CdTe/CdZnTe Pixellated Radiation Detector

Rasif Mohd Zain

University of Glasgow

School of Physics and Astronomy

Submitted in fulfilment of the requirements

for the degree of Doctor of Philosophy

November 2014

In memory of Mohd Zain Othman, Md Said Hassan & Rahmah Hj. Lassim...

Abstract

The work in this thesis is focused on the study of CdTe/CdZnTe pixellated detectors. During this research, three main aspects have been covered in the development and application of these detectors. These broadly describe the fabrication process, characterisation of energy spectrum and imaging performance, and application of these detectors in industrial X-ray tomography.

The first topic to be discussed in detail is the fabrication process of CZT pixellated detectors. This is a process that involves many steps, such as cutting the sample, cleaning the substrate, writing a masking pattern with e-beam lithography, photolithography, cleaning the surface using oxygen ash, metallisation and removing the resin in the development stage. However, these stages were grouped into three major steps to give a clearer image on what was going on throughout the fabrication process. They are grouped as sample preparation, pixellated structure deposition and sample passivation. The dry ash processing had been carried out in the James Watt Nano Fabrication Centre at Glasgow University. The motivation for the development of the dry ash process was to reduce the level of leakage current on the surface of the device so that a good energy spectrum resolution could be obtained. The research showed that a passivation technique using a layer of SiN as well as an oxygen plasma oxidation layer provided low leakage current in the pixel and lower interpixel leakage current. A good performance in energy spectrum was achieved after performing passivation. The FWHM of Co-57 is 10.78 keV where energy resolution is 8.8%.

The second area covered in this thesis is the energy spectrum and imaging performance of pixellated CdTe Timepix detector. Two pitches of pixel have been studied namely, 110 μm

pitch and 55 µm pitch. The work on characterisations has been performed with polychromatic and monoenergetic beams of X-rays. In both the Counting mode and ToT (Time over Threshold) mode it was discovered that there were large effects on performance due to charge sharing and fluorescence. In terms of image quality the result of MTF was found to be as expected, around half the contrast transfer (30%) recorded for 110 µm compared to 55 µm pixel detector at 4 *lp/mm*. Another field of interest explored was the defect factor. For this to be achieved studies had been performed in positive and negative bias of CdTe Timepix detector. The results showed that the presence of defects in the material affects the performance of the energy resolution of CdTe Timepix detector.

The third area covered in this thesis was the study of CdTe Timepix detector for use in Industrial X-ray tomography. To give the sensor the best performance it could offer in capturing images for industrial use, work had been carried to optimise the technique for producing good quality images. The hardware setup involved the careful alignment all of the components of the system and the introduction of a collimator. In addition the sofware software it dealt with the flat field correction, noise filter and data projection algorithm. The results show that the CdTe Timepix detector can be used as a good detector for X-ray tomography. Here, the 3D of volume rendering studies had been performed to a pencil as a sample and voltage regulator. The result of the pencil image in volume rendering showed that CdTe Timepix detector had successfully provided good image for different density profile of material (paint coating, wooden and carbon). Not only that, another important finding besides the excellent image produced was that the effect of beam hardening, ring artifact and metal shrank artifact in tomogram of voltage regulator had been eliminated successfully.

Acknowledgements

I would like to thank my supervisor, Professor Val O'Shea, for all his help, efforts, patience and motivate this PhD would hardly be possible. I really appreciate his expertise and guidance over the last few years that enabled me to accomplish this thesis on time. Thanks also to my secondary supervisor, Dr. Richard Bates for his support and very helpful discussion of physics stuff.

Very special acknowledgement goes to Dr. Dzmitry Maneuski, who I very closely worked with throughout my PhD time. I deeply appreciate the patience and the time he's spent with me to complete my PhD thesis. His quality advice, patience, understanding of the topic, endless help and countless discussion helped me to complete and clarify the thesis manuscript.

During my PhD I involved in collaboration with Diamond Light Source and Mid Sweden University in characteristic of Timepix detector. I am grateful to thanks to all the member of collaboration for extremely well organized working environment, productive and enjoyable. I also had the opportunity to work under collaboration with Kromek. Thanks to all Kromek staff to support led to valuable results.

I would like to thank to Minister of Science, Technology & Innovation, Government of Malaysia to sponsor my PhD study. Thanks also to my top management of the Malaysian Nuclear Agency to believe and give me the opportunity to further my PhD study here.

Many thanks to my family for their love, moral support and pray especially to my wife, Nor Zairina Md Said and my kids Aliyah, Aleesya and Abdullah Faheem. Finally, thanks to all my relative and friends.

Declaration

I declare that expect where explicit reference is made to the work of others, this dissertation is the result of my own work. This work has not been submitted for any other degree at the University of Glasgow or any other institution.

Rasif Mohd Zain

Contents

List of Figure

List of Tables

Chapter 1

Introduction

1.0 Introduction

In the modern world radiation and its detection provide important tools which find use in many commercial sectors, industrial and medical fields. Radiation sources and measurement systems find routine use in achieving a quality control in the production line, diagnosing diseases as well as treating the deadliest of diseases such as cancer, generating electricity, studying the origins of the universe, treating our food for health, and also in less attractive applications like developing weapons of mass destruction. Thanks to most of these developments the application and development of radiation technology has been increased and new applications are constantly being developed. This increase in radiation detection technology development is of great importance to society and the economy. Radiation detectors help in the diagnosis of disease inside the body through medical radiation imaging, the monitoring of nuclear power plant to ensure no radiation leakage to the environment, and is used in airport cargo scanning to ensure the safety of the passengers where aeroplanes are free from weapons and bombshells.

Gamma-ray spectroscopy is a major area of interest in radiation detection where the process of identifying a radioactive isotope is based on the characteristic energies of its

emitted gamma rays. The probability of a gamma ray depositing all of its energy in a detector element is determined by the material used in the manufacture of the detector and so they need to be of a high atomic number and density. Furthermore, the device must be able to accurately reconstruct the amount of energy deposited, a parameter known as the energy resolution. To achieve a precise radiation detection measurement, semiconductors material are used for their excellent resolution in detecting radiation. This is because solid state semiconductor detectors absorb ionizing radiation, such as X-rays, gamma-rays, and alpha particles, from radioactive materials. The radiation waves or particles deposit their energy in the material when the interact with it and generate electron-hole pairs, which are separated using a voltage bias applied to the semiconductor and collected by the front-end readout electronics. Semiconductor materials offer the best gamma performance for spectroscopy following the development of germanium detectors. However, germanium must be cooled well below room temperature to minimize the thermal excitation of electrons from the valence band to the conduction band. Scintillation detectors have long been the room temperature spectrometer detector of choice: the energy resolution is more than an order of magnitude worse than germanium but scintillators have proven to be affordable and deployable for field work.

The performance gap between scintillators and germanium has led researchers to research the development of new materials needed for alternative room temperature semiconductors. Theoretically, such a detector should have a higher atomic number and density than germanium while achieving similar energy resolution, along with room temperature operation and approach the low cost associated with scintillators. Much research has been carried to find for a more appropriate material to meet these requirements, focusing on wide-band gap compound semiconductors. To date the research community has explored materials such as HgI_2 (1), *GaAs* (3), *CdTe* (2), and later *CZT*(4).

In this study, three main areas have been pursued in developing CdTe /CZT pixellated detectors. These concentrate on the fabrication process, characterisation of energy spectral and imaging performance and the application of detector in industrial X-ray tomography. The motivation of this work comes from noting that the properties of the

CdTe/CZT render it suited to room temperature operation which is a crucial parameter for many applications.

A high value of leakage current is one of the main impediments to the development of CZT pixellated detectors [5]. There is a need to minimise leakage current as it affects the energy resolution and detection efficiency of the detectors – this can be achieved through optimising the fabrication process. For this process the main objective is to develop a procedure that uses the best etching process in order to minimise the damage to the material that leads to the leakage current of a pixellated detector. To this end a technique using the wet etching method is the currently preferred way of achieving this. In this work, a dry etching technique has been applied using reactive ion electron (RIE) plasma to grow a SiN layer passivation layer. All of the processes involved in fabricating pixelated CZT detectors will be discussed in greater detail in Chapter 3.

The second issue discussed in this work concerns the characterisation of CdTe Timepix detectors. The studies of energy spectral performance, the effect of fluorescence and charge sharing present in pixelated detectors are discussed in Chapter 4. The findings resulting from this work can help users implement correction techniques that can improve energy spectral analysis. This study also looked at the module transfer function (MTF) of detector in imaging performance. The characterisations have been carried out using x-ray sources, x-ray generators and a synchrotron.

In looking at the application of these detectors for imaging it has been decided to use a Timepix readout to measure the detector performance as it can provide both photon counting and spectral information and therefore is a very powerful readout system for the analysis of detector performance for the tomography application. Studies have been carried out to present CdTe Timepix detector is well suited for use in industrial X-ray tomography. This study has also developed techniques which can produce high quality images and minimise the generation of artefacts in the reconstructed tomogram. The work also shows that the CdTe Timepix detector is capable of differentiating the density profile of materials

when used in the volume rendering of tomographic images. All the processes involved in the development of a low cost X-ray tomography will be discussed in Chapter 5.

1.1 Dissertation overview

This thesis is divided into six chapters. Chapter 1 provides a general background and overview of the dissertation.

Chapter 2 discusses the theoretical explanations involved in this work. It describes the fundamental principles of radiation interaction with matter, basic semiconductor properties and discuses the relevant properties of *CdTe/CZT* that make it suitable as an appropriate material for radiation detection. The latter part of the chapter briefly details how the synchrotron radiation at Diamond Light Source (DLS) was used to do the characterisation of *CdTe* Timepix detector.

Chapter 3 explains the processes involved in pixelated CZT detector fabrication work. In order to give a clearer idea and also to avoid confusion regarding the process patterns and steps, they have been grouped in three separate stages. The initial stage of sample preparation (starting from sample cutting to wet and dry etching cleaning) is followed by pixelated structure definition (which deals with e-beam lithography, photolithography, oxygen ash and metal deposition) and finally the dry etching passivation process (oxygen plasma oxidation layer and *SiN* layer). This is followed by a description of the experimental setup of I-V measurement (bulk and interpixel leakage current) and the discussion of the results in terms of bulk leakage current, interpixel leakage current, resistivity and energy spectral performance.

Chapter 4 is devoted to a detailed characterisation of the hybrid single photon counting CdTe Timepix detector. The results discussed in this chapter assess both imaging and spectroscopic performance capabilities of two detectors, one with 55 μm pixels and the other with 110 μm pixel pitch. In addition, studies are carried out to measure the effect of

CdTe properties in terms of its leakage current when different bias voltage is applied and also the sensor's charge carrier transport properties. The studies continued with the energy spectral analysis in ToT mode as well as the performance of energy resolution of the detector as a function of different bias voltage. Energy resolution has also been studied using using an x-ray machine (Ag, Cu, Fe, Mo and Ce). Lastly, studies were carried out using the extreme condition monochromatic beam line synchrotron radiation at the DLS where the energy spectral performance can be analysed using the ToT mode available in the Timepix. Studies are also carried out to show the impact that charge sharing and fluorescence have on energy resolution. Meanwhile, a different approach has also been used to determine the energy spectral performance using the threshold scan (DAC Scan) mode in the CdTe Timepix detector in counting mode. Through this approach, the effects of different parameters (bias voltage, gain, count rate) had on the sensor can be measured. The MTF study focused on the imaging performance of the detectors with different bias voltages applied. Finally, in this chapter the presence of material defects has been explored.

Chapter 5 looks at the application of CdTe Timepix detector for X-ray tomography. It describes the study of different algorithms in beam projection, which gives a good contribution to produce high quality images and also to eliminate the artefacts which commonly occur in tomographic images. In addition the performance of the technique of volume rendering of of the image are discussed.

Finally, Chapter 6 is an overview of the thesis results. General conclusions about the research are presented in this work and suggestions for future work are provided.

Chapter 2

Basic Concepts of Semiconductor Detectors

2.0 Introduction

To fully understand the importance of studying the CdTe and CZT radiation detectors, a literature review of the principles of radiation detection, semiconductor properties, and the use of the x-ray synchrotron is presented in this chapter.

This chapter is divided into four sections. Section 2.1 starts with a literature overview of the theoretical background of the interaction of radiation with matter which illustrates the radiation detection principles behind the operation of *CdTe/CZT* as a nuclear radiation detector. This section describes the types of radiation interaction relevant to the work involved in this thesis. In Section 2.2 the theoretical background of semiconductor properties and operation are described [1]. Section 2.3 discusses the material properties that make *CdTe/CZT* crystal such a highly desirable material for use as gamma ray detectors. Finally, Section 2.4 describes the x-ray synchrotron and how it is used to define

the characteristics of CdTe Timepix detector. Further information on these topics can be found in references [6]-[8].

2.1 Radiation Interaction

Radiation refers to energy in the form of waves or particles. Radiation can consist of either charged or uncharged particles and photons. Charged radiation, such as beta particles, positrons, protons, alpha particles and fission fragments, are also known as ionizing radiation because they transfer energy to orbital electrons during interaction with matter. Neutrons are charge neutral and interact with matter differently and are not a topic covered in this work. Another uncharged radiation can exist as an electromagnetic wave, such as x-rays, gamma rays. Radiation types like these can be produced through many processes such as:

- Relaxation of an excited atom to its ground state either by ionization or by emission of an orbital electron.

- Spontaneous decay of heavy nucleus to produce alpha particles or fission fragments, or neutrons.

- Relaxation of an excited nucleus to a lower energy state to emit gamma rays.

In addition, gamma rays can also be emitted from the annihilation of electrons with positrons. Gamma rays are the most energetic form of electromagnetic radiation. Alpha particles typically have energy from ~3 to 7 MeV. Slow neutrons have energies ~0.025 eV while fast neutrons have 10 keV to 15 MeV.

For radiation to be detected, it must first undergo some interaction with the medium of detection. The interaction mechanisms of gamma and x-rays are known as the Photoelectric effect, Compton scattering and Pair production. Fig. 2.0 show the cross section of interaction of radiation through the material.

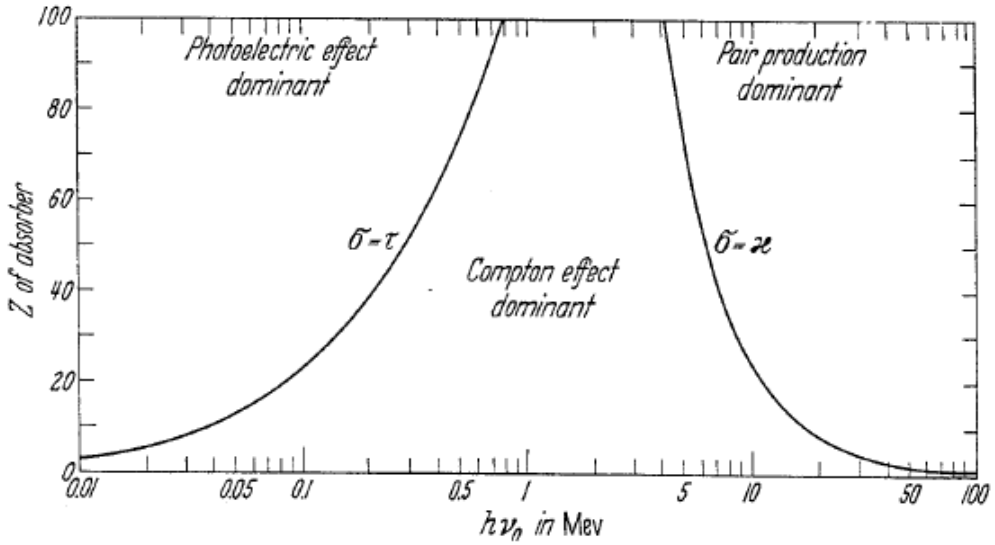

Figure 2.1: Regions of the relative dominance of the photoelectric effect, Compton scattering and pair production depending on the photon energy and the atomic number Z of the target material.

Photoelectric effect

Photoelectric absorption happens when all of the energy of an incident photon is absorbed by one of the orbital electrons of the atoms in the detector material which produce a photoelectron. This photoelectron has a kinetic energy equal to incident photon energy minus the atomic binding energy of the electron. The most probable origin of ejected photoelectron is the most tightly bound *K* shell of the atom. The photoelectron then loses its kinetic energy by Coulomb interactions with the semiconductor lattice thereby creating many electron-hole pairs. The number of electron-hole pairs created is a simple function of the energy of the incident photon.

$$E_{e^-} = hv - E_b \tag{2.1}$$

where E_{e^-} is the energy of photoelectron, hv is the incident photon energy and E_b is the binding energy of the electron in the original shell. Fig 2.1 shows the process that describes the photoelectric effect of photon interaction with matter.

Some of the x-ray photons may be generated and reabsorbed through the same photoelectric effect by less tightly-bound electrons. Photoelectric absorption is the predominant mode of interaction for gamma and x-rays. The photoelectric process is enhanced for materials with high atomic number Z. The probability, τ, of photoelectric absorption per atom over all ranges of energy $(E\gamma)$ and atomic number (Z) is roughly approximated as

$$\tau = const * \frac{Z^n}{E_\gamma^{3.5}} \tag{2.2}$$

where the exponent *n* varies between 4 and 5 over the energy region of interest. Equation 2.2 shows the dependence of the probability of photoelectric absorption on the atomic number of the absorbing material.

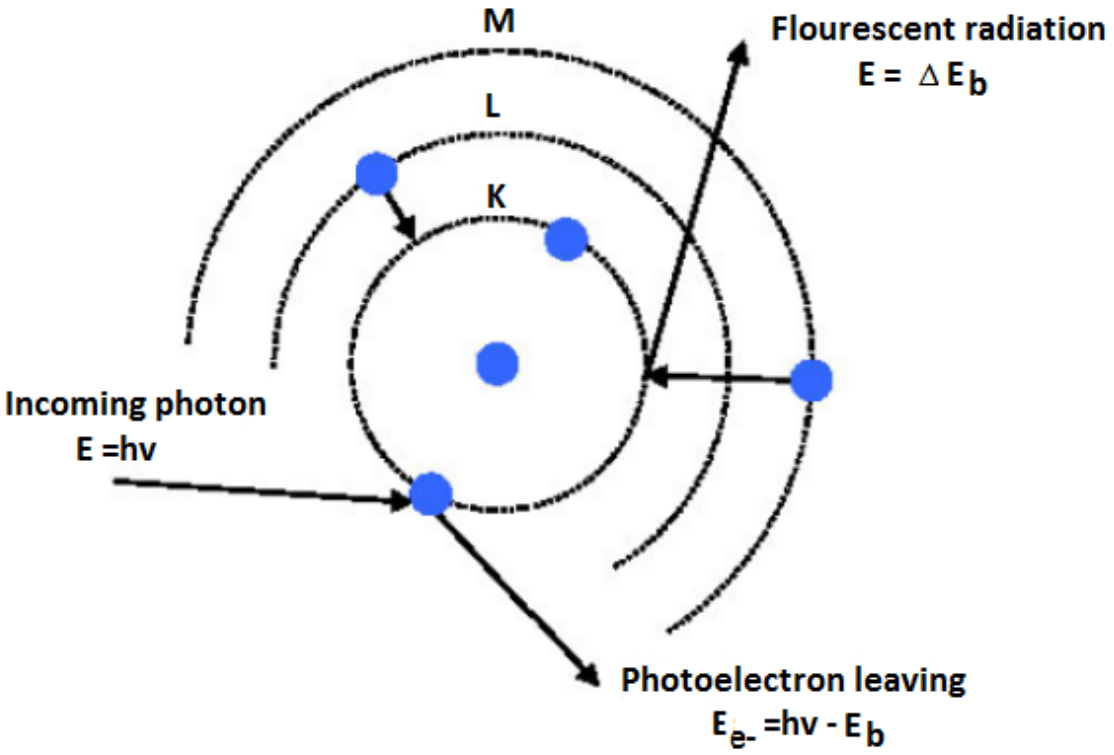

Figure 2.1: *Schematic of photoelectric absorption*

Compton scattering

Compton scattering is the predominant interaction mechanism for electromagnetic photons with energies over 100 keV. When an incoming photon collides with an orbital electron, the direction and energy of the incident photon is altered. The incident photon transfers some of its energy to the orbital electron. This electron loses its energy through creation of electron-hole pairs. Energy transfers are determined from the conservation of energy and momentum during the interaction.

The kinematics of the energy transfer is shown in Fig. 2.2 and described by the following equations

$$hv' = \frac{hv}{1+\frac{hv}{m_o c^2}(1-cos\theta)} \tag{2.3}$$

Where $m_o c^2$ is the rest-mass energy of the electron (0.511 MeV), hv and hv' is the energy of incident and recoil photon respectively. The incoming photon is deflected by an angle θ with respect to its original direction. A fraction of the photon energy is transferred to the electron. Since all scattering angles are possible with varying probabilities, this energy can vary from zero to a large fraction of the photon energy [3].

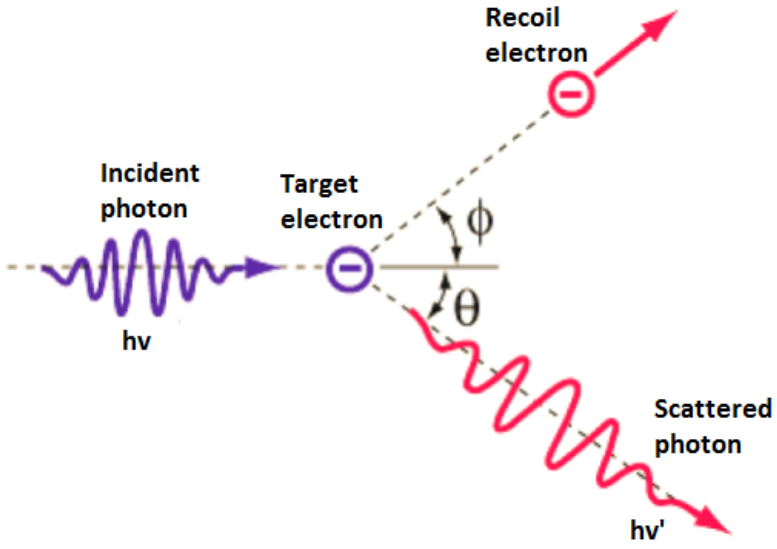

Figure 2.2: *Schematic of the mechanism of Compton scattering*

Pair production

An incident photon with energy above 1.022 MeV may create an electron-positron pair. Any excess energy can go into kinetic energy of the electron and positron. As the positron has a very short lifetime in the material it will annihilate with an electron in the material to produce two *annihilation photons* of energy 0.511 MeV. The annihilation photons then interact with atoms of the material to create electron-hole pairs. These two photons then lose energy by Compton scattering or the Photoelectric effect. Fig 2.3 shows the schematic process of pair production.

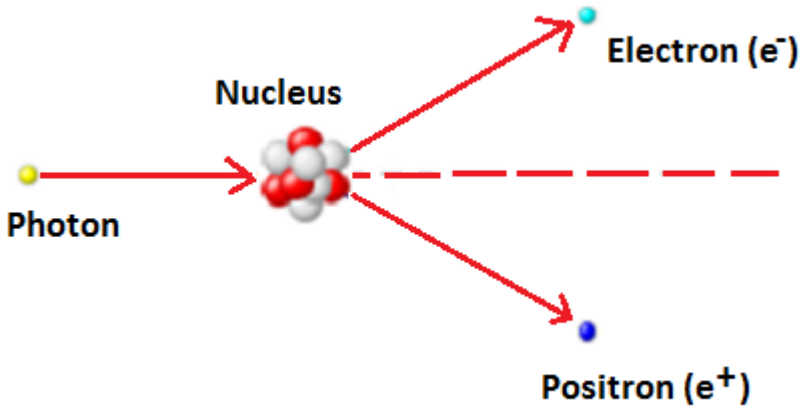

Figure 2.3: *Schematic of pair production process*

2.2 Semiconductors properties

Semiconductor materials are used in the fabrication of solid-state detectors. The materials are considered semiconductors due to their electrical conduction properties – being neither good conductors nor insulators. Here, the presence of a small energy gap between their valence and conduction bands helps the devices to function as detectors. This is because a small energy deposition can move electrons from the valence band to the conduction band, leaving holes behind. The two charge carriers (electron and hole) drift and produce a signal when an electrical field is applied. By collecting the charge carriers liberated by energy

deposition in the semiconductor the passage of an ionizing particle can be detected. The best semiconductor detectors for high energy photons are where the detector materials that have high detection efficiency, good energy resolution and good room temperature performance. Table 2.0 shows the summary of the requirements of the semiconductor material for good radiation detector performance in these applications..

TABLE 2.0: *Summary of Demand and Performance*

Demands	**Performance**
1. Large band gap	• Leakage current becomes sufficiently low, making room-temperature operation possible.
2. High atomic number	• Short absorption length for γ, also for relatively high γ-energy, γ-radiation can be detected with high efficiency
3. Long drift-length ($\mu F\tau$, *is preferably* ≥ the depletion width ω, for both electrons and hole μ=mobility, F=field, τ = carrier lifetime)	• Effective charge collection, the signal becomes independent of where in the detector the radiation is absorbed, ensuring good energy resolution.

Band structure

A semiconductor detector is fabricated from either elemental or compound single crystal materials with low band gap energy (approximately 1 to 5 eV). Fig. 2.4 shows the energy band diagrams of three classes of insulators, semiconductors, and conductors.

A solid contains many atoms with orbiting electrons. Under the right conditions the electrons on the outermost shell of an atom (valence band) are free to move to the conduction band. The energy difference between these two bands is known as the energy gap (E_g). It is known that metallic objects conduct electricity whereas non-metals (insulators) are not good conductors. In metals E_g is almost zero since the energy bands are so close together, so under a small electric field electrons can easily move from the valence band to the conduction band. Insulators have a larger E_g (greater than 5eV) so that it is difficult for electrons find the energy necessary to jump the gap. Conduction in insulators is so small compared to metals that it can be considered to be negligible. Semiconductors are materials whose electrical conductivity falls in between metals and insulators. E_g is small (~1eV). The level of conductivity can vary depending on temperature, optical excitation, and the purity of the semiconductor material [9, 10].

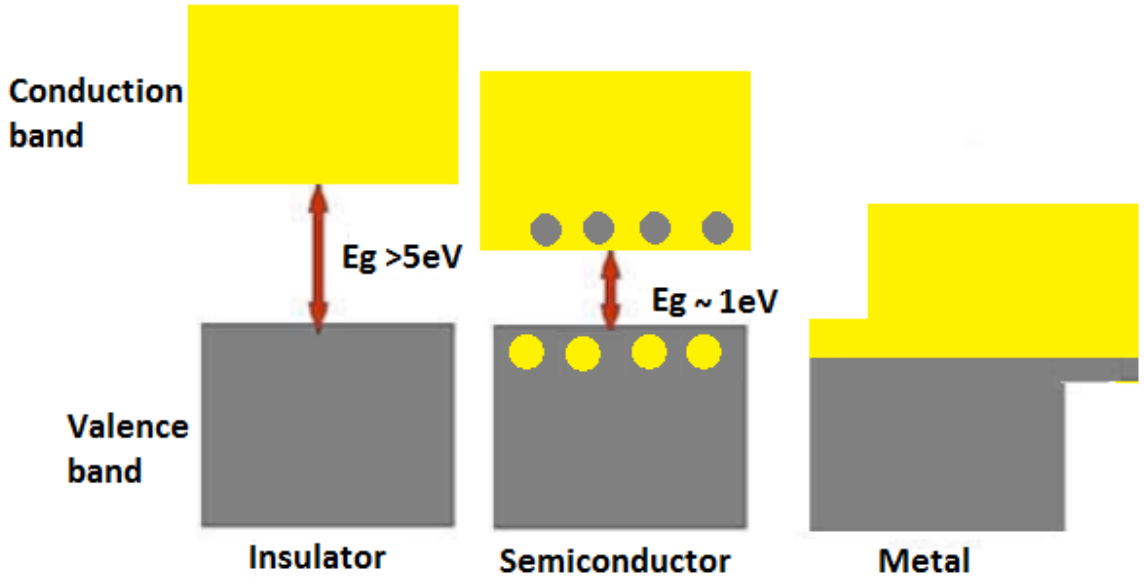

Figure 2.4: *Band structure for electron energies in materials.*

As the electron is promoted to the conduction band it leaves a vacancy, a hole in the valance band and so an electron-hole pair is created. A charge is induced on the electrodes of the detector element as the electron-hole pair drifts through the conducting medium.

Charge carriers

The fundamental property of charge transport in a semiconductor is the mobility (μ). As an electric field (ε) is applied across the semiconductor medium electrons and holes will migrate, where the motion is a combination of random thermal velocity and the net drift velocity (v_d) parallel to the direction of the applied field [7]. The mobility is related to the drift velocity and the applied field by;

$$(V_d)_{e,h} = \mu_{e,h}\, \varepsilon \tag{2.4}$$

where the subscript notation refers to the electron and hole component. Mobility is therefore also related with the drift time (τ) of the electrons and/or holes, drifting between the contact electrodes at a distance *d* apart (typically the thickness of the detector material).

$$\mu_{e,h} = \frac{d}{\tau_d} . \frac{1}{\varepsilon} \tag{2.5}$$

For an efficient detector with fast signals and large pulse amplitudes, the mobility should be high with a short drift time.

$$\tau_d = \frac{d^2}{\mu_{e,h} V} \tag{2.6}$$

where *V* is the applied voltage. Equation (2.4) can be rewritten in the form,

$$\lambda_{e,h} = \mu_{e,h} \tau_{e,h} \varepsilon \tag{2.7}$$

where λ is the mean carrier drift length and $\mu\tau$ is the (electron/hole) mobility-lifetime product. $\mu\tau$ itself is an important quantity that reflects the quality of the detector material. The Charge Collection Efficiency (CCE) is the ratio of the integrated collected charge with respect to the total electron/hole charge generated from a radioactive source at a given bias [11].

$$CCE = \frac{Q}{Q_O} \tag{2.8}$$

The CCE is also related to $\mu\tau$ using a simplified form of the Hecht equation,

$$CCE = \frac{(\mu\tau)V}{d^2}\left[1 - exp\left[\frac{d^2}{(\mu\tau)V}\right]\right] \tag{2.9}$$

In this thesis the charge carrier mobility work for the pixelated CdTe Timpix detector has been evaluated and discussed detail in Chapter 4.

Resistivity

The material properties required for a good room temperature nuclear detector include high resistivity and long lifetime of charge carriers. In this study the effect of resistivity of CZT pixelated design after the use of a novel passivation process is discussed in Chapter 3.

In theory, zinc telluride has a higher band gap than CdTe so that alloying CdTe with Zn increases the band gap and intrinsic resistivity of CZT from 10^{10} Ωcm to over 10^{16} Ωcm. Research [12] shows an increase of about two orders of magnitude in the resistivity of CZT as the fraction of zinc is increased - shown in Table 2.1. This increase in resistivity results in a decrease of the leakage current in the material.

In order to calculate the resistivity of semiconductor material in the pixellated design of an ohmic detector, where current (I) is flowing through a medium of pixel detector with an applied voltage (V). There is an “opposing force” which impedes the current flow know as resistance (R). Ohms law states;

$$V = IR \tag{2.10}$$

The resistance is the ratio of the potential voltage to the current. It has the unit of ohms (Ω). The resistivity (ρ) relates the resistance to the volume of the medium (cross-section area A with length L) and is given by the expression;

$$\rho = \frac{RA}{L} \tag{2.11}$$

***Table 2.1**: Resistivities of $Cd_{1-x}Zn_xTe$ crystals as a function of x.*
Crystals were grown by the high pressure Bridgman technique. (Extracted from [12])

Composition	Resistivity (Ω-cm)
CdTe	3.0×10^{9}
$\boldsymbol{Cd_{.96}Zn_{.04}Te}$	2.5×10^{10}
$\boldsymbol{Cd_{.9}Zn_{.1}Te}$	2.5×10^{11}

Spectroscopy

Radiation spectroscopy is an analytical technique which can determine the energy emitted from a given source/radionuclide. By connecting the right detector to a data acquisition tool known as a multi-channels analyser (MCA) the energy of the radiation can be seen physically as an image called a spectrum. An energy spectrum is a statistical count of events, which are "binned" into channel in an MCA. If the characteristic peak energy is known then the channel number can be calibrated in terms of energy. Strictly the random nature of radiation is described by the Poisson distribution, however, if good counting statistics are achieved then the randomness tends toward a Gaussian distribution.

The width, or the full width half maximum (FWHM), of the peak describes the energy resolution of the detector. The FWHM is related by,

$$R = \frac{FWHM}{x_o}$$

$$= \frac{\sqrt[2]{2ln2\sigma}}{x_o} \tag{2.12}$$

where R is resolution, x_o is the mean/centroid and σ is the standard deviation. Since the resolution is a ratio it is often quoted as a percentage, although is some cases the resolution can be quoted as the FWHM alone.

2.3 CdTe/CdZnTe properties

CdTe / CdZnTe Detector

CdTe has been studied as an X-ray and γ-ray detector since 1960s [13]. CdTe has a cubic zincblende crystal structure with atomic number of 50 (Cd = 48 and Te = 52 and a wide band gap of 1.44 eV, which favours room temperature operation. Poor charge carrier transport properties and disparity between electron and hole properties are typical of CdTe materials ($\mu_e\tau_e$ = 10^{-3}cm^2/V and $\mu_h\tau_h$ = 10^{-4} cm^2/V). The low values of the charge carrier mobility – lifetime product are due to the presence of defects and impurities in the crystals which act as trapping centres. In this thesis the charge carrier mobility work for the CdTe Timepix detector has been studied and discussed detail in Chapter 4. Typical defects in CdTe are mainly structural defects, impurities and complexes of the two, such as cadmium vacancies and donor impurities (*Cl*, *In*) [14]. The principal physical properties of CdTe are presented in Table 2.2. High purity CdTe crystals can be grown by using different techniques, such as zone melting, the Bridgman method, epitaxial and travelling heater method (THM). CdTe crystals are usually grown by the THM method and doped with *Cl*

to compensate background impurities and defects, resulting in high resistivity *p*-type materials (10^9 Ωcm) [14].

Table 2.2: *Physical properties of the principal compound semiconductor at T =25°C* [15]

Material	Si	CdTe	$Cd_{0.9}Zn_{0.1}Te$
Atomic number	14	48, 52	48, 30, 52
Density (g/cm^3)	2.33	6.20	5.78
Band gap (eV)	1.12	1.44	1.57
Pair creation energy (eV)	3.62	4.43	4.6
Resistivity (Ω cm)	10^4	10^9	10^{10}
$\mu_e\tau_e$ (cm^2/V)	>1	10^{-3}	10^{-3} -10^{-2}
$\mu_h\tau_h$ (cm^2/V)	~1	10^{-4}	10^{-5}

$Cd_{1-x}Zn_xTe$ is also a suitable material for room temperature radiation detectors [5, 15]. The addition of zinc at the level of a few percent increases band gap as well as the energy of defect formation. CdTe and ZnTe form a solid solution throughout the entire alloy range, however only the range x = 0.1 to 0.2 is applied for detector applications (x is the blending fraction of ZnTe in CdTe). The increased band gap (1.57 eV for x = 0.1) ensures high bulk resistivities and reduces the dislocation density, resulting in lower leakage currents and higher temperature operation. Specifically, resistivities of CZT are typically between one and two orders of magnitude greater than that of CdTe and the resultant leakage currents are correspondingly lower. This is important for the detector performance, as it permits measurements to be taken with a lower leakage current or a larger applied bias. This ternary compound has a cubic, zincblende type lattice with atomic number close to that of CdTe. The main drawback of CZT crystals is the low value of $\mu\tau$ values of electrons and holes compared to CdTe (Table 2.2). However, the main advantage of CZT over CdTe detectors is the absence of the polarization effect, which limits the exploitation of CdTe detectors.

CZT detectors are usually fabricated with ohmic contacts (*Pt, Au*). CZT detectors with ohmic contacts (*Pt*) showed good energy resolution of 1.4% (FWHM) at 59.5 keV (T= -37^{o}C) [16]. Nevertheless, the poor hole charge transport properties produce long tails in the measured energy spectra. In order to overcome this constraint, single carrier device has been developed [17].

The poor hole transport properties of CdTe and CZT materials are a critical issue in the development of X-ray and gamma ray detectors. Hole trapping reduces the charge collection efficiency of the detectors and produces an asymmetric long tailing of the photopeaks of the measured spectra (hole tailing). Several techniques have been used to minimize this effect. The planar parallel field (PPF) is the classical configuration used in overall planar detectors, in which the detectors are irradiated through the cathode, thus minimizing the hole trapping probability if the detector is thin. In an alternative configuration, denoted as planar transverse field (PTF) [18], the irradiation direction is orthogonal (transverse) to the electric field. In such a configuration different detector thicknesses can be chosen, in order to achieve the detection efficiency required, without modifying the inter-electrode distance and therefore the charge collection properties of the detectors. This technique is particularly useful for detectors with needing high detection efficiency in the gamma energy range. Several techniques are used in the development of detectors based on the collection of electrons (single charge carrier sensing detectors or unipolar detectors), which have better transport properties than those collecting both carrier or holes. Single charge carrier sensing techniques are widely employed for CdTe and CdZnTe detectors, by using both electronic methods pulse rise time discrimination [19], bi-parametric analysis [20, 21] and by developing careful electrode design Frisch-grid [22, 23], pixels [24, 25, 26], coplanar grids [27], strips [28, 29] multiple electrodes [30]-[33].

For imaging performance, application the CdTe pixilated detector gain a good quality image [34]. Chapter 5 describes imaging performance of the pixilated CdTe Timepix detector used in x-ray computed tomography mode.

2.4 X-ray Synchrotrons

X-ray synchrotron facility at Diamod Light Source has been used in this work to measure the characteristics of the CdTe Timepix Detectors. A synchrotron is a bright source of mono-energetic x-rays, invented in 1943 [35]. A synchrotron accelerates a beam of electrons and feeds these beams to wiggler cavities that use strong magnetic fields to induce the electrons to radiate x-ray photons. They are used to generate intense beams of light across a broad range of energies (1 to 150 keV) for use in a wide variety of experiments.

Particle accelerators use electric fields to increase the energy of the particle. This can be done by using a series of hollow radio-frequency (RF) cavities, each of which has an alternating voltage applied to it. The alternating voltage is timed so that when the bunches of particles pass through the cavity, the electric field will accelerate them and increase their energy. In a linear accelerator, the RF cavities simply form a line. In a synchrotron, the RF cavities form a circle, and a series of bending magnets are used to steer the particle beam. So, the particles repeatedly travel round the ring, gaining energy with each revolution. The synchrotron complex has a number of feeds off the primary beam that produce the beams of photons which are then sent to the experimental hutches where measurements are carried out. Fig. 2.5 shows the layout of the synchrotron at the Diamond Light Source.

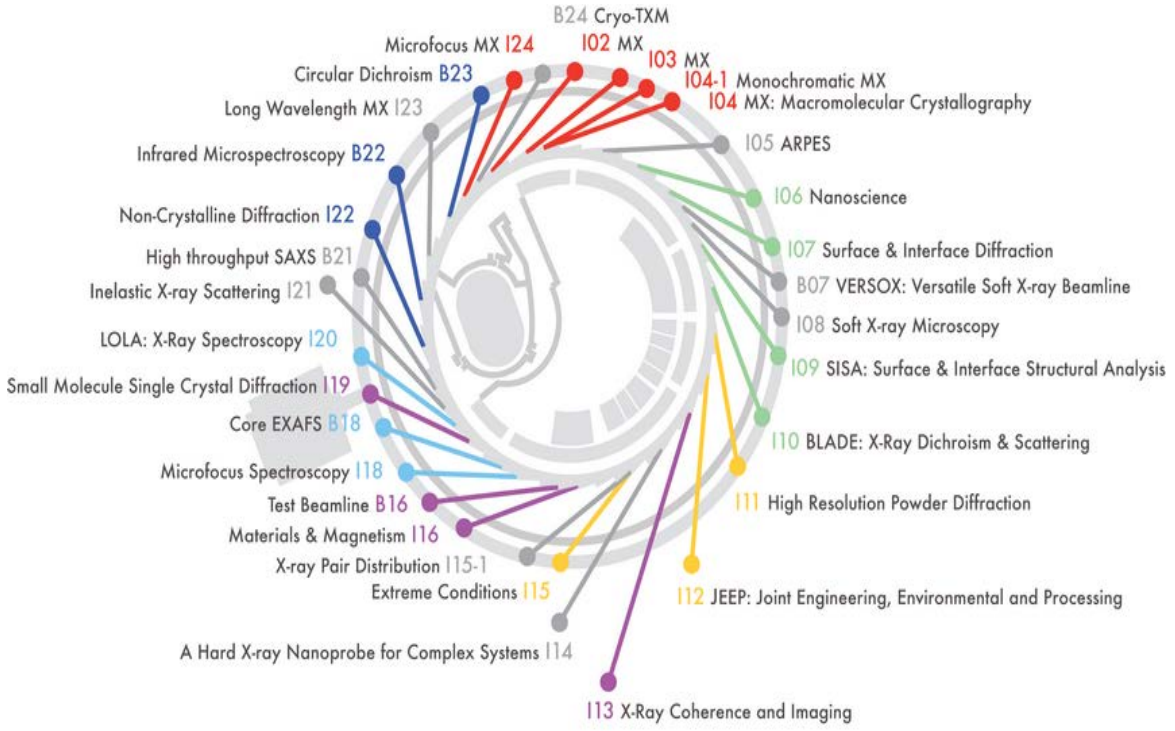

Figure 2.5: *Schematic of the Diamond synchrotron [36].*

To prevent the bunches of particles in the synchrotron from dispersing, it is necessary to apply magnetic focusing, both in terms of spatial position and momentum. Along the direction of motion, the RF cavities can be configured to have a focusing effect. The phase of the sinusoidal voltage applied to the RF cavity is chosen so that particles lagging behind the bunch pass through the cavity when the electric field is stronger, boosting their energy and causing them to catch up with the main bunch. Conversely, particles leading the bunch are accelerated less. To provide focusing perpendicular to the particles' motion, additional magnets are used, as described in Ref. [37].

Chapter 3

Fabrication of *CdZnTe* Pixellated Detector

3.0 Introduction

In this chapter the process steps that need to be carried out for the fabrication of *CdZnTe (CZT)* samples with a pixellated structure are described. Most of the optimization of these process steps has been carried out based on previous work [38]. Firstly, an overview of the process flow is given, followed by a more detailed description of each process step used. These processes are dependent on the process equipment and process specifications available at the James Watt NanoFabrication Centre (JWNC) which take into account the limitations of the equipment and the challenges in adapting these recipes to deliver the required performance for our *CZT* structures. A special additional process step, introduced to improve the recipe and create a novel low leakage current structure leading to an improved energy resolution for *CZT* pixellated structures, is also presented. This research is based on a collaboration with Kromek who were the suppliers of the *CZT* crystals for this work.

3.1 Overview of the process flow

Fig. 3.1 illustrates the main steps of the process used in the fabrication of the *CZT* pixel detector structures. The motivation for choosing each process step in Fig. 3.1 is based on the need to fabricate low leakage current pixel structures with high yield and repeatability. The process sequence described is the standard way of substrate cleaning, pattern definition and metallisation used for semiconductor fabrication in our clean room facilities. Additional process steps to minimise leakage currents are a novel part of this work.

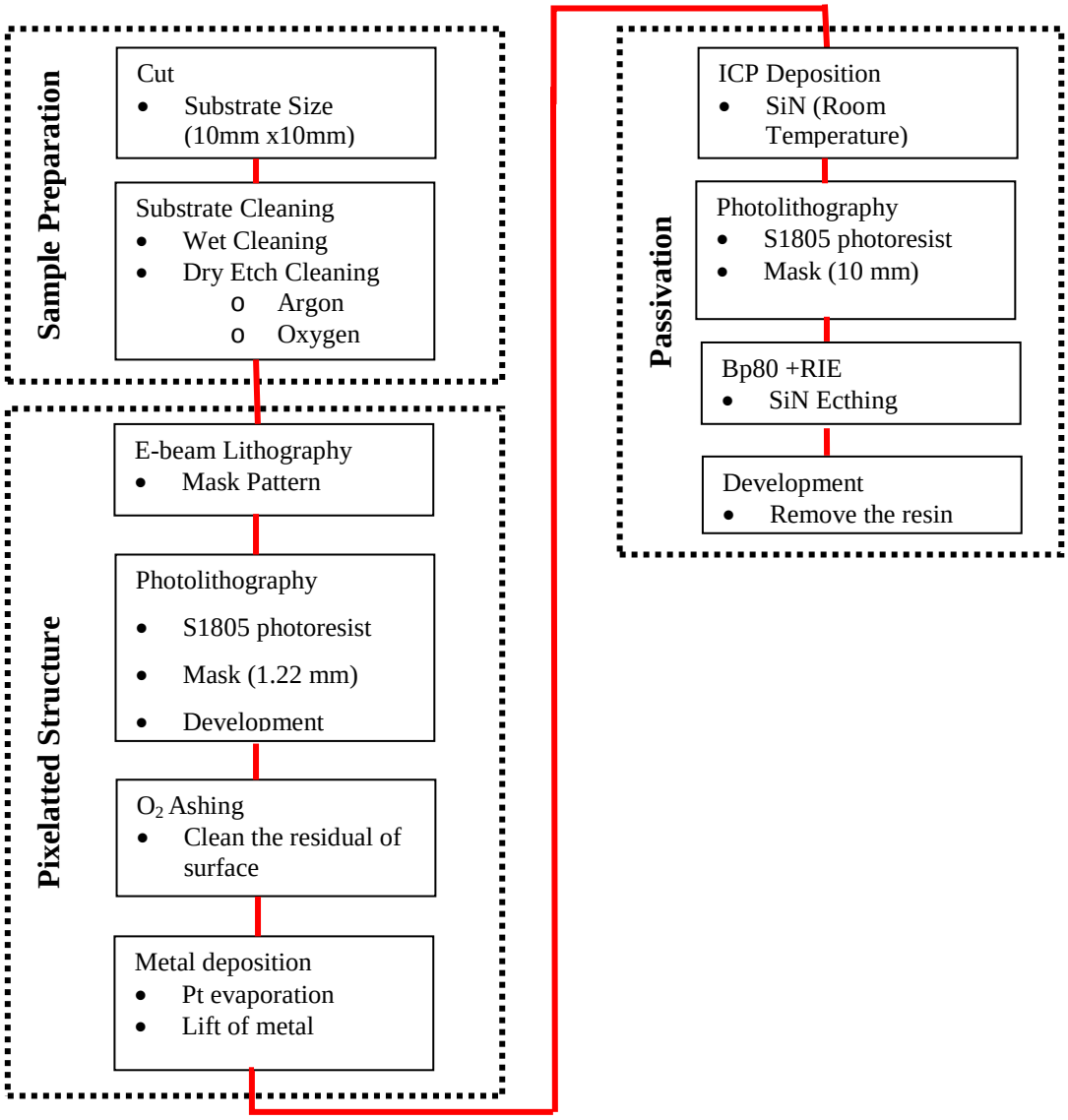

Figure 3.1: *General process flow of the fabrication steps of CZT pixellated detector*

As illustrated in Fig.3.1 the principal fabrication process can be divided into three main stages. The first stage concerns the preparation of the substrate which is common to almost every fabrication process. The second stage is the formation of a pixellated structure using photolithography and metal deposition which are also well defined processes available from the JWNC. The third stage in the fabrication process describes the deposition of a passivation layer of *SiN* using an inductively coupled plasma (ICP) deposition technique.

3.2 Sample preparation

The material for this study is *CZT* produced by Kromek using a proprietary growth technique [39]. This material is produced using a novel technique based on Physical Vapour Transport that enables the growth of high quality material. In comparison to the traditional growth technique which produces 75 mm ingots that are rarely in single crystals, this technique has the advantage of growing *CZT* of arbitrary thickness on special substrates with a diameter up to 100 mm with almost single crystal quality. The original wafer (diameter: 4 inches) is cut into smaller fragments (10 x10 mm^2) to enable optimisation of the fabrication process.

Prior to any manipulation the substrate is flushed with acetone and blow dried with dry nitrogen gas. Acetone is the standard solvent used to remove organic contaminants from the semiconductor substrate surface. The substrate is then cleaned with deionised water in an ultrasonic bath for two minutes. The ultrasonic energy creates small bubbles which collapse at high speed due to the phenomenon of cavitation. This process physically removes contaminants from the substrate surface in the same fashion as a gentle mechanical scrub – the substrate is then dried by gently blowing a jet of dry nitrogen gas over the substrate. Finally the substrate is cleaned with methanol in an ultrasonic bath for 2 minutes. Nitrogen gas is then used to blow any remaining methanol off the substrate surface. This is a standard process in the JWNC known as wet cleaning.

In addition the substrate was cleaned using argon and oxygen ion etches using a BP80+ Reactive Ion Etching (RIE) Machine to ensure that the surface of the substrate had minimal chemical contamination. This process removes any non-stoichiometric surface layer generated by the mechanical polish preparation. The conditions used for this step are listed in Table 3.0.

Table 3.0: *BP80+ parameters used for surface treatment of CZT substrate*

Parameter	**Flow 1**	**Flow 2**
Process gas required	Argon	Oxygen
Table temperature (^{o}C)	22	22
GAS FLOW (sccm)	100	100
PROCESS PRESSURE (milliTorr)	20	15
RF POWER (W)	50	30
PROCESSING TIME (minutes)	5:00	10:00

A wet cleaning process is useful in substrate cleaning, however, a general tendency is to minimise wet processes and use dry processes only as they are more reliable and repeatable.

3.3 Pixellated Structure

In order to realise the pixellated structure which needs to be deposited on the anode surface of the *CZT* substrate and achieve an ohmic contact, the following fabrication processes need to be carried out.

3.3.1 Lithography

In the field of microelectronic fabrication the lithography process transfers a pattern that has been created using computer software to a substrate so that complex shapes can be

built up using many deposition and etch stages on multiple layers. The word Lithography is Greek in origin, and according to the Cambridge Advanced Learner's Dictionary, means: 'picture printed using a stone or metal block on which an image has been drawn with a thick oily substance that attracts ink' [40]. In this study the word lithography is used to define the process of transferring a pattern of geometrical shapes onto a substrate surface. The pattern is transferred to the substrate using a layer of photoresist which is a chemical compound formulated to be sensitive to light in such a way that the areas exposed either harden or soften (positive or negative resists) when developed. This is applied to the substrate surface and the pattern transferred via exposure to light through a mask (or electrons – steered by the beam writer), followed by the development process. Following development the areas of the substrate not covered by the photoresist can be metallized replicating the pattern defined by the resist template.

Many techniques for lithography have been developed using sources ranging from optical (UV) to non-optical (e-beam, protons, X-ray). Each of these techniques has specific advantages and limitations in particular applications. For example *resolution* is defined as the minimum feature dimension that can be transferred with high fidelity to a resist film on a semiconductor wafer. *Registration* provides a measure of how accurately patterns on successive masks can be aligned (or overlaid) with respect to previously defined patterns on the wafer. Finally *throughput* is the number of wafers that can be exposed per hour for a given mask level [6]. For this project optical lithography was considered the most efficient technique for the fabrication of CZT pixellated detector for the required dimensions and the minimum feature size needed to define the pixels.

3.3.2 Photolithography

Photolithography (or optical lithography) is a process which uses light to transfer a geometry pattern from mask to a light-sensitive film (photoresist, or simply resist) on the substrate. The resist is applied to the substrate by applying some drops of the resist through a microfilter while the substrate is placed on a spinner. The resist has been formulated to a precise viscosity so that a predetermined film thickness is deposited over most of the

substrate when it is spun at high velocity (3000 rpm) on the spinner. Having defined a layer of precise thickness the resist is then baked in an oven (Usually at 90 °C for 30 minutes) to drive off the solvents and prepare the substrate for the exposure.

There are two methods used to expose the resist to the optical source: shadow printing and projection printing [6]. In shadow printing, the mask and the substrate are contacted directly one on top of the other as in contact printing, or in close proximity known as proximity printing. Fig. 3.2 (a) shows the basic setup for contact printing where a resist-coated substrate is brought into physical contact with a mask, and the resist is exposed to a collimated beam of ultraviolent light through the back of the mask for a fixed time. The intimate contact between resists and mask provides very high resolution (~ 1 μm) [41], the disadvantage of this method however is due to the presence of dust particles. A dust particle on the substrate can be stick to the mask when it contacts the substrate. The embedded particles then cause permanent damage to the mask and result in defects on the substrate with each succeeding exposure. In order to minimize mask damage, the proximity exposure method is used. Fig. 3.2 (b) shows the basic setup of proximity printing. For this reason, proximity exposure is preferentially used in this work. The photolithography machine used to carry out this work is the SUSS MA6 which is optimised for the proximity exposure process.

Alternatively one can use projection printing which is an exposure technique that projects an image of the mask pattern onto a resist-coated substrate that can be many centimetres away from the mask. To increase resolution, only a small portion of the substrate is exposed at a time. The small image area is scanned or stepped over the substrate to cover the entire substrate surface. Fig. 3.2 (c) shows the basic setup of projection printing.

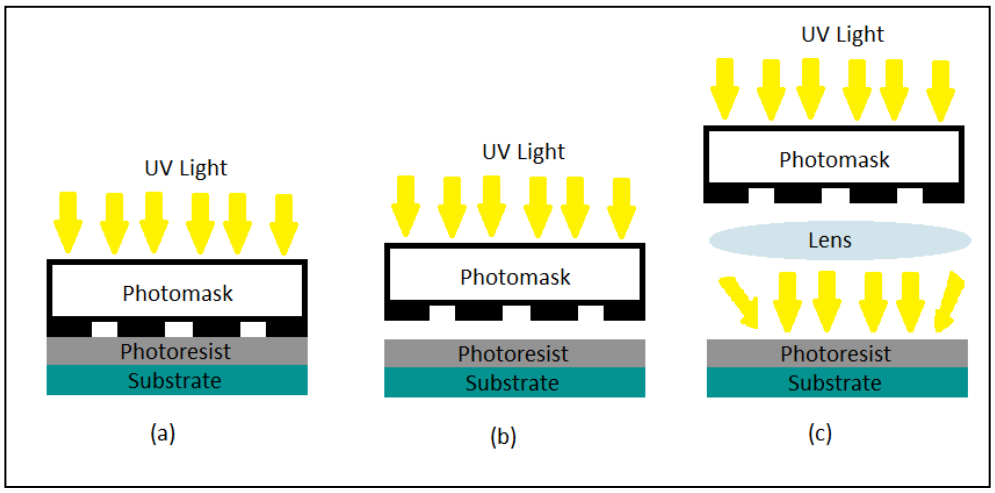

Figure 3.2: *Basic setup of exposure method. (a) Contact printing. (b) Proximity printing. (c) Projection printing.*

3.3.3 Mask

The masks used for photolithography are produced using an electron beam lithography tool (EBL). In order to make a mask of a required design, a design file is first created. This is done in a semiconductor layout design package called L-Edit v.15 by Tanner EDA. This is a user-friendly PC-based CAD design package. It has the capability of designing a device structure which can be divided into different cells in a hierarchical manner - making it easier to design a complex structure while retaining the ability to amend any small changes in the design without the need to make big changes in the design of the whole structure. The design pattern is subsequently streamed to a GDSII (Graphic Data System II) file. The GDSII is a binary file format representing planar geometry shapes, text labels, and some other information – which is arranged in hierarchical form. The objects are grouped by numeric attributes assigned to them, including the layer number or data type. The GDSII file is fractured in the CATS (Computer Aided Transcription System) environment to regenerate the file data for individual pixels before the file is transferred to the BELLE (Beam-writer Exposure Layout for Lithography Engineers) software system which is developed specifically to be used for EBL – and which is used to drive the electron beam to write the pattern on the mask. During this stage, various parameters will be determined by the user, such as base-dose, spot-size, and the location of the pattern, beam energy, and calculation of the total job running time. Fig. 3.3 shows the design layout for one of the mask plates used for this work – this is the plate for the metal layer deposition.

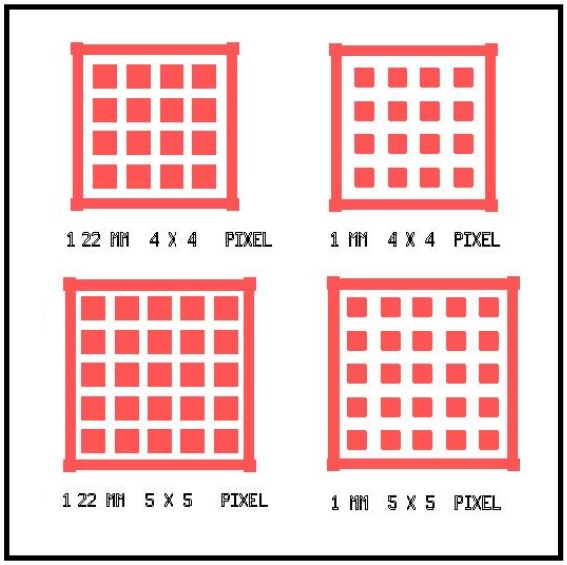

Figure 3.3: *Design of mask plate showing the layer of metal and passivation used to build up the pixelated structure used in this study.*

The JWNC technical staff prepare the masks (which are bought in as quartz plate coated with 100 nm of chrome) by spinning the e-beam resist on top of the chrome. After exposure and development, the chrome is etched away using chemical wet etch and any remaining resist is removed using a barrel asher - leaving the original pattern transferred onto the chrome. Multiple copies of the chrome master can then be made using a contact printing technique. The mask copying process introduces a slight loss of resolution but this is not important for the large feature sizes that are present in this study. Fig. 3.4 shows one of the mask plates used in our work.

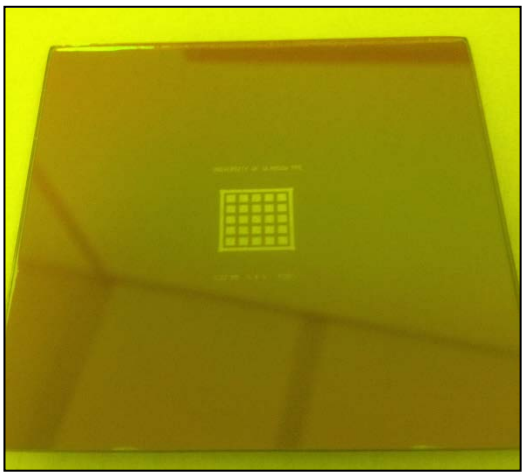

Figure 3.4: *Mask plate for the metal layer of the 5x5 pixel matrix.*

3.3.4 Photoresist

Photoresist is a radiation-sensitive compound dissolved in a solvent that is used to produce a liquid with a very precise viscosity. Resists can be classified as either positive or negative resist. For a positive resist the compound forms cross links in the bake after spinning and incident radiation breaks these links so the exposed regions become more soluble and can therefore be removed easily in the development process. The net result is that the patterns formed in the positive resist are the same as those on the mask. For negative resists the baking drives off the solvent but does not encourage cross linking in the photosensitive compound. As the resist is exposed through the mask the radiation causes the compound to cross link and so the exposed regions become less soluble and the patterns formed in the negative resist are the reverse of the mask patterns. Fig. 3.5 shows the pattern with different resists.

Positive photoresist consists of three components: a photosensitive compound, a base resin, and an organic solvent. Prior to exposure, the photosensitive compound is insoluble in the developer solution. After exposure, the photosensitive compound absorbs radiation in the exposed pattern areas, changes its chemical structure, and becomes soluble in the developer solution. Upon development, the exposed areas are removed.

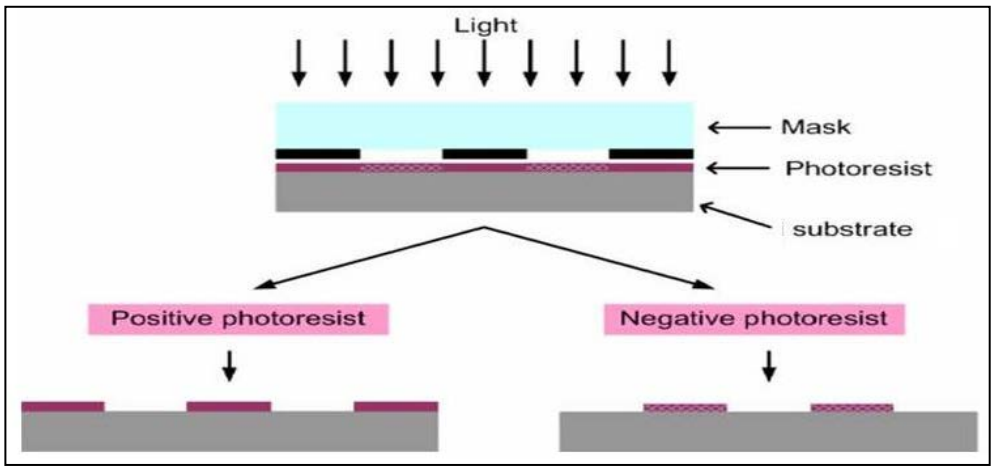

Figure 3.5: *Photoresist pattern with positive and negative resists*

Negative photoresists comprise of polymers combined with a photosensitive compound. After exposure, the photosensitive compound absorbs the optical energy and converts it into chemical energy to initiate a polymer linking reaction. This reaction causes cross linking of the polymer molecules. The cross linked polymer has a higher molecular weight and becomes insoluble in the developer solution. Upon development, the unexposed areas are removed. One major drawback of a negative photoresists is that in the development process the whole resists mass swells through the absorption of developer solvent. This swelling action limits the resolution of negative photoresists.

The resist used for this project was Shipley S1805. This is a positive tone resist which is photosensitive to UV light with a wavelength from 350 nm to 450 nm. The thickness of the resist film can be controlled by the spin speed / acceleration. The pattern resolution depends on the film thickness but in this work, it was chosen use the standard processing parameters as the feature sizes are not too demanding (see Fig. 3.6).

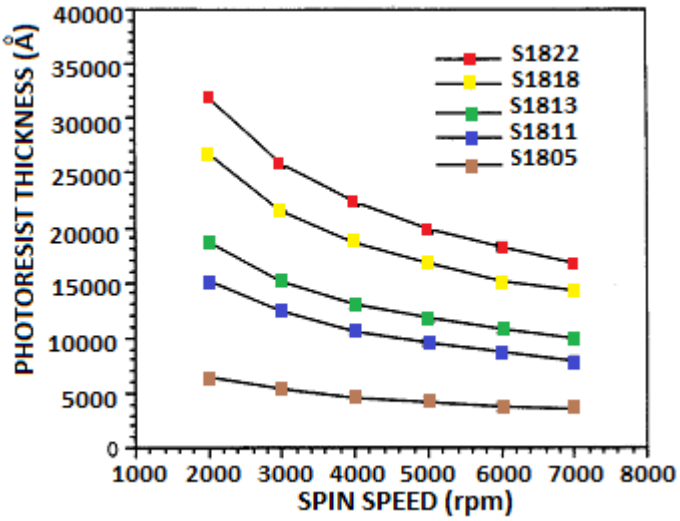

Figure 3.6: *Spin speed curved of Microposit S1800 photo resist series [42].*

To apply the photoresist to the surface of the substrate, the substrate is placed on a vacuum chuck in a laminar air flow (LAF) cabinet. This chuck is able to spin round at a speed determined by the user (measured in revolutions per minute (rpm)). A HDMS (*hexamethyldisilazane*) based microposit primer is applied to the surface of the substrate and spun for 5 seconds at 4000 rpm. The HDMS primer is used to improve photoresist adhesion to oxides. The HDMS reacts with the oxide surface to form a strong bond to the surface of the substrate. At the same time free bonds are left which readily react with the photoresist, enhancing the photoresist adhesion.

The S1805 photoresist is then applied to the substrate in small quantities using a filtered syringe to remove any particulate residue, and is spun at a 4000 rpm for 30 seconds. After photoresist spinning, the substrate is put onto a hotplate for a soft bake in two stages; 60 ^{o}C for 2 minutes and 80 ^{o}C for 3 minutes to remove any solvent in the resist. The substrate is then loaded into the mask-aligner Karl Suss MA6. The substrate is then aligned accurately to the pattern on the mask using the MA6 microscope and exposed to the UV light (365 nm for 5 seconds). The exposed resist is then developed using Shipley Microposit Developer Concentrate. The recipe used in the development process is a 1:1 solution of Shipley Microposit Developer Concentrate: Reverse Osmosis (RO) water. The exposed substrate is immersed in the developer solution for 3 minutes and then rinsed in RO water for a further 2 minutes.

3.3.5 Oxygen Asher

After rinsing away the solvent, any residual resist in the developed area is removed using an Oxygen Barrel Asher – a Gala machine. This step generates a low power oxygen plasma in a barrel shaped chamber. The reactive oxygen ions etch the resist very selectively which cleans off any remaining resist residues.

3.3.6 Metallisation and lift-off

The metal deposition used to produce our pixellated structures with an ohmic contact uses electron-beam evaporation with a rotating crucible permitting a series of different (up to 6) different metal targets to be evaporated during a single run. The metallisation takes place in a vacuum chamber in the Plassys MEB 550S evaporation system which is used to deposit *Pt* on our substrate during the fabrication. Once the substrate is loaded into the evaporator, the chamber is pumped down to the process pressure (2×10^{-6} Torr) and the desired metal scheme is selected via control software, in our case this is *Pt*. In order to initiate the evaporation, the selected metal target in the crucible is heated over its melting point by a beam of electrons and the metal evaporates into the vacuum and onto the substrate surface where it condenses as a thin film on the substrate surface.

The metallisation step is followed by a 'lift-off' which is used to remove the resist mask and unwanted metal. One of the advantages of an evaporated deposition is that it is highly directional so that no metal is deposited on the sidewalls of the developed resist. This causes a break in the metal layer continuity along the profile of the resist/surface interface. The substrate is then sprayed with acetone where any remaining resist is subsequently dissolved. This leaves only the areas which are exposed during the lithography with metal, as shown in Fig. 3.7.

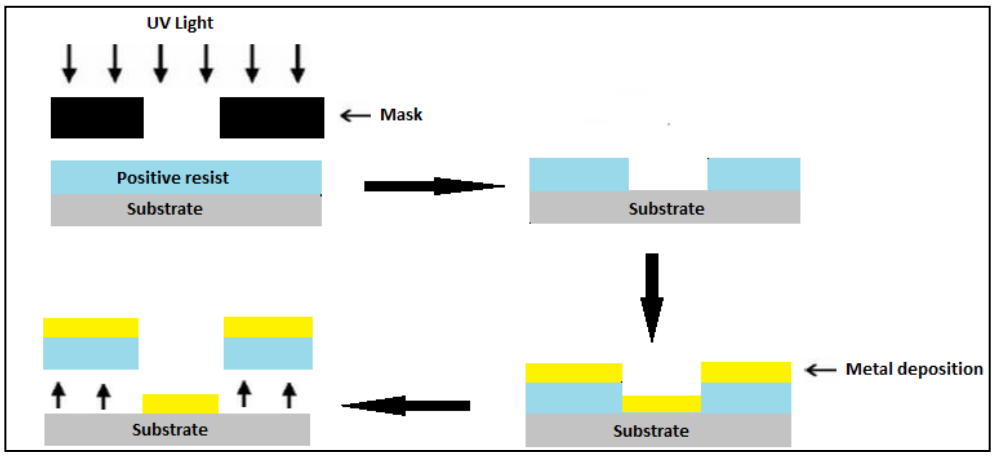

Figure 3.7: *The process sequence showing lithography, metallisation and lift-off used to define the pixel detector.*

3.4 Passivation

This process was proposed as a technique to produce a low surface interpixel leakage current for the *CZT* pixellated detector in order to improve its spectroscopic performance. To reduce surface leakage current and enhance detector performance surface treatment (passivation) has been used as part of the pixel fabrication process. The passivation layer is deposited after contact deposition. The selected process deposits a uniform layer of a dielectric material on top of the pixellated structure/ anode surface. Previous methods of passivation include variations of the wet etch typically used after mechanical polishing, wet chemistry surface oxidation using peroxides [43, 44] and atomic oxygen bombardment [45]. Chemical etching with a Bromine-Methanol solution leaves the *CZT* surface rich in *Te* and is considered to be one of the primary causes of increased surface leakage current in *CZT*.

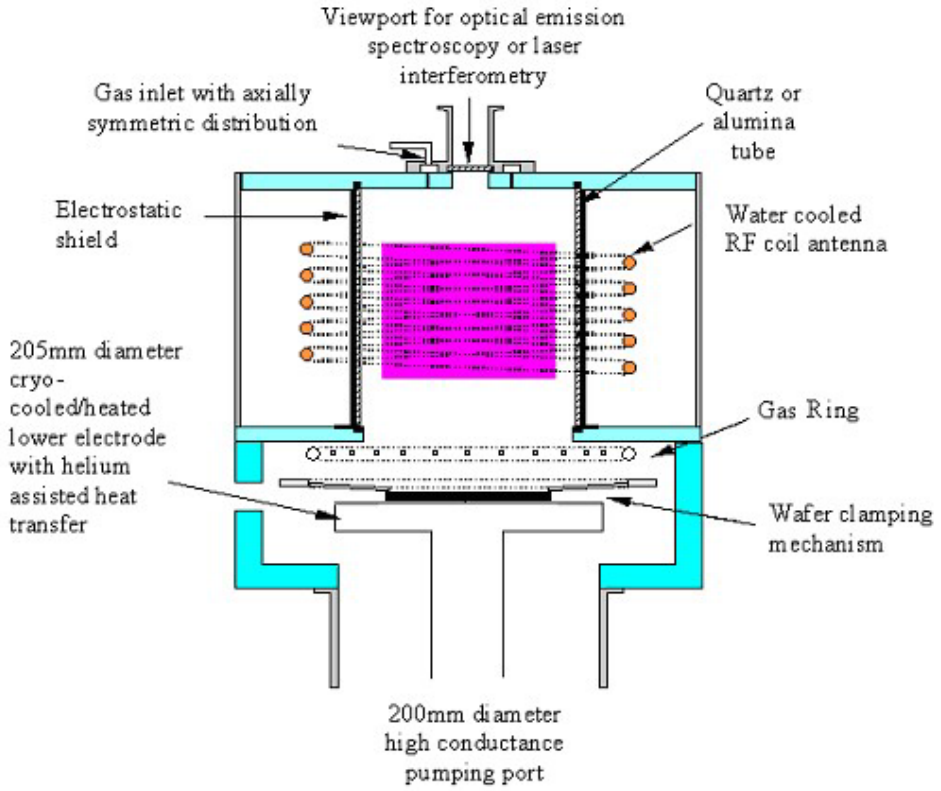

Figure 3.8: *Schematic of an ICP Deposition Tool [41] which was chosen as the preferred technique to deposit a high quality layer of SiN on the CZT substrate.*

SiN has been chosen as the dielectric material to effect this surface passivation as the deposition process for this material is well characterised and lays down a highly uniform layer of material. The *SiN* is deposited using an Inductively Coupled Plasma (ICP) Deposition Tool. In this technique the deposition of *SiN* is done at room temperature to eliminate potential thermal damage to the very thermally sensitive *CZT* substrate. Fig. 3.8 shows a schematic of ICP deposition system used to carry out the deposition of our passivating layers. Silane and dopant gases are fed through the gas ring located just above the substrate/wafer. This minimises the deposition in the source area and reduces the need for cleaning. The operating power levels of the ICP deposition system are up to 2 kW and this level of RF power provides higher plasma densities with up to 10^{18} electron m^{-3} and operating at a low pressure of 1-20 mTorr. These conditions increase the mean free path of the ions in the plasma and cause little scattering of the ions or active species before they hit the substrate.

After depositing the passivation layer using the ICP deposition system, the substrate is prepared for a second lithography step. The process steps applied are similar to the ones described in Section 3.3.4 but excluding the development process. The substrate is then ready for dry etching – to remove selected areas of the passivation layer on the substrate. This technique used BP80+ RIE machine. RIE is a technique that removes the undesired material through the combined effect of chemical and physical interaction with accelerated ions. RIE produces both strongly anisotropic etch profiles and good selectivity between the mask layer and the material to be etched. RF power applied to two parallel plates is used to control both plasma generation and ion acceleration and so it is possible to control etch rate. Table 3.1 show one of the parameter involved in etches process. After completing the dry etching process, the substrate is flushed with acetone to remove the resin on the substrate. Fig. 3.9 shows the image of the substrate after the fabrication process is completed.

Table 3.1: *RIE process parameters used for the nitride etch.*

PARAMETER	**RUN 1**
Process Gas Required	CHF_3/O_2
Etch Depth (nm)	500 nm
Table Temperature (^oC)	22
Gas Flow (sccm)	50/5
Process Pressure (milliTorr)	55
Rf Power (W)	150
Processing Time (minutes)	10:00

In order to confirm the etching process produced the desired etch depth, a surface measurement as been performed. This was done with a Dektak 150 surface profiler. Using the recipe in Table 3.1 show the etch depth was designed to be around 500 nm. Fig. 3.10 shows the interface measurement of Dektak 150 surface profiler which indicates a physical etch in good agreement with the target depth.

Processing time is one of the critical parameter to control the etch depth of the sample. From the calibration graph for RIE system provided by technician staff at JWNC the ecth rate is 50nm/min. So if our process requires an etch depth of 500 nm it takes around 10:00 minutes.

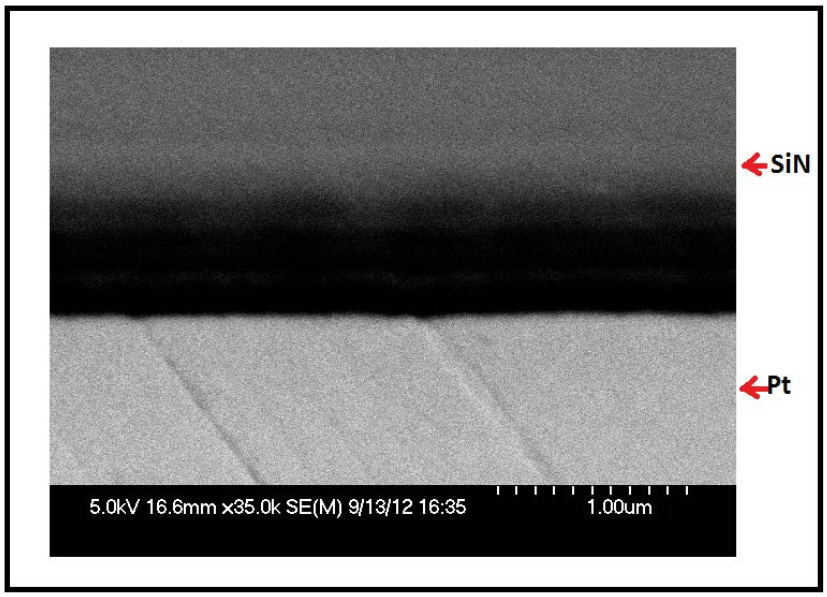

Figure 3.9: *SEM images showing the result after the complete fabrication process.*

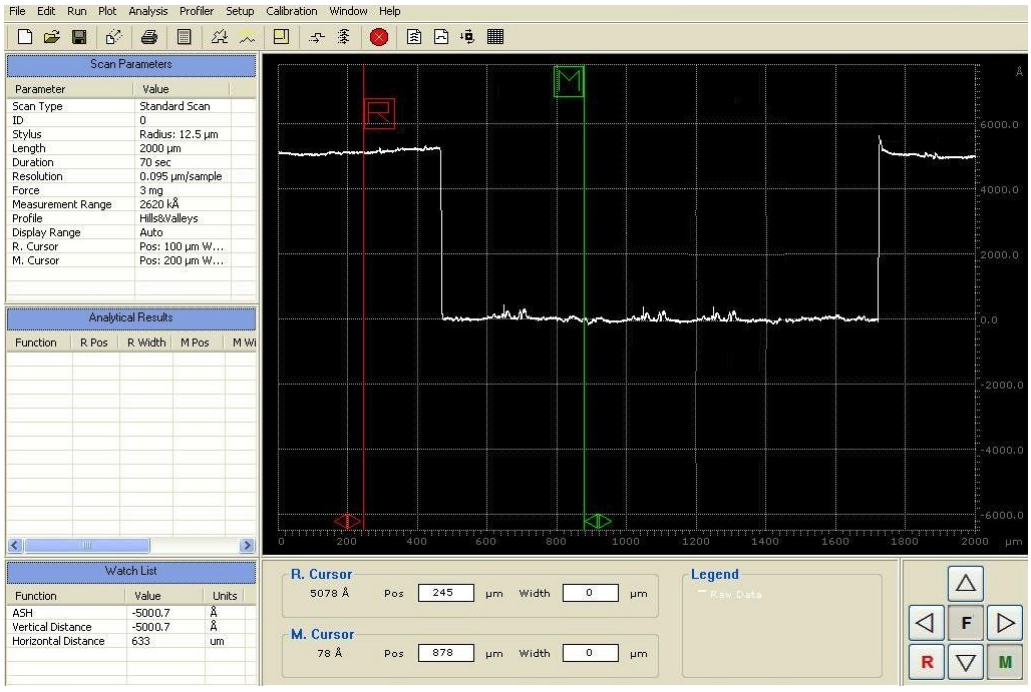

Figure 3.10: *Interface of Dektak 150 Surface Profiler showing the etched trench.*

3.5 Electrical Characterisation

Bulk leakage current and surface leakage current are two parameters that contribute to total leakage current of the semiconductor spectrometer. It is obvious that the bulk leakage current is affected by material resistivity ρ (Ω.cm); while the surface morphology and stoichiometry of the device affects the surface leakage current. It has been measured and reported that the total leakage current for unpassivated *CZT* radiation detectors is dominated by surface leakage current rather than the bulk leakage [46]. The study of *CZT* detector leakage current is very important because it has the effect of degrading the energy resolution as a result of the electronic noise due to it at the output of the charge-sensitive preamplifiers [47]. In order to solve this problem, surface passivation for *CZT* detectors is important in the fabrication of gamma-ray detectors [48]. Surface passivation plays a dominant role in reducing the surface leakage current and therefore decreasing the noise and improving the spectral energy resolution of the detectors.

During the process of CZT substrate preparation, mechanical polishing and chemical etching always induce surface damage, dangling bonds, a non-stoichiometric surface and surface roughness, which are considered as the primary sources of the high surface leakage current. Chemical etching with a bromine-methanol (BM) solution leaves the *CZT* surface rich in *Te,* and is considered as one cause of increased surface leakage current [49]. Various chemical passivation processes that reduced the surface leakage current of CZT detectors have been previously reported, mainly including H_20_2 [49], NH_4F/H_2O_2 [50], *KOH* [51] etc. NH_4F/H_2O_2 reacts with the Te-rich layer on the substrate and converts it to TeO_2, and so is a good passivating agent, through this processing, the oxidation of the *Te* excess is not quite complete and leaves residual *Te* still present deep in the oxide layer [50]. This would affect its electrical properties because the residual *Te* present in the layer could still be electrically active. In this study, we have explored alternative methods of oxidizing a *Te*-rich surface via an oxygen plasma and passivation by Inductively Coupled Plasma SiN which can yield superb passivating capability. All the process steps involved in this study have been discussed earlier in this chapter.

A dedicated experimental setup for leakage current measurement has been developed. The diagram of the experimental setup is shown in Fig. 3.11. In this project we have used a Wentworth S3000 probe station, a custom made probe card, a Keithley 6485 picoAmmeter, a Keithley 7001 Relay switch and a Keithley 237 source-measurement unit to precisely measure the Current–Voltage (I-V) characteristics. The CZT detector is placed on the chuck of the wafer prober and a vacuum applied through the chuck to make sure the sample does not move during the measurement process (Fig 3.12). Meanwhile, I-V characteristics are recorded using LabView program "Pixellated_CZT_TestCentre.vi" interfacing with a picoAmmeter/voltmeter source/Relay switch. Fig. 3.13 shows the interface (GUI) of the software developeded for this study. The scan mode performs as an automated measurement for all pixels involved through probe card and it is controlled for each measurement through switching by Keithley 7001 relay switch.

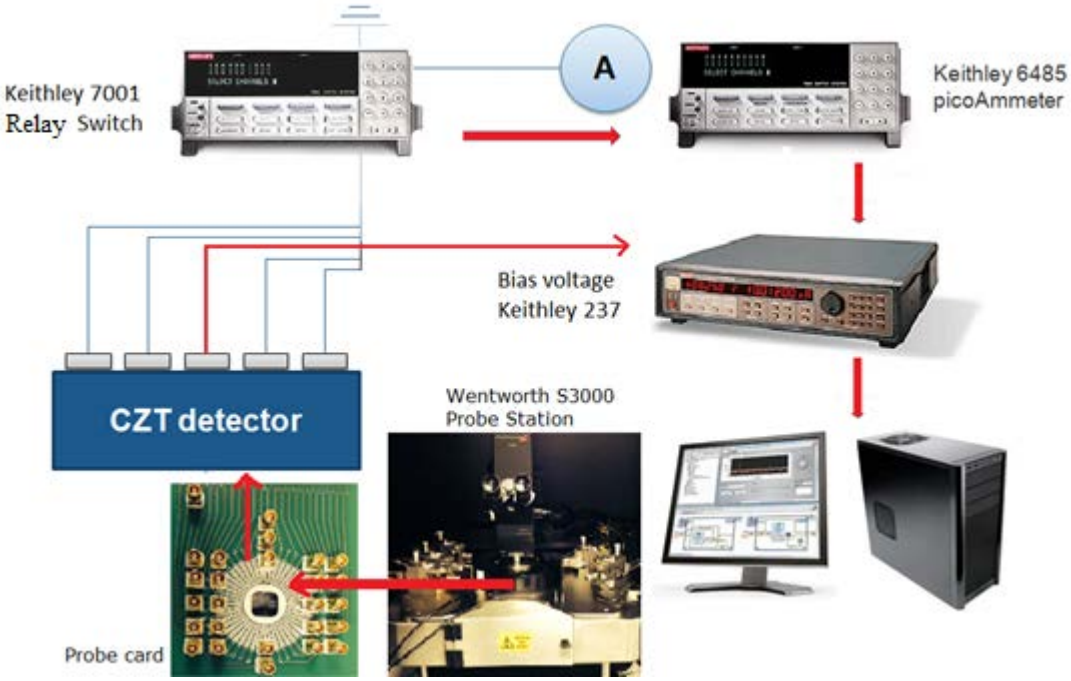

Figure 3.11: *Diagram of I-V Measurement*

In terms of leakage current, the two types of leakage current measurement being studied are interpixel surface leakage current and bulk leakage current. For interpixel surface leakage current measurement, two techniques are used whereby the chuck is positioned as either a floating or grounded point. Here, for both measurement work, the

probe needle is positioned and the bias is applied to the centre of the pixel while the neighbouring pixels are being measured with the chuck (cathode) in floating or grounded. This is to find out whether the change in the chuck setup has an influence on the results in the leakage current readings. Meanwhile for the bulk leakage current the bias voltage is applied to the Chuck (cathode) and the leakage current is measured at the anode (centre of pixel) by using the picoAmmeter. In scan mode, the bias voltage is stepped from 0 to 100V for both polarities to investigate the variation of leakage current from pixel to pixel.

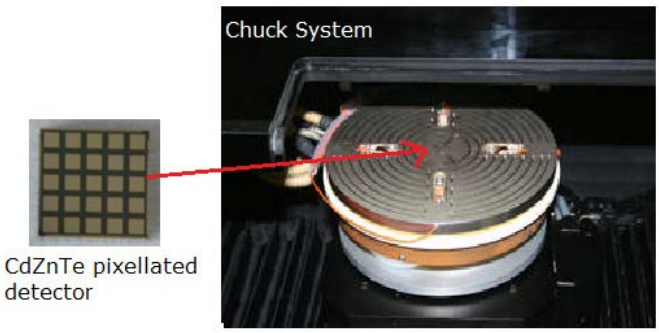

Figure 3.12: *Chuck system of Wentworth S3000 probe station*

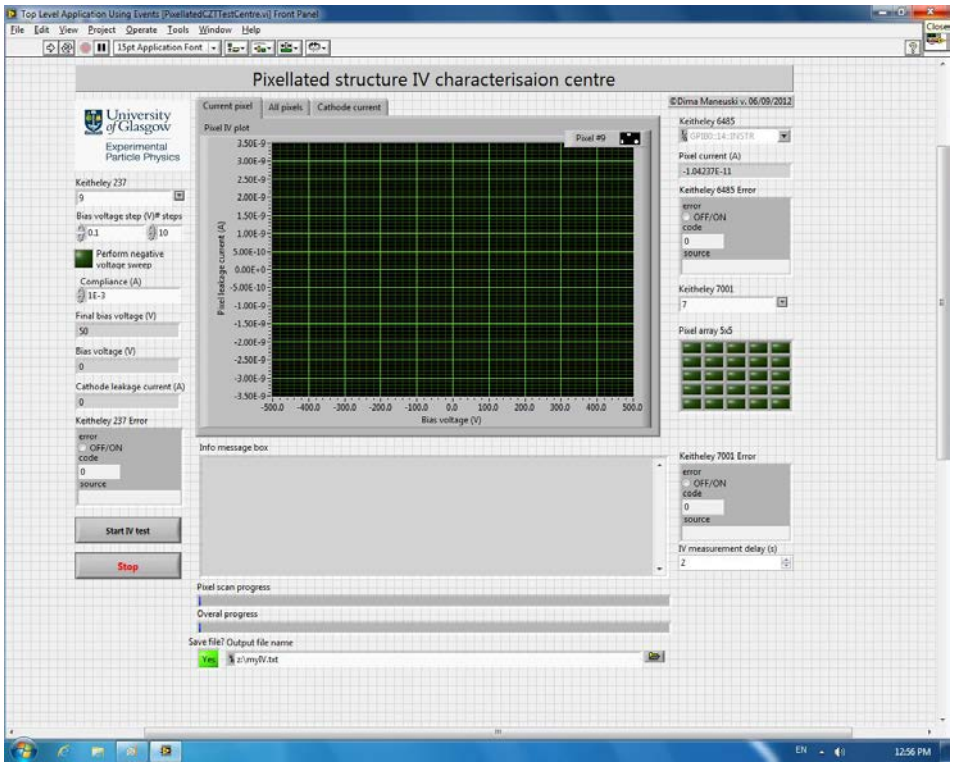

Figure 3.13: *Interface of I-V measurement software*

I-V System Setup Verification

In order to make sure the setup of I-V measurement is reliable and also produces accurate data, the system has been tested using a sample of polycrystalline diamond. The reason for choosing diamond as the sample for testing the I-V setup is because of its properties. As diamond has an indirect band gap it functions well as an insulator with the capability of being a semiconductor. Diamond detectors usually exhibit a p-type semiconductor behaviour with a boron impurity at an energy level of 0.37eV above the valance band [52]. Table 3.2 shows the electric properties of a diamond [53].

Table 3.2: *Electric properties of diamond*

Property	**Value**
Mass density	3.515g/cm^3
Band gap energy	5.5 eV
Lattice constant	3.567 Å
Young's modulus	1050 GPa
Resistivity	>1014 Ωm
Hole mobility	2100 cm^2/V.s
Electron mobility	2000cm^2/V.s

The samples were fabricated in the same pixellated design. The anode and cathode contacts are realised by depositing gold to produce *ohmic* contacts. A structure with simple *ohmic* electrodes in both sides of the diamond detector was fabricated. Fig. 3.14 shows the layout of the pixellated diamond detector.

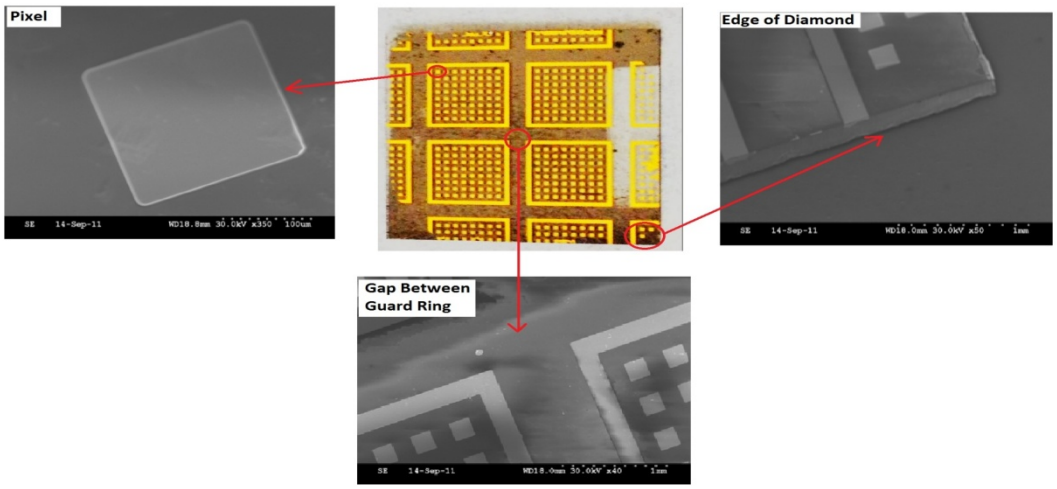

Figure 3.14: *Pixelated diamond detector.*

The measurement of bulk leakage current is arranged so that the bias voltage is applied to the cathode and the setup also measures the leakage current at the anode by using the picoAmmeter. The bias voltage is stepped from 0 to 1 kV for both polarities to investigate the variation of leakage current from pixel to pixel. The leakage current is measured at room temperature with the bias voltage applied to the anode. Fig. 3.15 shows a typical leakage current measurement taken from A2 pixel #2. When the bias voltage is applied up to 1.0 kV, there is no break down and the leakage current of the diamond detector is only 7pA.

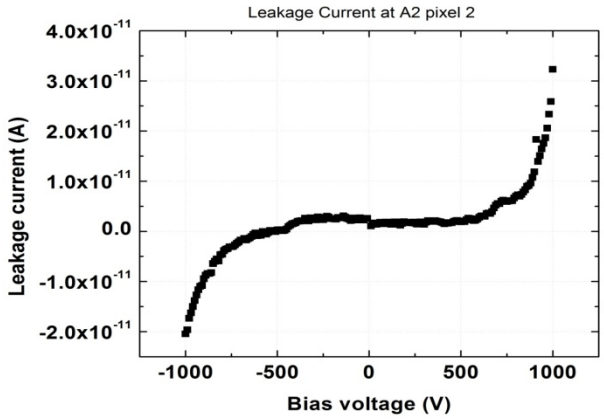

Figure 3.15: *Bulk leakage current of polycrystalline diamond pixellated detector.*

In order to assess the stability of the I-V measurement setup the bias was swept from 0V to 1000V in steps of 10V then back from 1000V to 0V and then to -1000V and back to 0V. The result in Fig. 3.16 shows no polarisation effect and also no appreciable fluctuation of the current on successive passes.

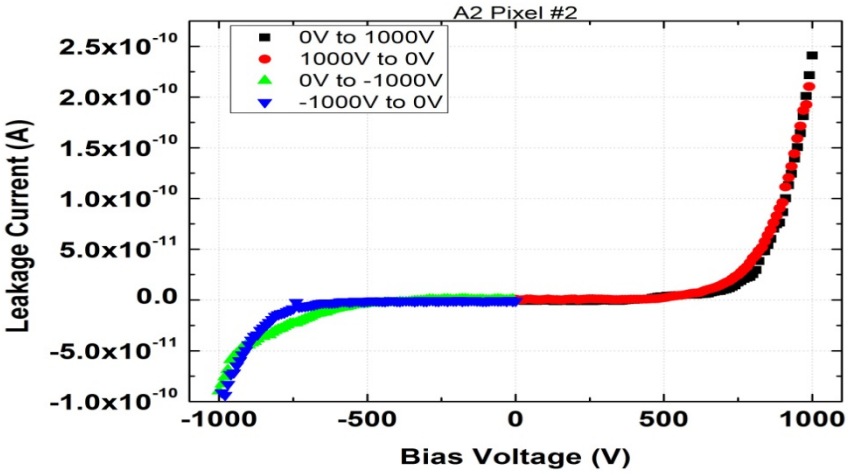

Figure 3.16: *Different magnitude of bias voltage*

From the measurement taken it shows that the setup of I-V measurement is capable of measuring a very low leakage currents down to picoampere level. The system set-up shows that the data produced from the system is reliable and is not influenced by the noise from the cable, probe needle and other electronic equipment. The setup here is applied to measure the leakage current of CZT pixellated detector.

I-V measurements of CZT pixellated detector

Bulk Leakage Current

The CZT samples used in these studies are not of the high quality detector grade material that is still under laboratory development to refine the growth technique (Kromek) to produce high quality material suitable for detector fabrication. However, this study is intended to show that the process of passivation developed will give a desired reduction of leakage current regardless of the quality of the materials used in the sampling.

Fig. 3.17 shows the pixel numbering scheme used during the I-V measurement. For the bulk leakage current measurement, pixel # 13 was measured. This pixel is located at the centre of the pixel arrangement. Pixel # 13 (anode) has been chosen to study the effect of charge produced from the neighbouring pixels after being injected with bias at chuck (cathode).

The I-V measurement was done on the CZT samples where the process involved; oxygen plasma surface oxidation and 200 nm SiN passivation. Special precautions have been taken in order to ensure a steady state current during the measurement. Because of the presence of deep levels in the forbidden gap of CZT material, it can take several minutes or even hours to reach equilibrium between free and trapped carriers. To reduce the waiting interval between measurements, the bias on the contacts is varied in small steps. To be more specific, after setting a new set of contact biases, the measurement is paused for 10 minutes before taking 100 sequential measurements of the current, separated in time by 5 sec intervals. This sequence of data points ensures that the equilibrium current has been actually achieved, and also increased the accuracy of the measurements. All the measurements have been done at room temperature and in the dark inside the Wentworth S3000 probe station. The CZT is very sensitive to light. Fig 3.18 shows the effect of UV light during measurement. When the UV light is on the leakage current is very sensitive and increases immediately up to 10^{-6} A and when inside the dark side it is around 10^{-9} A.

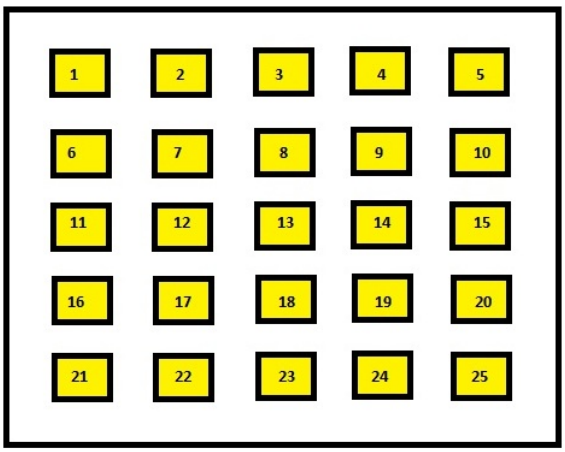

Figure 3.17: *Arrangement of pixel # number.*

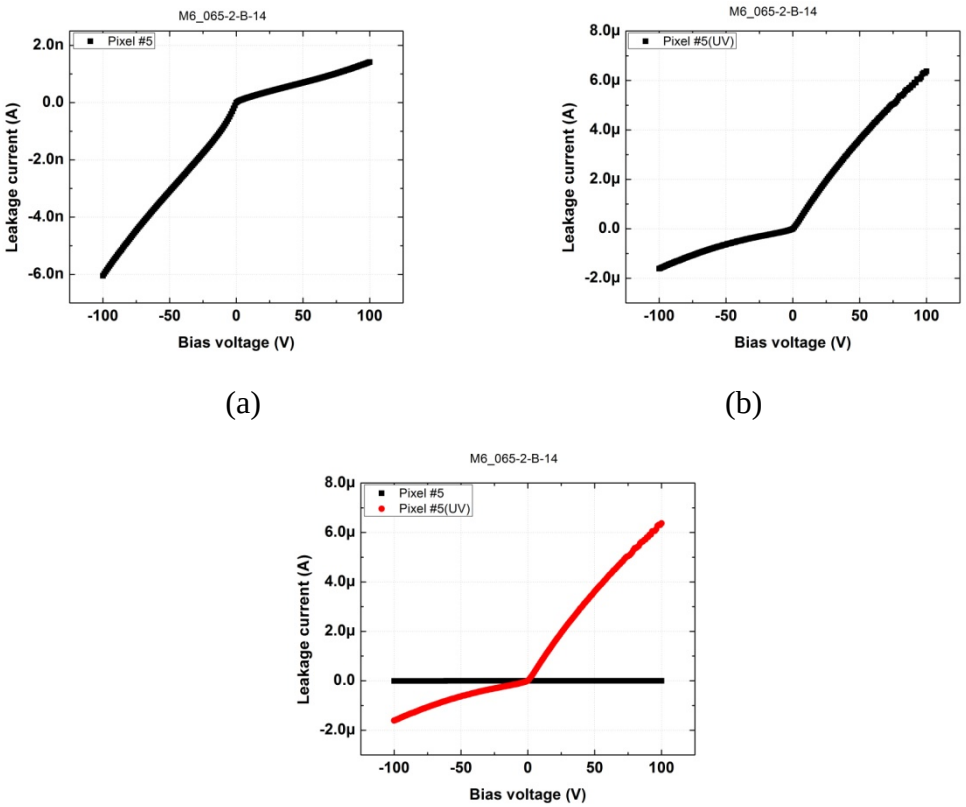

Figure 3.18: *Effect of UV in measurements: (a) Without UV light (b) UV light is on (c) Combination of data*

The results of of the bulk leakage current measurement for the passivated and untreated CZT detector are shown in Fig. 3.19. The measurements show that a passivation layer of 200 nm SiN and an oxygen plasma oxidation substantially reduces the leakage current of the detector. Passivation reduces the bulk leakage current measurement of the pixel by about an order factor by 3 compared to the sample without passivation for a negative bias. The result also shows that the sources of the bulk leakage current are not only from internal resistivity and defect of CZT material. Another source of bulk leakage current can also arise from the charge concentration produced in between the neighbouring pixels on the surface of CZT pixellated detector. Based on a comparison of the bulk leakage current results, the passivation technique shows that it may be possible to reduce effects due to charge trapped at the surface in the interpixel region

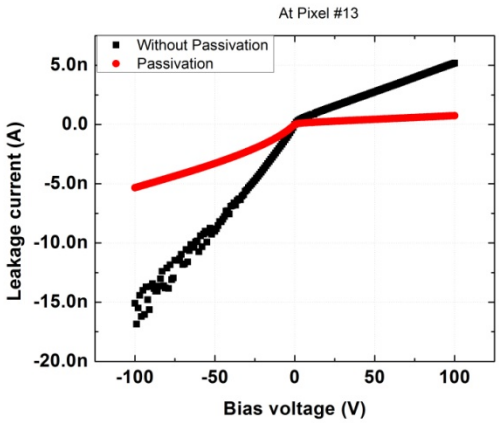

Figure 3.19: *Bulk leakage current of CZT pixellated detector*

The shape of the I-V curve plotted in Fig: 3.19 indicates that the curve is non-linear although the contact deposited in the fabrication is supposed to behave as an Ohmic contact. A highly asymmetric I-V curve is shown in Fig: 3.20. These asymmetries in I-V characteristics do no real harm, since the detector can be biased with the polarity that gives the lower leakage current. The result findings of this study are within the range of the results published by other researchers [5].

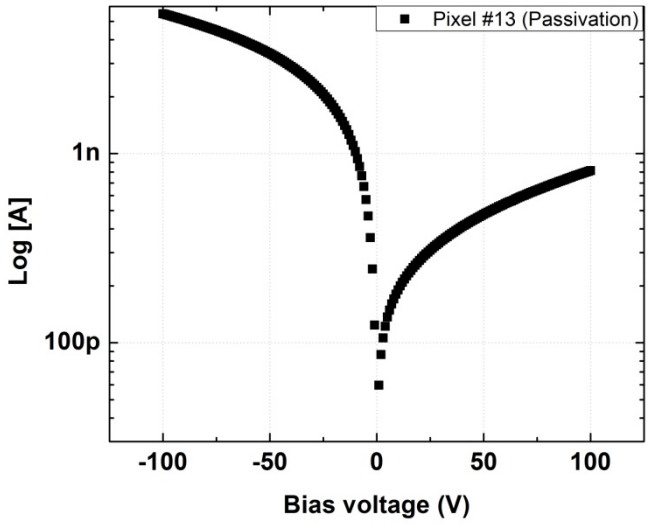

Figure 3.20: *Asymmetric I-V characteristic passivation CZT pixellated detector*

Fig. 3.21 (a) and (b) are the results of the fitting procedure to measure resistivity of CZT pixelated detector. Here, the data obtained from the fitting procedure are within ±2V. From the graph, the resistance for the SiN passivation + oxygen plasma oxidation is 1.19 $x10^{10}\Omega$ and without passivation is 1.23 $x10^{9}\Omega$. Based on the calculation the resistivity of the SiN passivation is 5.9 $x10^{10}$ Ωcm and 6.2 x 10^{9} Ωcm for CZT sample without passivation. SiN passivation provides the results that there is an increase of resistance and resistivity both by around a factor of 10. As mentioned previously the CZT samples used in this study are not detector quality material so the starting resistivity without passivation is 10^{9}. In theory the resistivity, of CZT samples should be greater than 10^{10} where the additional Zn functions to increase of resitivity of CZT material.

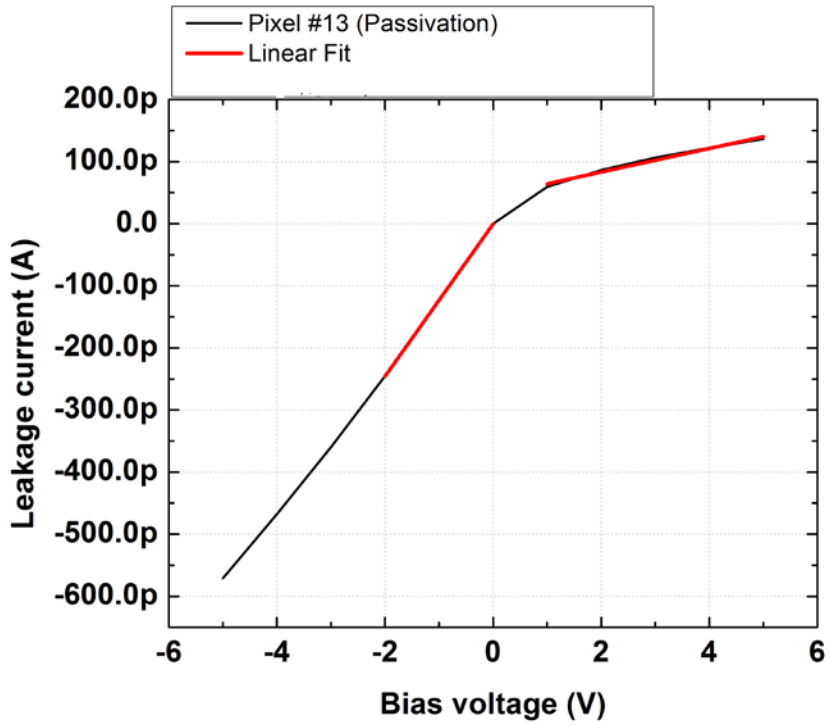

(a)

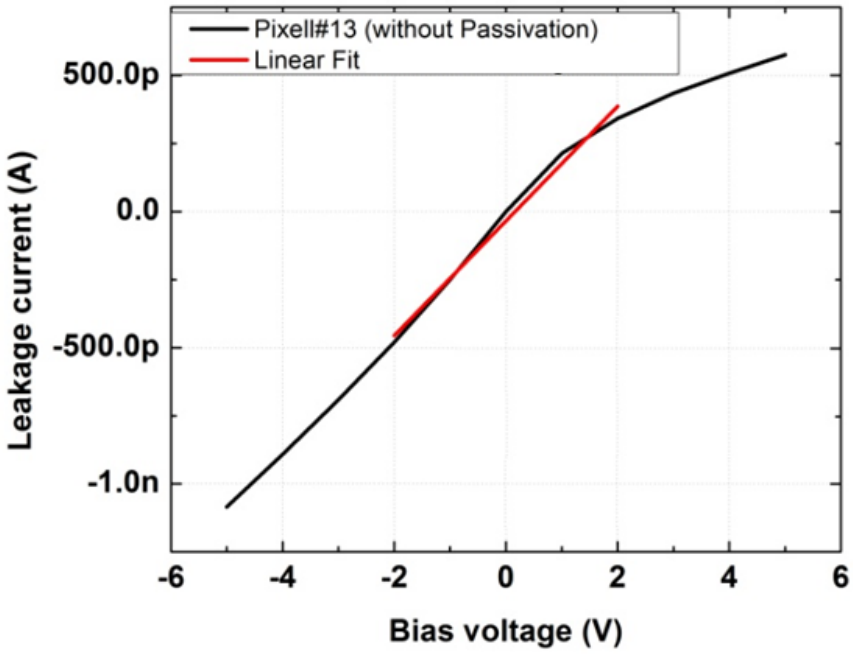

(b)

Figure 3.21 : *I-V Characteristic of resitivity of bulk leakage current (a) Passivation (b) Without Passivation.*

Interpixel Leakage Current

Maximising size of surface interpixel leakage current have been carried out with two arrangements. The difference between Technique 1 and Technique 2 is only how the chuck (cathode) is electrically connected. As for Technique 1 the chuck is grounded and meanwhile for Technique 2 it is floating. Bias was then supplied to pixel no 13 and neighbouring pixels; #8, #12, #14, and #18 were measured automatically in order to measure the interpixel leakage current. The results of the measurements of interpixel leakage current are shown in Fig. 3.22 (a) and (b) for both techniques. Technique 1 indicates that the interpixel leakage current is lower compare to the one measured with Technique 2. Despite the striking result obtained from Technique 1 (the occurence of low leakage current), it is not a true measurement of interpixel leakage current measurement. This is beacuse when the chuck is at ground it changes the potential distribution inside of the CZT sample and some of the charges go towards to ground.

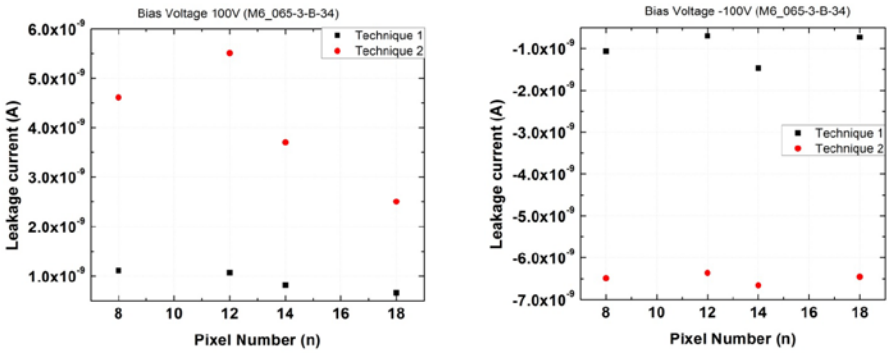

(a)

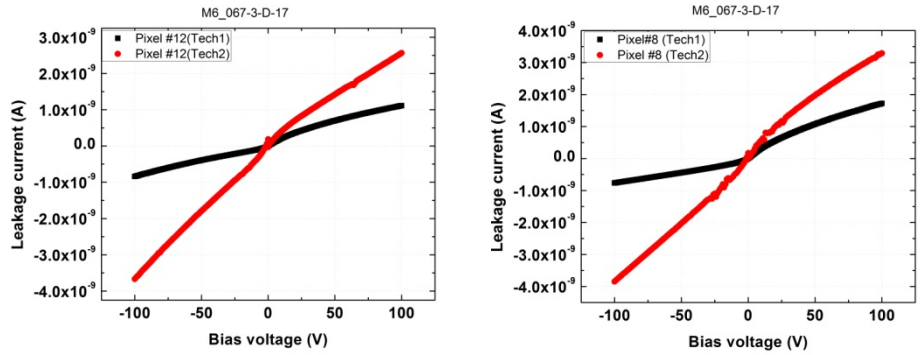

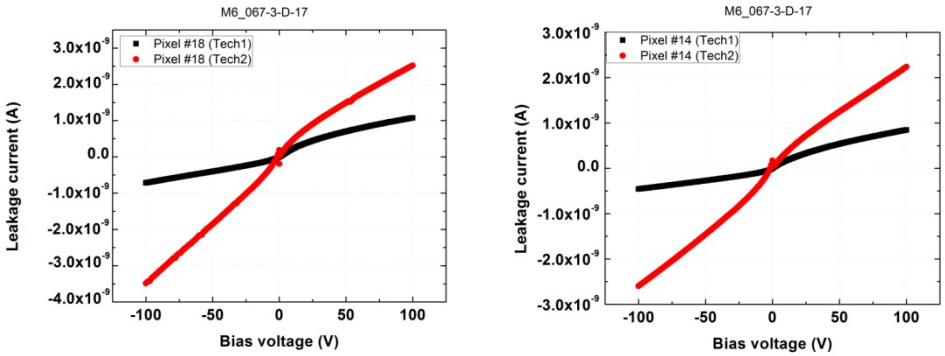

(b)

Figure 3.22: *Interpixel leakage current different techniques: (a) M6_065-3-B-34 (b) M6_067-3-D-17*

Fig. 3.23 shows the result of interpixel leakage current measurement. Section (a) is the result of the bias at 100V and (b) for -100V. This indicates that the passivation technique with SiN results in a large reduction of interpixel leakage current. The improvement of this passivation for all interpixel measurement is around 86 % . Table 3.3 shows the summary of the interpixel leakage current measurement results. To summarise, the oxygen plasma used in producing TeO_2 and also with the superb passivation of SiN, they are capable of producing a promising result for low interpixel leakage current.

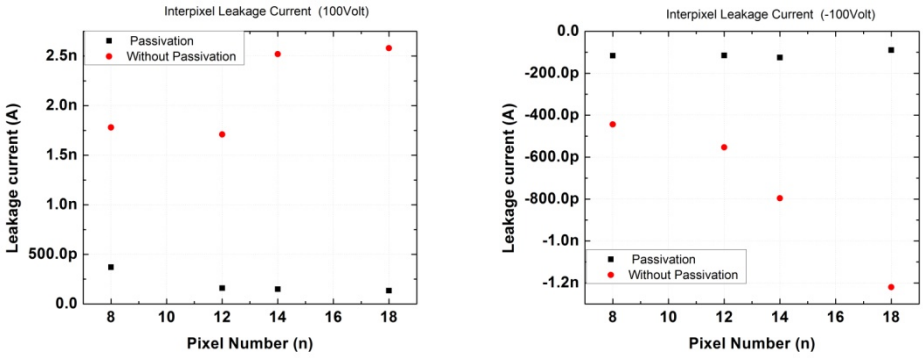

(a) (b)

Figure 3.23: *Interpixel leakage current passivation(200 nm): (a) 100 V (b) -100 V*

Table 3.3: *Summary of interpixel leakage current (200 nm)*

Pixel #	Bias Voltage (V)	Pre-Passivation (A)	Post-Passivation (A)	% Improvement (A)
8	100	1.78E-9	3.71E-10	79
	-100	-4.44E-10	-1.16E-10	74
12	100	1.71E-9	1.6E-10	91
	-100	-5.53E-10	-1.15E-10	79
14	100	2.52E-9	1.49E-10	94
	-100	-7.96E-10	-1.25E-10	84
18	100	2.58E-9	1.34E-10	95
	-100	-1.22E-9	-8.94E-11	93

In order to study the effect of different thicknesses of SiN; 400 nm and 500 nm thick layers have been deposited. Fig. 3.24 and 3.25 show the result of interpixel leakage current for different SiN layer thickness. All the measurements for 500 nm and 400 nm SiN show an improvement of low leakage current that is around an 85% reduction in leakage current. The findings show similar results to those obtained with the 200 nm SiN passivation layer. For pixel# 8 and #12 in 400 nm thickness of SiN there is almost no difference in interpixeal leakage current. The only difference seen is when the bias is close to 200 V. This is because of the presence of a defect near the surface of the material probably introduced during the polishing process. These studies are also conducted using bias from -500 V up to 500 V. All of these measurements show the trend that when the bias is up to 200 V and -200 V the current becomes saturated above this bias

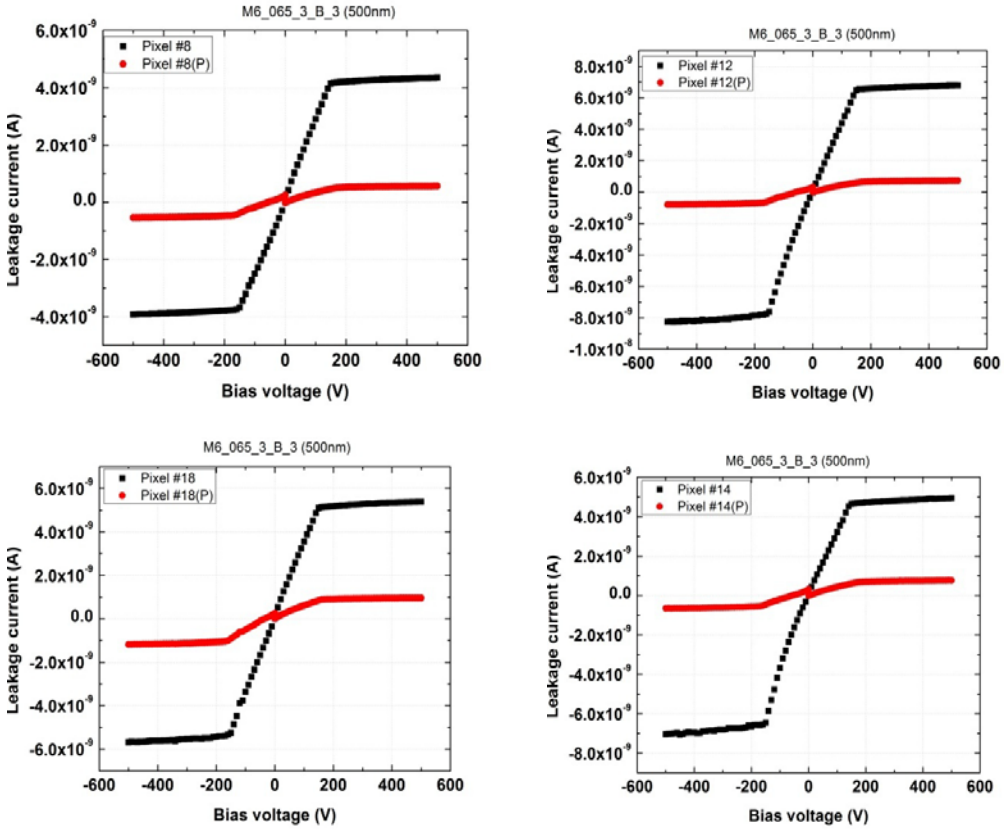

Figure 3.24: *Interpixel leakage current with 500nm SiN passivation layer*

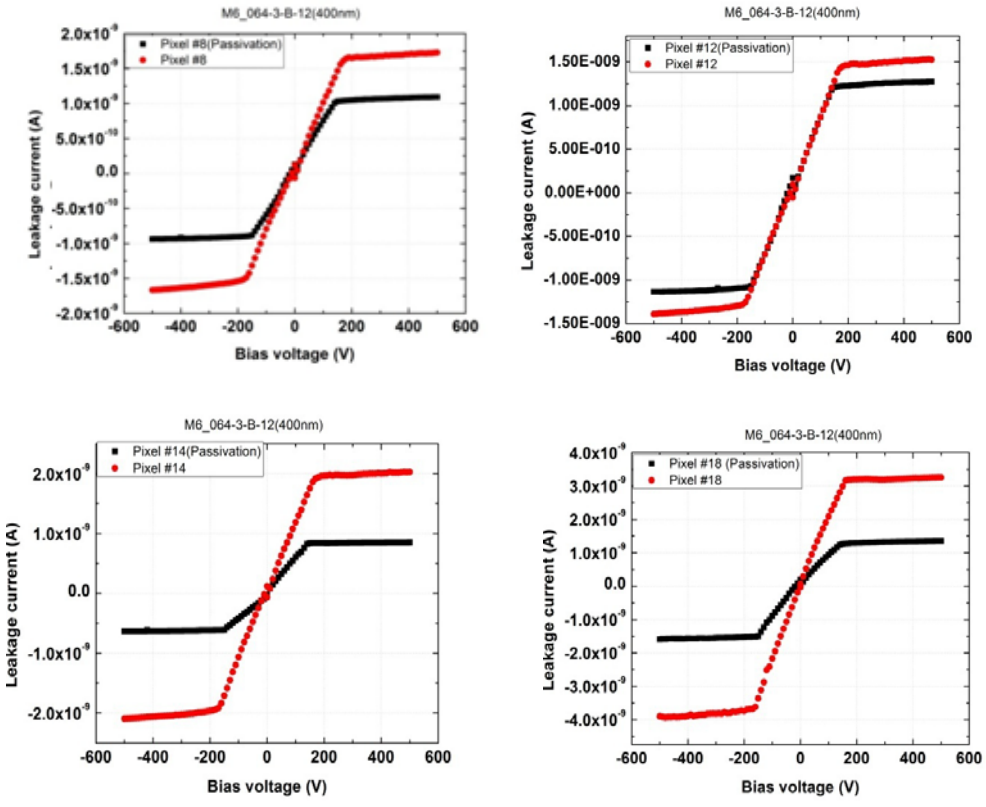

Figure 3.25: *Interpixel leakage current with 400nm SiN passivation layer*

Spectrum Energy

Radiation spectroscopy is an analytical technique which can determine the energy emitted from a given source/radionuclide. By connecting the right detector to an instrument known as a multi-channel analyser (MCA) the energy of the radiation can be represented physically as an image called a spectrum. An energy spectrum is a statistical count of events, which are "binned" into channels in the MCA. If the characteristic peak energy is known then the channel number can be calibrated in terms of energy. The width, or the full width half maximum (FWHM), of the peak describes the resolution of the detector. The FWHM is related to the resolution by,

$$R = \frac{FWHM}{X_O} \tag{3.1}$$

Where R is resolution, x_o is the mean.

A spectrum of *a CZT* pixelated detector for ^{57}Co has been studied. The spectrum from the ^{57}Co is analyzed without any correction of the charge collection. Fig. 3.26 shows the setup of experiment involved. Meanwhile, Fig. 3.27 shows the resulting spectrum of ^{57}Co taken with the *CZT* pixellated detector. The measurements are setup at 100 V, 100 gain and 1 μs amplifier shaping. MCA used in the experiment is known to have linear performance. Hence only one point was required for calibration 122 keV peak only was used to calibrate the system. The result shows for *SiN* passivation + oxygen plasma oxidation FWHM is 10.78 keV giving it an energy resolution is 8.8%. Meanwhile, without passivation the FWHM from the sample is 11.31 keV and energy resolution is 9.2%. The result also shows the *CZT* material used in this study has a has a slightly assymetric peak. This happens due to the poor charge transport properties of the material, electron-hole pairs generated in this sensor are not completely collected [54].

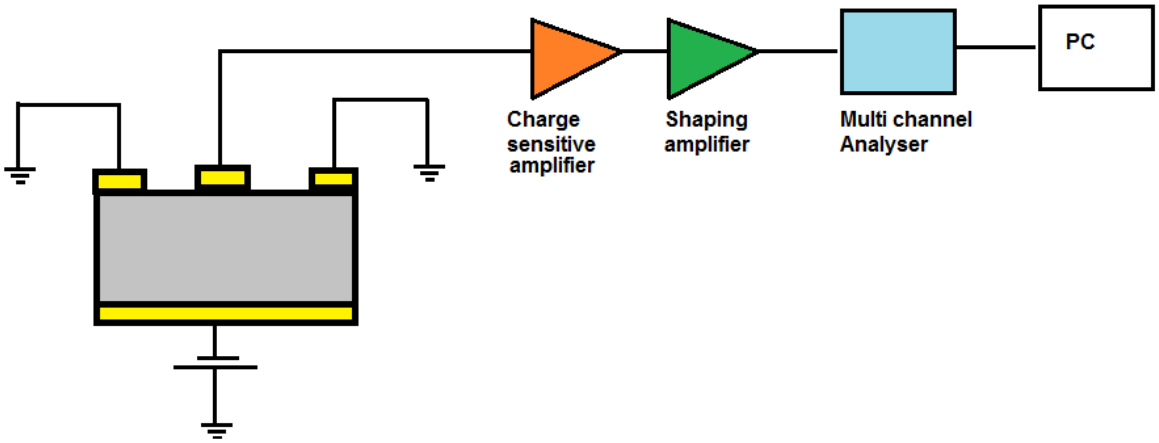

Figure 3.26: *Experiment setup for spectrum analysis*

Ideally, the detected energy of an incident photon is equal to the true photon energy. In reality, several effects in the detection process limit the ability of the detector to resolve the true photon energy. One effect is the stochastic generation of electron-hole pairs in the detector, while a second effect is incomplete charge collection due to the trapping of holes. A third effect is charge sharing between neighbouring pixels, which occurs when the energy deposited by an incoming photon is distributed between two or more detector pixels, resulting in each pixel measuring a lower energy photon. A fourth effect occurs when a *K-fluorescence* photon emitted during photoelectric absorption leaves the active pixel volume, causing the measured photon energy to be lower than the true energy. From the graph above, the effect of detection should be showing one peak at 122 keV. However, in this study the *CZT* pixellated detector shows another two peaks are Pb Kα and fluorescence.

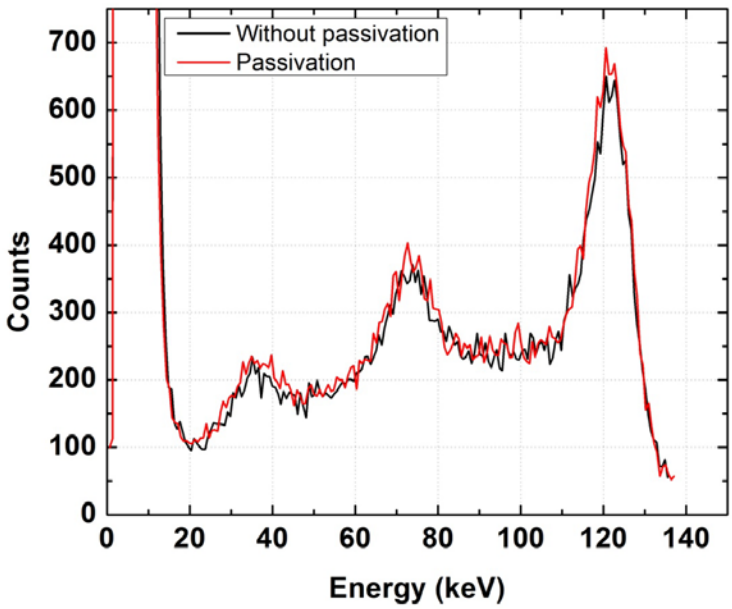

Figure 3.27: *Energy Spectrum of Co-57*

3.6 Summary

Fabrication of *CZT* pixelated structure has been developed as a series of processes designed to produce low surface leakage currents as part of this project. This has been presented and discussed in detail. The surface leakage suppression through the ICP deposition technique with RIE dry etching has produced promising results on these devices. *SiN* passivation + oxygen plasma oxidation reduces the leakage current of *CZT* pixellated detector elements. Moreover, the results indicate that by using this technique the bulk leakage current can be reduced by an order of magnitude compared to the one without passivation. This technique also proves that there is an increase of around 85% in the reduction of interpixel leakage current which gives a better performance of the energy resolving capability. Detectors with this type of passivation have a measured FWHM for ^{57}Co of 10.78 keV - an energy resolution of 8.8%. The output of this work package provide critical feedback to the fabrication effort and ultimately lead to the convergence of an optimised combination of recipes for the contact and *SiN* deposition and etch processes as well as defining a process sequence that leads to optimal performance. All the output of this study has been transferred to Kromek.

Chapter 4

CdTe Timepix Characterisation

4.0 Introduction

This chapter is devoted to a description of the work done and measurements taken with the hybrid single photon counting *CdTe* Timepix detector. Section 4.1 briefly explains the chips architecture, time over threshold (ToT) mode, time of arrival (ToA) mode and readout interface. A comprehensive description of the chip can be found in [55]. Section 4.2 describes the *CdTe* pixellated detector properties as well as the study of its leakage current and material transport properties. Section 4.3 is describes the measurements taken to quantify the imaging performance of this detector. The following section 4.4 explains the Timepix ToT energy calibration procedure and section 4.5 discusses the spectroscopic performance of γ-ray source and x-ray generator measurements. Section 4.6 discusses the results of the spectroscopic performance of the assembly using synchrotron radiation at DLS to characterise the device. Lastly, section 4.7 elaborates the studies that been undertaken to assess the effects on detector performance caused by the presence of defects in the detector material. The results discussed in this chapter allow both imaging and spectroscopic performance capabilities for two detectors with 55 μm and 110 μm pixel pitches to be evaluated.

4.1 Timepix chip properties

The Timepix detector is a semiconductor pixellated X-ray and γ-ray detector which uses a sensor developed of different materials such as Si, GaAs or CdTe. The sensor is bump-bonded to a CMOS read-out chip. The Timepix chip has been developed by the Medipix collaboration [56], [57]. Fig 4.1 shows the Timepix chip board with CdTe sensor assembly.

Figure 4.1: *Timepix chip board with CdTe sensor.*

4.1.1 The structure of the Timepix

The Timepix chip has a array of 256X256 pixels each containing an analog and a digital part. The chip has a power consumption of 440 mW and 450 mW for the analogue and digital sections, for a reference clock frequency of 80 MHz. To facilitate tiling the chip, the pixel array is placed at one side of the chip, leaving three sides which have less than 50 μm inactive space between the pixels and the physical edge of the chip. The digital readout section on the periphery contains wire-bonding pads and the control logic for input and output. It also has contains the circuitry to generate all of the bias/control voltages and currents needed for the operation of the chip. There are 13 global digital to analog converters (DAC), of which eight are 8-bit current DACs, and four are 8-bit voltage DACs. There is a linear voltage DAC which sets the threshold (THL) using 14 bits. This DAC is split in an overall threshold setting of 10-bit, and 4-bit for adjustments of the threshold for each individual pixel. In this way, variations between pixels can be equalised.

Each individual pixel is 55X55 μm^2 in size and contains an analogue and a digital section. Fig.4.2 shows the block diagram of a Timepix pixel cell. The analog part contains a pre-amplifier, discriminator and a 4-bit threshold adjustment. The digital side of the pixel consists of the counting logic, synchronisation logic for the reference clock, overflow control logic, a buffer and a pixel configuration register for setting the acquisition mode and the threshold equalisation. The synchronisation logic has three operation modes (counting, ToA and ToT) which can be set by the configuration bits P0 and P1.

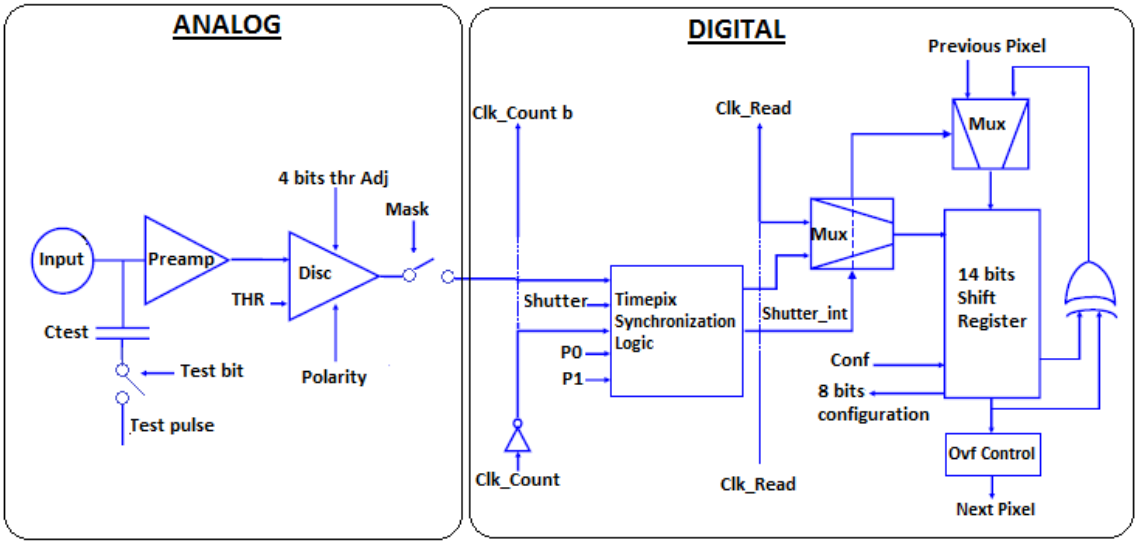

Figure 4.2: *Timepix pixel schematic [55]*

Fig.4.3 shows the Timepix connected to a USB-readout. The overall Timepix assembly consists of three main parts; the sensor layer, Timepix ASIC and readout interface system. The readout is designed to extract the data from the ASIC but is not part of the detector. Several readout systems exist for the Timepix chip. The readout device used for this work is FITPix fast interface for Timepix pixel detector [58]. FITPix interface is developed in the IEAP CTU Prague. FITPix is created to fulfil the need for a faster, smaller, flexible and better interface for the Timepix.

The FITPix interface is based on FPGA circuit which enables to achieve a high data frame-rate [59]. The all digital systems are placed in the FPGA clocked by a 50 MHz

(main system clock). The readout frequency is two times higher than the main system clock [58]. The Timepix chip uses CMOS technology for control and LVDS (low-voltage differential signalling) technology for data transfer. All signals from the chipboard of Timepix are connected through a VHDCI (very high density cable interconnect) connector. The connection between the PC and FITPix is USB 2.0, because the data - rate is 480 Mbit/s [60]. This bus is available in each computer today.

The Pixelman software [61] is the common user interface to control the Timepix chip, and to store data from the pixel matrix. It provides a preview window, and writes the data to a Binary file. In addition, all the DAC settings, like threshold and bias voltage, can be controlled through the Pixelman software. The software also provides the possibility to perform a threshold equalisation of the chip, so that the threshold is uniform over the entire pixel matrix.

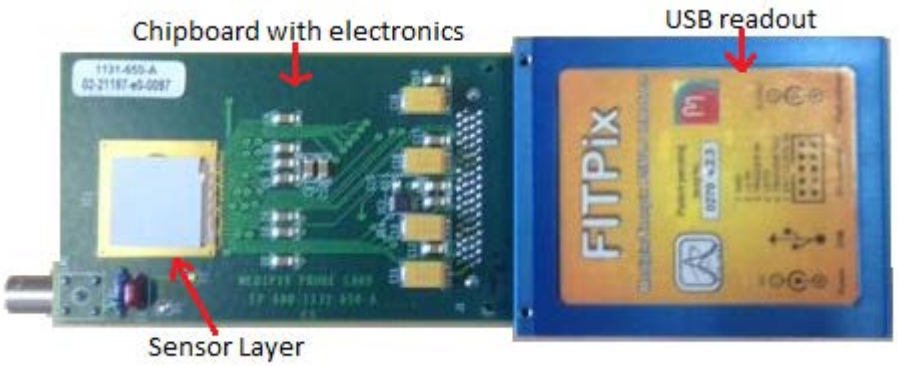

Figure 4.3: *The Timepix detector with a USB-readout*

The sensor layer is the part of the detector where the study of the detector characterisation takes place. Fig. 4.4 shows the structure of a Timepix detector assembly. The material which the sensor layer is made of is a semiconductor. In these studies a Timepix readout chips with CdTe sensors were used. The size of the sensor material is usually about 1.4 cm X 1.4 cm and it is 0.3 mm - 2 mm thick. In this project applied 1 mm thick CdTe. The sensor material is the screen for the detector. Particles which pass through the sensor material are scattered and deposit some of their energy within the sensor layer.

By extracting this energy from the sensor, one can detect the particle tracks and make them"visible".

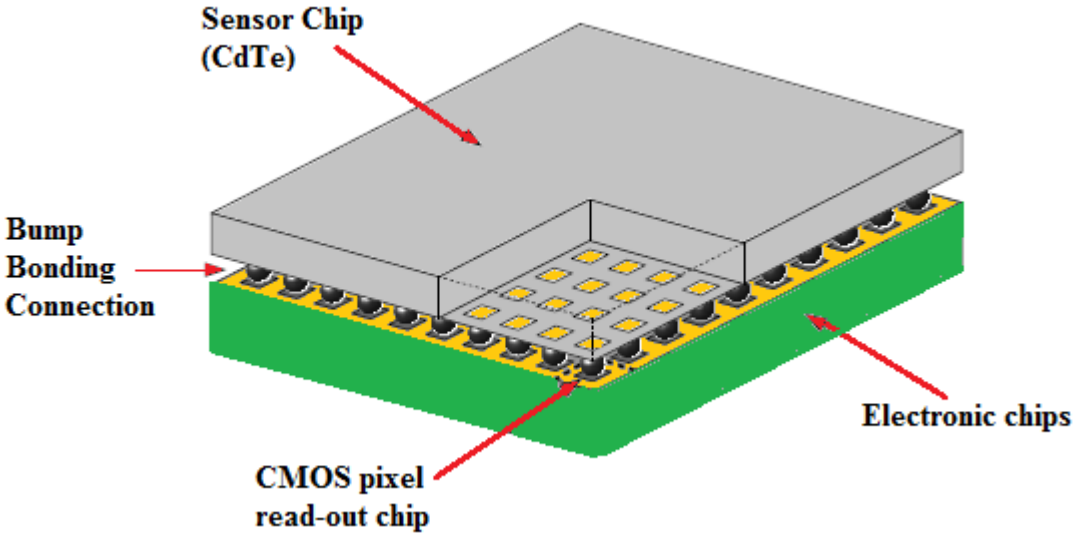

***Figure 4.4**: Diagram of Timepix detector*

The ASIC has two main purposes: it is needed to extract the deposited energy information from the sensor and, together with the electrodes on the sensor backside, it provides the pixelation of the sensor layer. The pixel grid on the ASIC is connected to the sensor layer by bump-bonds (Fig.4.4). The distance between centres of the electrodes defines the size of the pixels, known as the pixel pitch. If every pixel on the grid is connected to the sensor layer the pixel pitch is 55 µm, but chips with 110 µm and 220 µm pixel pitch are available as well. In the latter cases only every second or fourth ASIC grid pixel is connected to the sensor. The number of pixels is 256 x 256, 128 x 128 or 64 x 64, respectively.

The chipboard with the electronics is responsible for the ASIC power supply, supply voltage generation and the data connection from and to the ASIC. A comprehensive descriptions of electronic chips function are discussed in [55], [62]. In the integrator the analogue signal, which is related to the energy deposited in the sensor, is transformed into a digital data packet. This procedure is discussed in the next subsection. The other part is the digital analog converter (DAC). It converts the working parameters of the detector,

which can be set and adjusted by the user, from its digital values coming from the computer to analogue values which the electronics can deal with. Therefore the working parameters of the ASIC are named DAC-values, or rather, DAC-settings.

4.1.2 Timepix Detection Process

Fig. 4.5 shows the charge collection in Timepix detector in various operation modes.

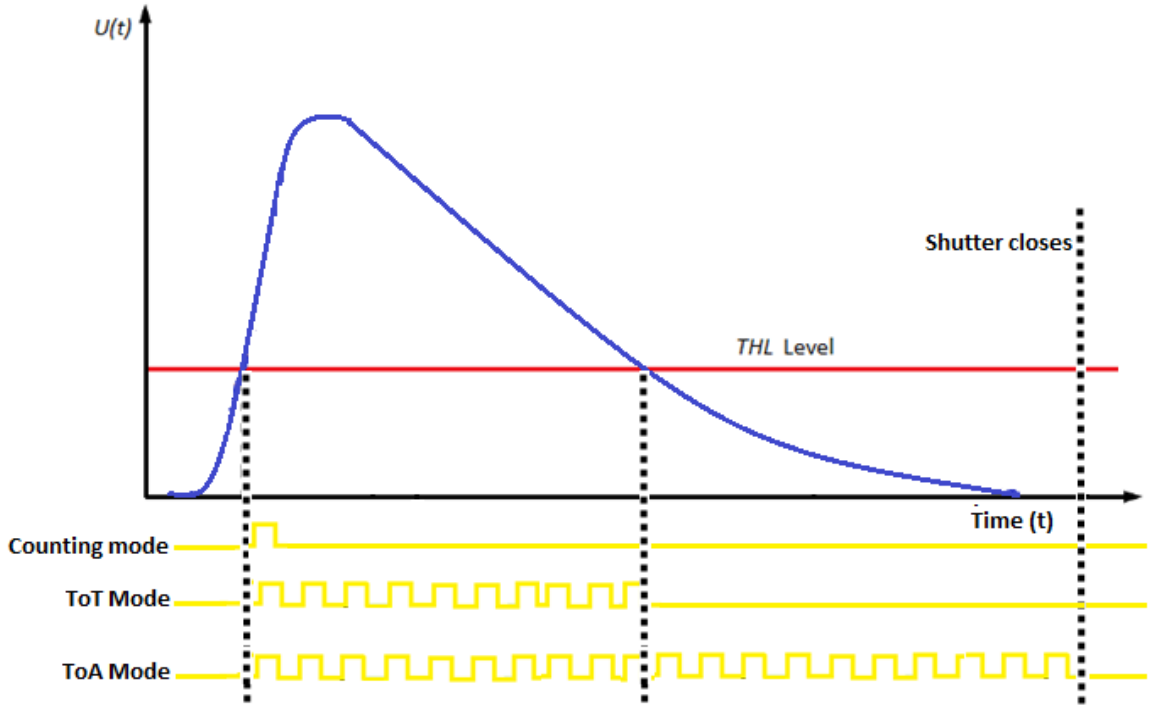

Figure 4.5: *Charge collection in Timepix*

The height of the pulse is proportional to the amount of charge collected in the pixel. The red line indicates the threshold level (THL), which is a DAC-value applied to set a discrimination level of the pixel signal. The threshold is necessary as there is always a leakage current in the detector due to the noise in the electronics – this is undesirable and is suppressed by using the threshold. This signal (blue line) can then produce several different digital outputs when it exceeds the threshold level. Every pixel on the Timepix chip can be configured in one of three operating modes. These are the Time over Threshold

(ToT), Time of Arrival (ToA) and Medipix or counting mode. The characterisation of CdTe Timepix detector in this study predominantly uses the Counting and ToT modes.

- In counting mode, the detector counts how many times during the measurement period, called the acquisition time, that the pulse height was higher than the THL. This number is recorded for each pixel and directed to the detector output.

- The time-of-arrival (ToA) mode; in this mode the detector counts the time (in digital units supplied from an on chip oscillator) from the first time the pulse is above the threshold level until the end of the acquisition time.

- The time-over-threshold (ToT) mode; in this mode the length of the pulse above the THL is measured to provide information about the energy deposited in a pixel. The discriminator digital to analogue converter determines whether a signal is over threshold or not. The threshold (THL) DAC determines the height of the threshold, and therefore the width of the pulse. A typical threshold is about 50 DAC (≈ 1250e) above the noise mean. The ToT range is within 14 bits precisely 11810 counts. The resolution of the ToT measurement is determined by the frequency of the counting clock, which can be up to 100 MHz. The shape of the pulse is highly influenced by the settings of the digital to analogue converters [63]. The Ikrum (Krummenacher current) DAC determines the slope of the falling edge of the signal pulse. A high Ikrum current decreases the length of the falling edge, because it enables a faster discharge of the integrating capacitor of the charge amplifier. A higher Ikrum current decreases the pulse width for a given input signal. Furthermore, it decreases the pulse height a little. The preamplifier current influences the rise time of the pulse. A small preamplifier current decreases the rise time, which can vary from 90 to 180 ns.

4.1.3 Threshold equalization

Before a Timepix detector can be used properly, an analogue threshold equalization has to be performed. This is necessary because all the pixels are not really identical, but have slight differences in their electrical properties due to fabrication. Therefore, every pixel has a different noise level. If only one fixed THL value is used for all pixels, the actual threshold energy will vary among all pixels leading to increased noise. Therefore the threshold energy has to be adjusted for each pixel individually. For every pixel there is a global threshold level supplied to all the pixels. On each pixel there are 3 bits of threshold adjust so that the local threshold level can be shifted up or down within a small interval around the threshold energy given by the THL. After this is done for every pixel the threshold energy is at the almost same level for all pixels.

The adjustment is known as threshold equalization and can be performed automatically by the PixelMan Software [61]. The threshold equalization window of PixelMan is shown in Fig.4.6. Several parameters can be set which have an influence on the quality and the duration of the process:

- Spacing: If all pixels are equalized at the same time, they can affect each other and degrade the quality of the equalization. To avoid this problem the equalization can be done for a set of pixels which have at least a particular separation which can be set by the spacing parameter. If, for instance, the spacing is set to 2, only one pixel and its second neighbours will be equalized at the same time (then the next set of neighbours and so on); for spacing 3 the third next neighbour etc. Of course, the time which is required for the equalization process increases with spacing.

- Interpolate: If this parameter is set, the software will interpolate between various measurement points. For the best equalization the interpolation should be turned off.

- Acquisition count and time: The time and number of repetitions for one particular measurement run.

- THL Range automatic: If this is set true, the software will adjust the THL automatically to an optimal level in the given range. This process increases the time for the equalization (depending on the step and the range).

After the procedure, the resulting settings for the pixel grid are called an adjustment mask. Masks can be saved and loaded when they are needed for a measurement process. A mask can be considered as good, or rather, useful to work with if the distance between the actual distance σ and the, so-called, optimal distance σ_{opt} is not bigger than

$$\Delta\sigma = \sigma - \sigma_{opt} < 0.1.$$

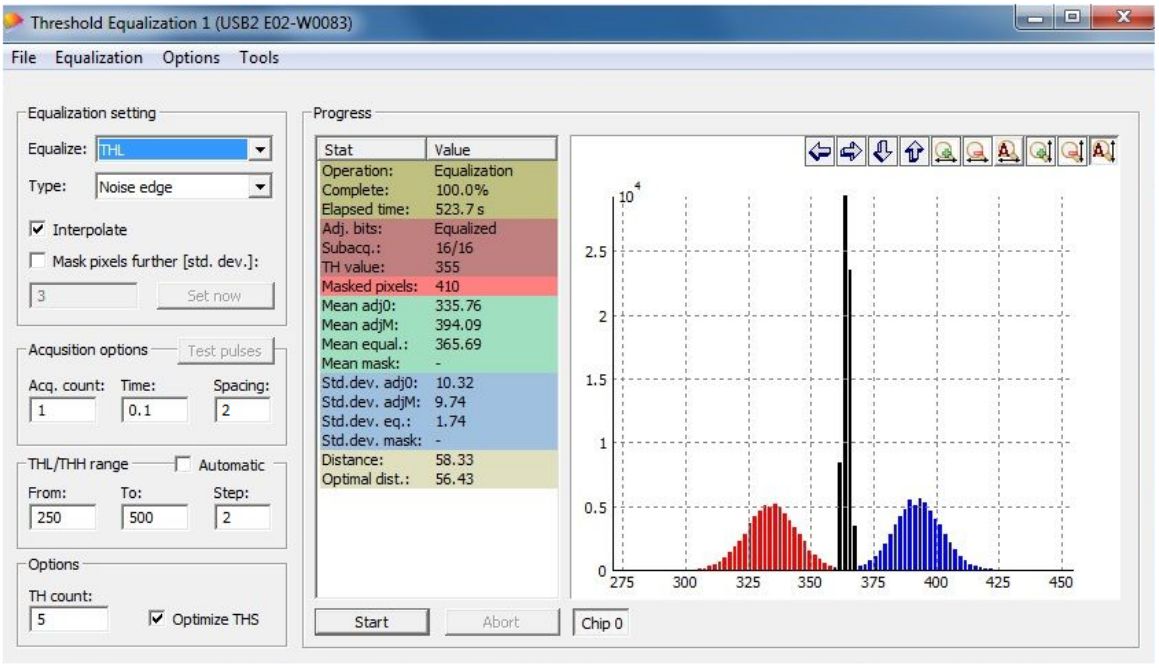

Figure 4.6: *Threshold equalization of the chip*

4.2 CdTe properties

4.2.1 I-V measurement

The sensor bump-bonded to the Timepix chip is a 1 mm thick high resistivity p-type CdTe material from Acrorad [64]. The absorption efficiency of a 1 mm thick CdTe sensor layer

approaches 100% for photons of energies up to 60 keV, and is 65% at 100 keV [65]. The dice size is 14 x 14 mm matching the size of the readout chip. The pixels and the back side of the detector are Ohmic type Platinum contacts. The current-voltage characteristic of the detector already bump-bonded to Timepix is shown in Fig 4.7. I-V measurement shows a symmetric curve where it establishes quasi-Ohmic behaviour for bias voltages between ±300V (Fig.4.8).

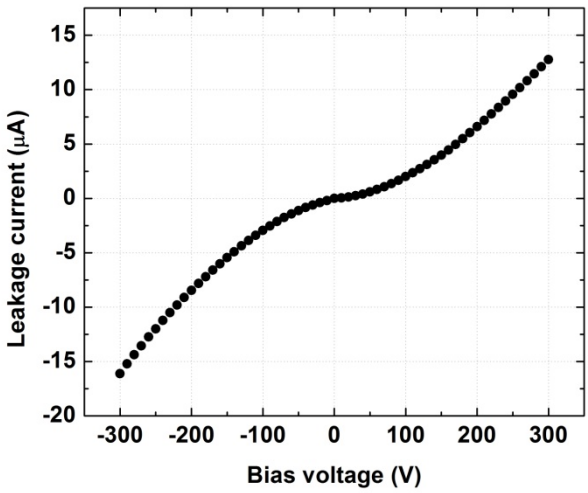

Figure 4.7: *Leakage current for CdTe Timepix detectors*

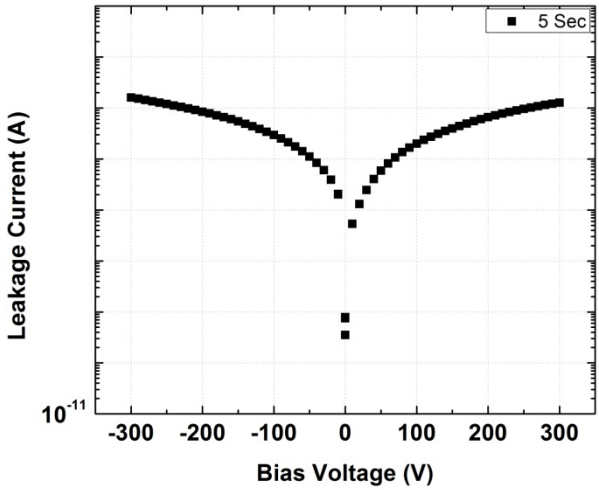

Figure 4.8: *Symmetric curve of ohmic behaviour CdTe Timepix detector*

The measurement of leakage current as a function of applied bias, in both electron (reverse) and holes (forward) collection mode shown in Fig. 4.9. The typical leakage

current was measured with a delay time in order to minimise measurement of the relaxation current, which is commonly known to overlap with the leakage current. In forward bias at 300 V a leakage current of around 8.28 x 10^{-6} A is measured at 30 sec (interval delay time for each measurement) and at 5 sec it is around 1.20 x 10^{-5} A. It shows that the leakage current for CdTe Timepix reduce 25% when the delay time is 30 sec. For negative bias at -300 V shows a reduction of about 45% in the leakage current at 30 sec delay time compared to a 5 sec delay.

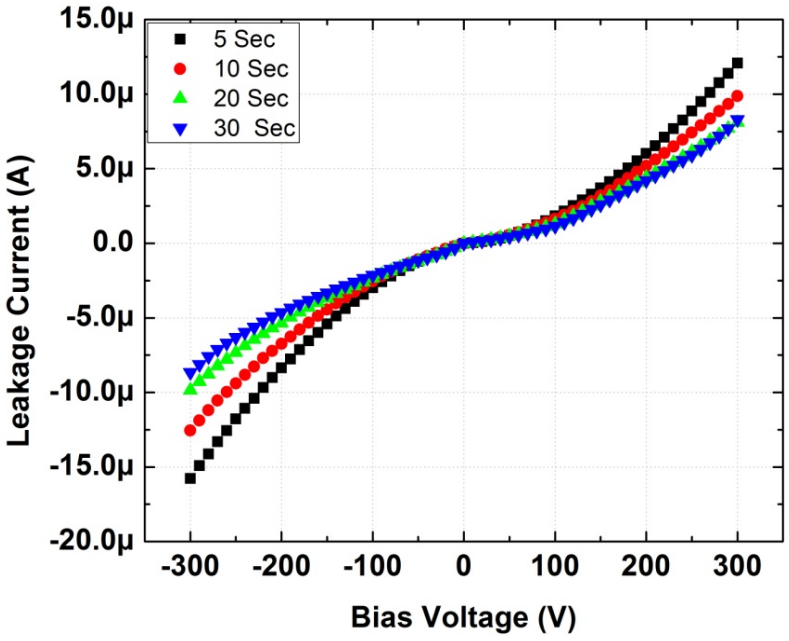

Figure 4.9: *Different delay times*

Leakage current also has a time-dependent component. Large over/under shoots are measured when bias is increased/decreased, respectively. The measurements were set up where the bias voltage was swept from 0 to 300 V in steps of 10 V then back from 300 to 0 V and then to -300 and back to 0 V. The result in Fig.4.10 shows that a return to a steady value at an exponential rate is observed, and an almost stable leakage current value can be measured after a few minutes. Slow drifting of the leakage current values can also be measured over a day. These leakage current fluctuations were found not to have much influence on the X -ray detection abilities of the devices.

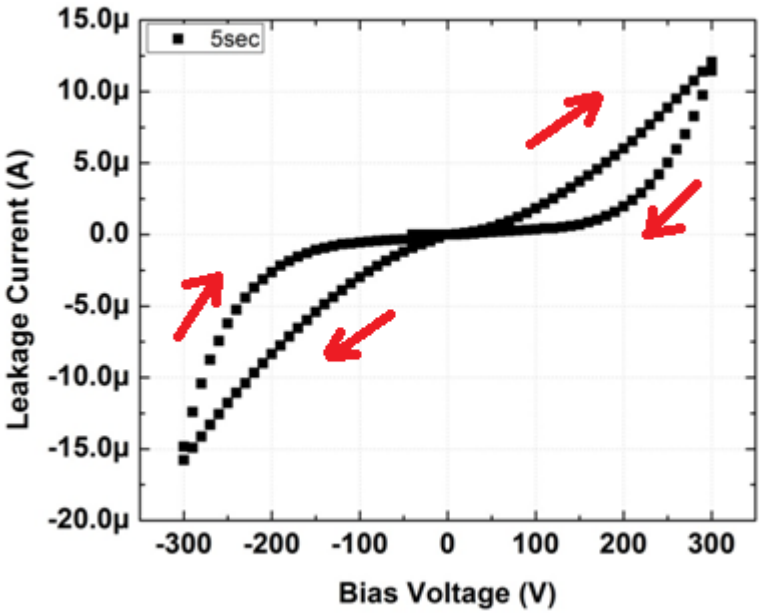

Figure 4.10: *Different magnitude of bias voltage*

A critical issue for CdTe detectors is their time instability under bias, i.e. the so-called polarization effect [63]. The term polarization has come to mean any change in the performance of the detectors after the detector biasing. This effect is mainly due to the trapping and the de-trapping of the carriers that alter the space-charge distribution and the electric field profile in the detectors. Polarization leads to a time-dependent decrease in counting rate and charge collection efficiency Fig. 4.11 shows the current–time characteristics for relaxation current at different voltages with negative voltage applied to the Timepix detector. The relaxation currents measured at low field ~ -10 V indicates the contribution of pure dielectric relaxation current. In higher fields ~ -100 V and above, the current has contributions from both dielectric relaxation current and leakage current. From the graph, the polarization effect stabilised at above 230 seconds for all the reverse bias.

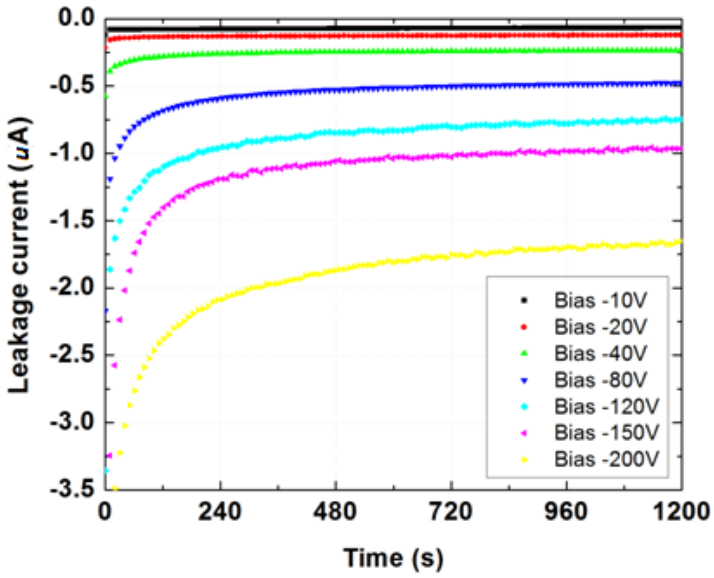

Figure 4.11: *Bias stability measurement*

4.2.2 Charge Carrier Transport Properties

The Mobility lifetime product

The transport properties of the charge carriers in the CdTe sensor, namely the mobility-lifetime product ($\mu\tau$-product), is a major indicator of the charge collection efficiency (CCE) of the detectors [66]. μ is the charge mobility and τ is the mean lifetime of the charge carrier. Mobility lifetime product is one of the key measurable parameters for determining the quality and charge transport properties of CdTe sensors.

The $\mu\tau$-product was investigated by using a set-up that measured the response to 5.5 MeV alpha-particles at bias voltages ranging from 0 to 50 V for electrons and 0 to 250 V for holes. The alpha particles are absorbed in up to the first 30 microns of the sensor and the charge carriers have to drift almost through the complete depth of the sensor to reach the pixel contacts. The average charge deposited was plotted against its corresponding bias voltage. The data points were fitted to the Hecht Relation and the corresponding $\mu\tau$ -product can be extracted for each pixel [67]. The Hecht-relationship is shown in equation (4.1) .

$$Q(U) = Q_o.\frac{\mu.\tau}{d^2}.(U - U_o).\left(1 - e^{\left(-\frac{d^2}{\mu.\tau(U-U_o)}\right)}\right) \quad (4.1)$$

Here, *Q* refers to the pulse height, which is correlated with the induced charge. μ is the mobility and τ is the lifetime of the charge carriers. *U* is the bias voltage on the sensor and *d* is the sensors thickness. The fitting parameter U_0 takes into account the effect of the energy threshold [67]. At a sufficiently high bias voltage the exponential component tends to zero. This corresponds to the detector being over depleted, and, at sufficiently high bias, charge is no longer trapped and the slope of the μτ plot flattens. This region of operation is called the saturation region [68],[69].

After absorption of the alpha particles, the generated charge cloud will expand while drifting towards the collecting electrode. As the CdTe-Timepix assembly is a pixelated readout system, the charge carriers will influence charge in a circular shaped cluster expanding over several pixels. Therefore the method described before had to be adapted, which was achieved by using the Time over-Threshold (ToT) readout mode of the Timepix chip. This readout mode is measuring the time, which the signal of the charge sensitive amplifier (CSA) is above the energy threshold. The ToT is measured by counting the number of period lengths given by an internal frequency, being further referred to as ToT counts. In the case of the Timepix pixel electronics the pulse length is directly correlated to the pulse height, thus providing a measure for the pulse height in each pixel. The overall charge created by an alpha particle will create pulse heights in several pixels which when summed up corresponds to the pulse height as would be induced in a non pixellated readout system. Thus, a reconstruction of the overall pulse height is possible by summing the pulse heights in each pixel of the cluster. Cluster charge is reconstruct using image J where it's function of bias voltage applied.

The extracted mean $\mu\tau$ value for electrons from fitting the data with the Hecht relation in Fig. 4.12 was found to be (1.35 ± 0.04) x 10^{-3} cm^2/V and agreed with the previously published value (1.9±0.6) x 10^{-3} cm^2/V) [67]. The extracted $\mu\tau$ value for holes

in Fig. 4.13 was measured to be (2.1 ± 0.3) x 10^{-4} cm^2/V which is more than twice a previously published values (0.75±0.25) x 10^{-4} cm^2/V [67]. Both values are within the typical range of Acrorad CdTe material.

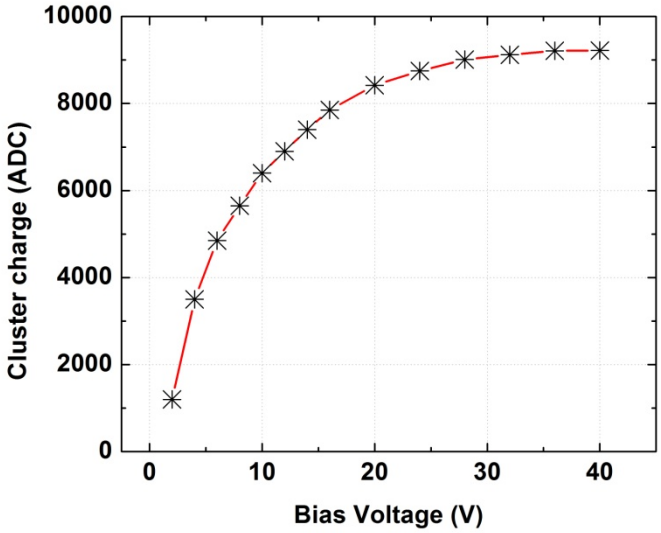

Figure 4.12: *Mean μτ for electrons*

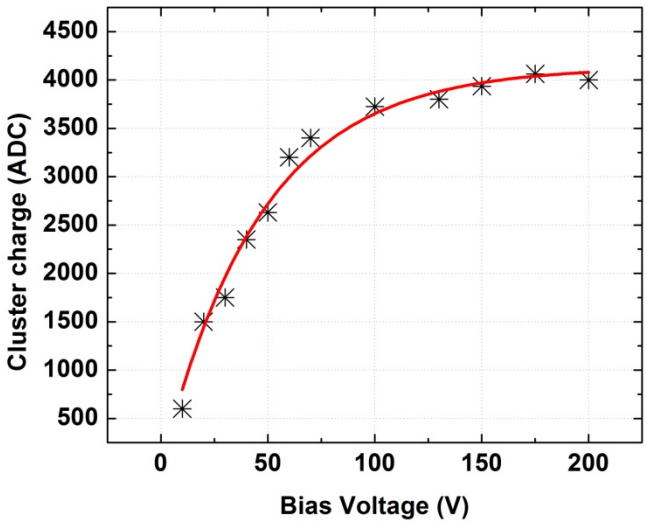

Figure 4.13: *Mean μτ for holes*

4.3 Imaging performance (MTF)

For the Modulation Transfer Function (MTF) measurements the bremsstrahlung spectrum from a dental X-ray tube operated at 60 kVp was used. No flat field correction of the acquired images was performed. This approach was chosen in order to establish the basic performance of the system without any corrections.

4.3.1 Theory

The MTF characterises the spatial frequency response of an imaging system and basically describes how well the object contrast is transmitted through the imaging chain for a given spatial frequency.

It is defined as the ratio between the modulation of a sinusoidal test pattern M_{in} at a spatial frequency f and the modulation of the obtained image, M_{out}

$$MTF(f) = \frac{M_{out}(f)}{M_{in}(f)} \tag{4.2}$$

It yields a value between zero and 1 for all frequencies and can be described by analytical functions or a convolution of functions in simple cases. Assuming for example square pixels with lateral dimension *l* and a uniform sensitivity over the whole pixel area, the theoretical limit for the MTF is given by

$$MTF_{sq} = \frac{\sin(\pi f l)}{\pi f l} =: sinc(\pi f l) \tag{4.3}$$

where f denotes the spatial frequency. There are two methods for measuring the MTF of a given system: the edge method and the slit method.

The edge method is a relatively fast and easy method to derive the MTF of a digital imaging system from a single, even a rather small, image. This is especially convenient when working with small detectors and at an early development stage. For this method a precision edge made from e.g. tungsten is placed approximately 1.5^{o} tilted to the pixel rows over the detector and an image is acquired. By projecting the image data along the direction of the edge, a one-dimensional over sampled data set is obtained from which the edge spread function is determined and numerically differentiated, leading to the line spread function (LSF) perpendicular to the edge. Calculating the modulus of the Fourier transform of the LSF results in the desired MTF, which is also perpendicular to the edge.

The slit method uses a fine slit instead of the edge employed when using the edge method (Fig. 4.14). The advantage of the slit method when compared to the edge method is that the projection of the image data along the slit axis leads directly to the LSF without the need to calculate the derivative of the edge spread functions. But it has also disadvantages: the fabrication of a fine, accurate slit is more difficult than that of a simple edge and the lowest frequency components are not readily available in the image because only a very narrow strip of the detector is illuminated. To evaluate the measurement the low frequency components of the LSF must be extrapolated. Last but not least the positioning of the slit can be rather more difficult because only a nearly perfect alignment produces a satisfactory slit image; the side walls of the slit must be oriented exactly perpendicular to the detector plane for the slit to be seen at all. On the other hand it is not easy to achieve a very good alignment when using a single edge since the edge image does not show misalignments so clearly.

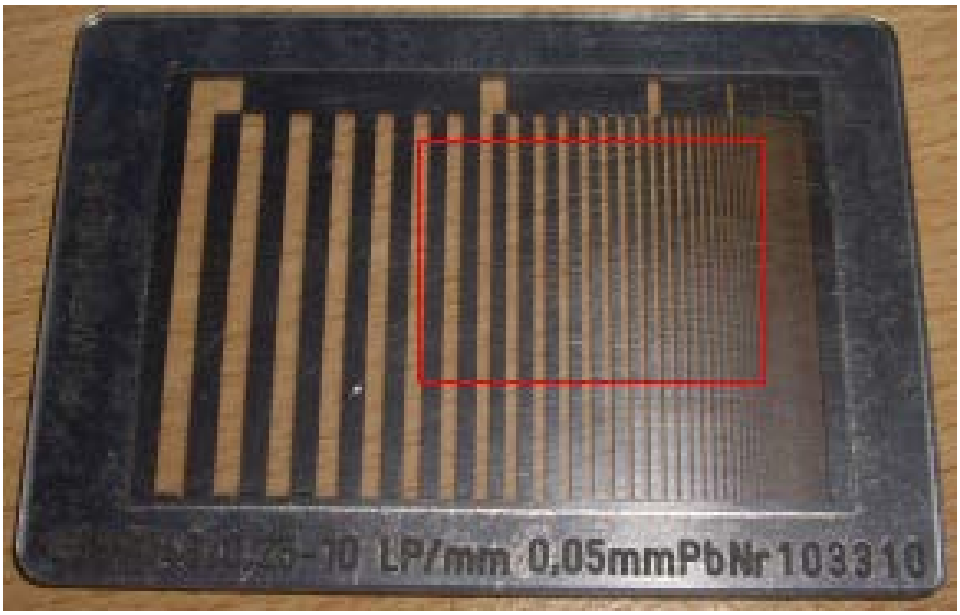

Figure 4.14: *PbNr slit*

4.3.2 Experimental setup

The imaging capabilities of two pixel detectors with different pitches were evaluated in terms of the modulation transfer function (MTF) with a laboratory X-ray tube. This represents the normalised transfer of contrast through the system at a given spatial frequency, expressed in line pairs per millimetre (*lp/mm*). A slanted niobium-lead (*PbNr*) edge was placed close to the detector surface at ~ 5 degrees inclination to a sensor row. The detector was exposed to various energies from the X-ray tube. No flat-field correction was performed on the images. An error function was fitted to the edge profile. The Fourier transformation of the derivative normalised to 1 at 0 spatial frequency resulted in a plot of the MTF. Fig 4.15 shows the experimental setup used to make these measurements.

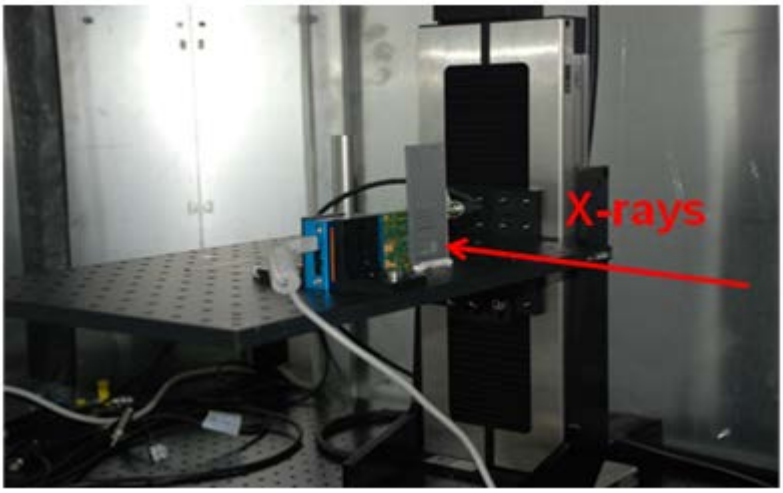

Figure 4.15 :*X-ray tube experimental setup for MTF*

4.3.3 Results

A comparison between MTFs at various bias voltages for the 55 µm pitch detector is presented in Fig.4.16. Fig 4.17 (a) and (b) shows the variation of image quality, corresponding to two bias voltages of -100 and -500 V. The best MTF is observed for bias voltages of 400–500 V. Gradual degradation of performance is seen for smaller detector biases. It should be noted that due to non-uniformities and defects in the detector material a variation of 10 – 20% in the MTF taken from various "good" regions on the detector was observed.

The MTF performance was assessed at various X-ray tube cathode voltages. A degradation of ~10% was observed for X-ray tube energies between 20 and 60 kVp, which is mainly associated with the *PbNr* being more transparent at higher energies, leading to a degradation of the edge quality. This can be seen in Fig. 4.18.

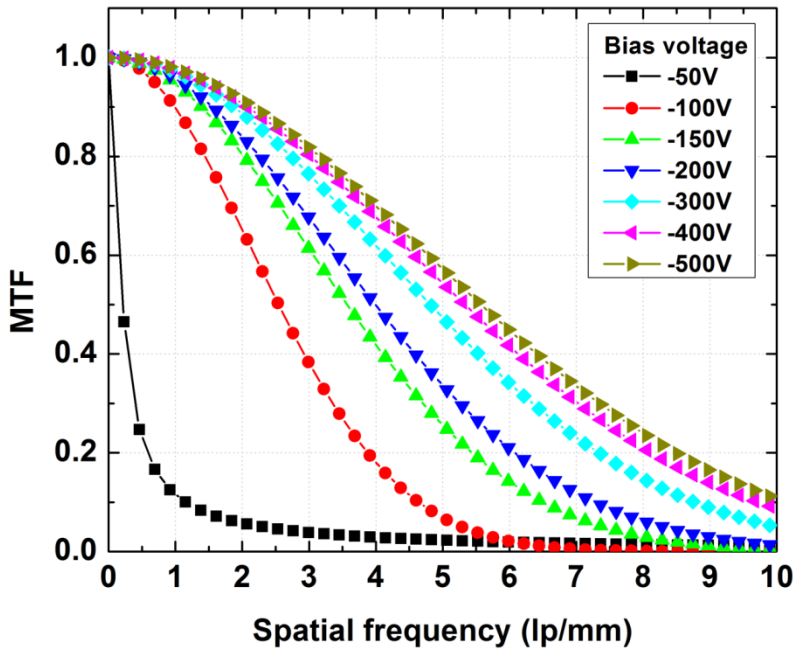

***Figure 4.16**: MTF dependence of bias voltage recorded by the 55µm pixel pitch sensor. X-ray tube energy was set to 60 kVp.*

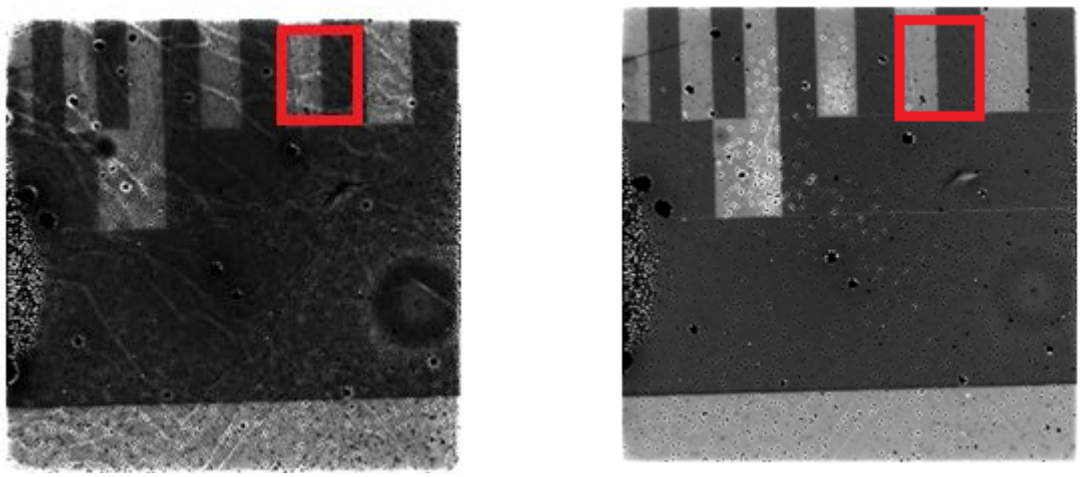

(a) *(b)*

***Figure 4.17:** Images to the right demonstrate the quality of the image recorded: (a) at -100V and (b) -500V. Red square shows the area analysis of MTF.*

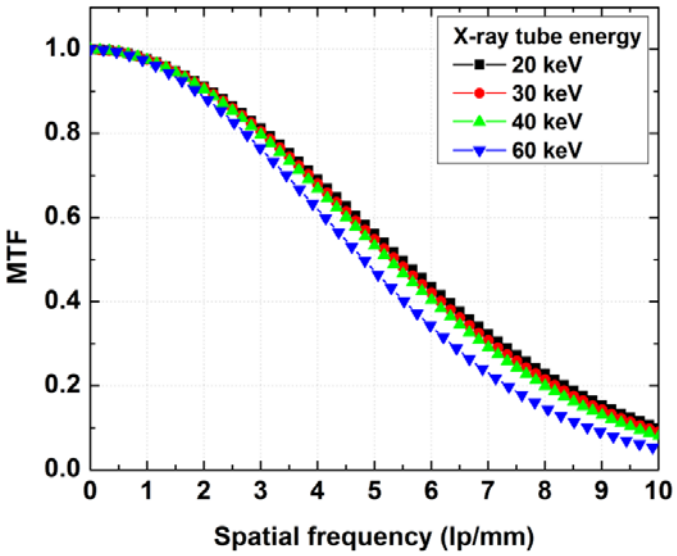

Figure 4.18: *55 µm pixel detector MTF dependence on X-ray tube voltage. The detector was biased at -300 V, threshold was set to ~ 5 keV*

An MTF comparison between 55 and 110 µm is shown Fig.4.19. The X-ray tube was operated at 20 kV, while the detector threshold was set to a noise level of ~5 k V. The system has been calibrated follow the procedure in 4.4. A 70% modulation transfer at 4 *lp*/mm is observed for the 55 µm pixel compared to 30% for 110 µm. This is in agreement with expected values of the pixel being double the size.

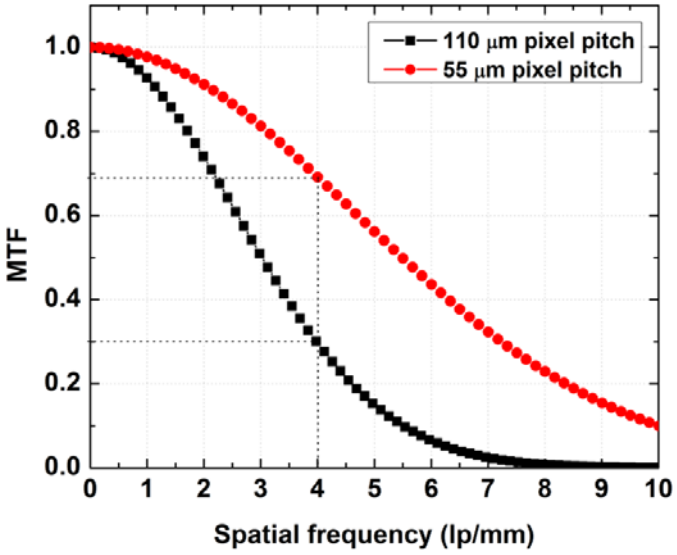

Figure 4.19: *MTF comparison between 55 µm and 110 µm pixel detectors. Bias voltage applied was -300 V, threshold was set to ~ 5 keV.*

4.4 Timepix ToT energy calibration

Since the ToT is a digital representation of the pulse height and not directly measured, there is a need to provide a method of calculating the deposited energy in keV from the ToT which is actually measured. This work is to establish the measured dependence between the TOT and the deposited energy E - E(ToT). It can be done for each pixel individually or for the whole matrix. Here it was done for the whole matrix. The ToT calibration procedure consists of the following steps:

- Recording the ToT spectra of well-known -radiation sources.
- Identifying the peaks in the ToT spectrum and relating them to the photon energies emitted by the radiation source.
- Fitting the peaks and inserting them into a ToT versus energy diagram.
- Fitting a calibration curve ToT(E) through these points and inverting the curve to get the E(TOT) relation.

The first step in the calibration process is to record the ToT spectra of well-known radiation sources and identify their γ-lines in the recorded ToT spectra [70]. Two kinds of radiation were applied:

- γ-lines arising from the radioactive decays of materials which undergo spontaneous decays with a preferably high branching ratio. A high branching ratio is desirable to have monochromatic radiation in a particular energy interval.
- X-ray fluorescences; K_{α}- and L_{α}- fluorescence lines of particular materials. This experimental setup is more complex since to excite those transitions, electrons of the K or L shell have to be ejected from the atom. An external X-ray source is used

to ionise the transitions needed. The energy of the photons emitted by the source have to be higher than the ionization energy of the K shell and it is convenient to be able to regulate the source's photons' energy and intensity. Additionally a stable photon flux over a time period is needed. Commercial continuous wave X-ray tubes can fulfil these requirements.

A cluster analysis procedure is used to increase the spectrum quality from the measurement. The idea of clustering is to increase the spectrum quality by avoiding the effects due to charge sharing.

There are several possible scenarios when a photo electron is generated in the detector. In Fig. 4.20 (a), the photon converts close to the centre of the pixel. The small arrows denote the drifting charges, and the blue block gives an indication of the charge deposited in the pixel. In this case, all charges are collected in one pixel, and the position is always reconstructed exactly in the pixel centre. In the second case shown in Fig. 4.20 (b), the photoelectron passes close to the edge of the pixel. Because of the diffusion of the charges when drifting towards the readout chip, a small amount of charge will be deposited in the neighbouring pixel. The third case in Fig.4.20 (c) shows a photon which scatters in the detector, so that multiple pixels register a charge due to the interaction. Thus, in Fig. 4.21 (Synchrotron-ray beam line) and 4.22 (X-ray source) shows some of the results of cluster analysis applied to the spectrum measurement using the *CdTe* Timpex in ToT mode. This result shows by applied the cluster analysis, it's improved the analysis to plot the energy spectrum.

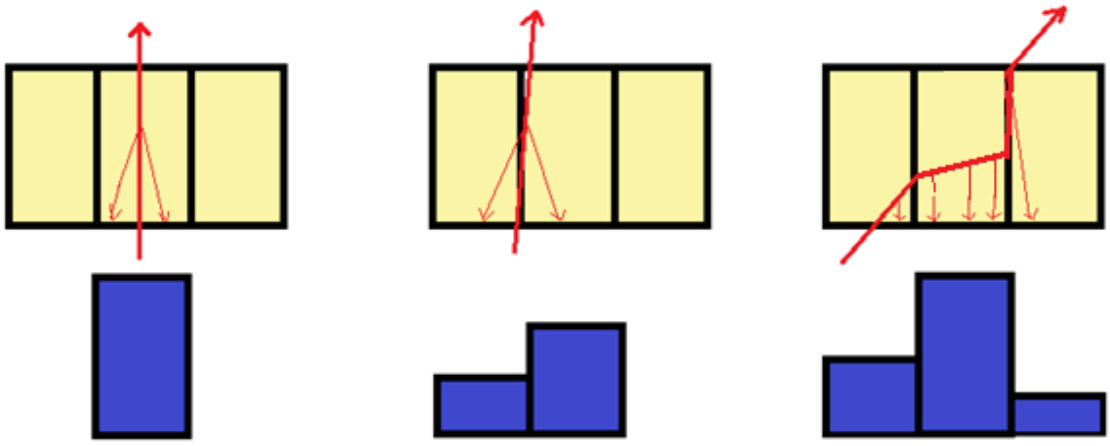

(a) (b) (c)

Figure 4.20: *A photon beam through a pixel detector; (a) single hit (b) diffusion (c) angled incidence*

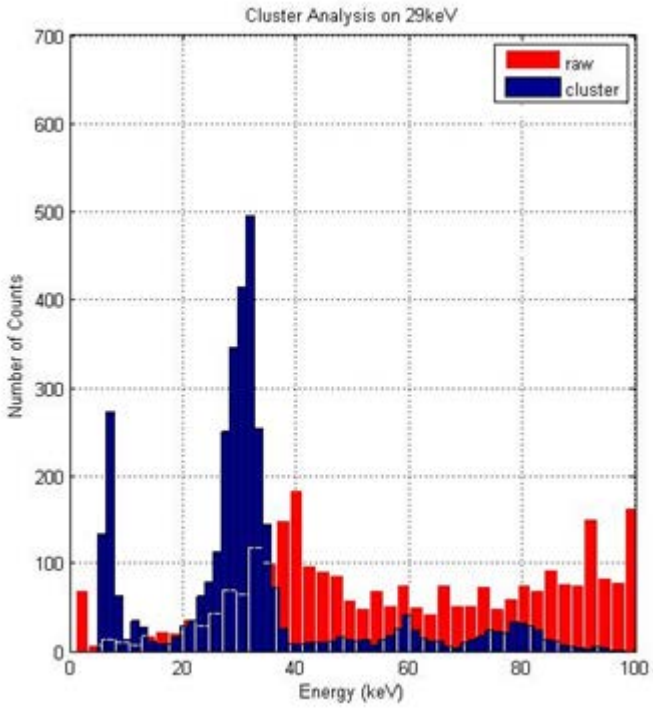

(a)

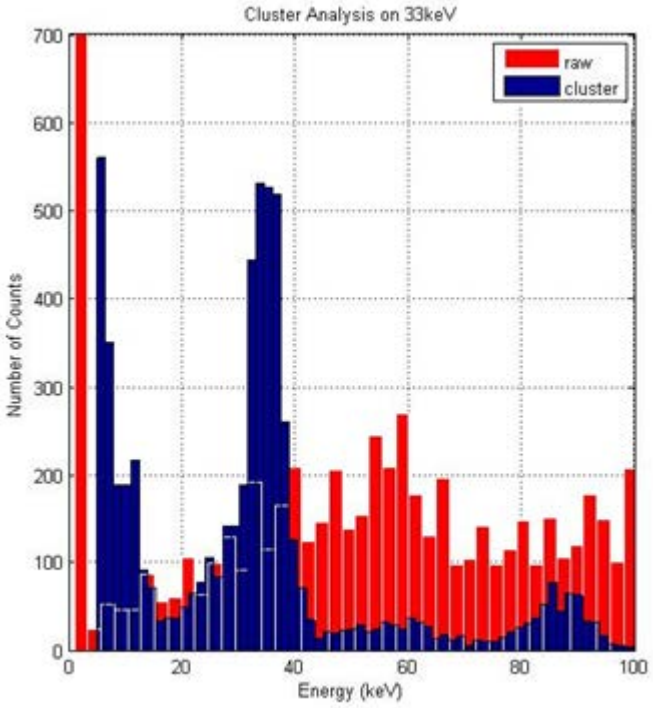

(b)

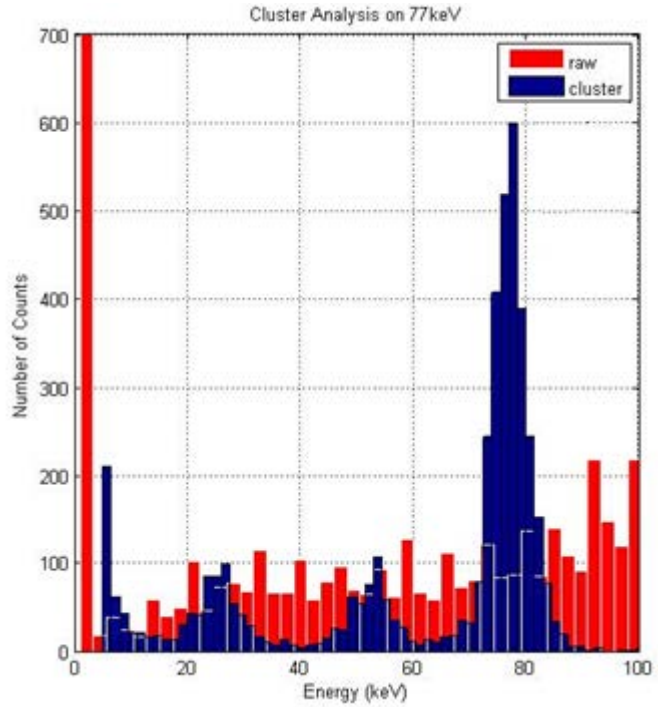

(c)

Figure 4.21: *Cluster analysis: (a) 29 keV, (b) 33 keV and (c) 77keV*

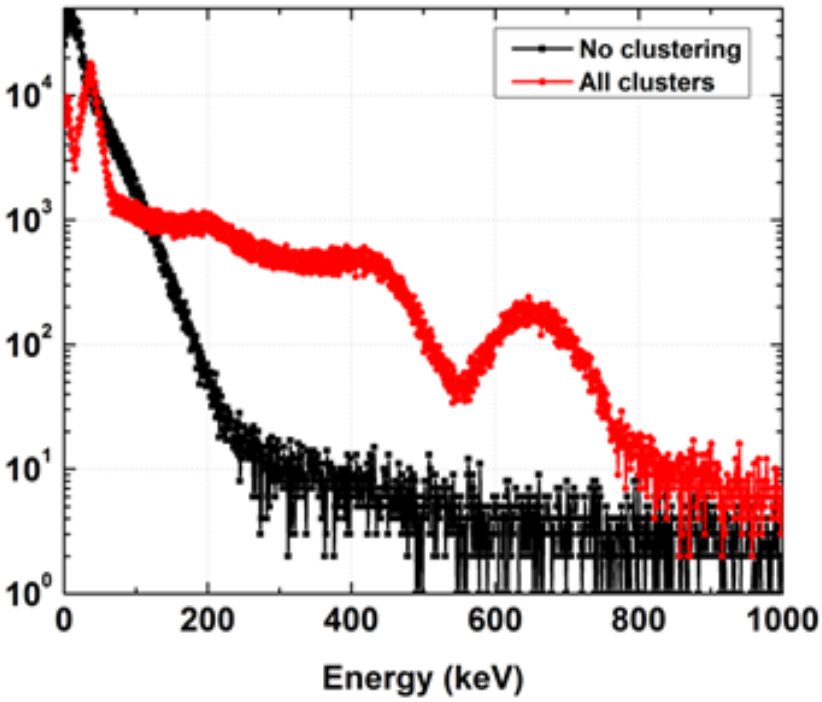

Figure 4.22: *Clusters analysis of* ^{137}Cs

Cluster analysis was applied for energy calibration [70]. The calibration curve is a measure of the relation between the ToT and the real energy measured in a pixel taking into account the cluster information. The procedure is to insert the results of the identified peaks from all measured ToT spectra in a ToT versus energy graph and fit a curve to these points. For single pixels, interactions of low energy X-ray sources (below 60 keV) were recorded and fitted with a nonlinear function:

$$ToT = a \times E + b - \frac{c}{t-E} \tag{4.4}$$

The coefficients *a*, *b*, *c* and *t* were extracted and the quadratic equation was resolved against energy. The positive root of the solution was used for ToT to keV data conversion. Tabel 4.0 shows the data conversion from ToT to keV. Meanwhile, Fig. 4.23 shows the ToT energy calibration 55 µm *CdTe* Timepix detector created from these studies. For γ-sources with energies above ~100 keV only the linear part of the equation was employed. The recorded energy a spectrum was reconstructed by summing the charge converted into

keV units in the neighbouring pixels, which passed the threshold. Fig.4.24 presents the plot of energy calibration with energy above ~100 keV.

***Table 4.0**: ToT Calibration table for 55 µm CdTe Timepix detector*

Element (Kα)	Energy (keV)	ToT counts	Error on ToT
Ti	4.5	7	
Mn	5.9	10	
Ni	7.5	30.2	11.0
Cu	8.0	33.0	11.7
Au (Lα)	9.7	39.3	13.1
Rb	13.4	57.8	12.36
Zr	15.8	60.1	10.7
Mo	17.5	67.2	10.2
Ag	22.1	80.7	10.7
In	24.2	85.9	10.6
Sn	25.3	89.9	9.99
Ba	32.0	99.0	14.07
Tb	44.2	131.1	15.66
Am-241	59.9	185.8	15.64

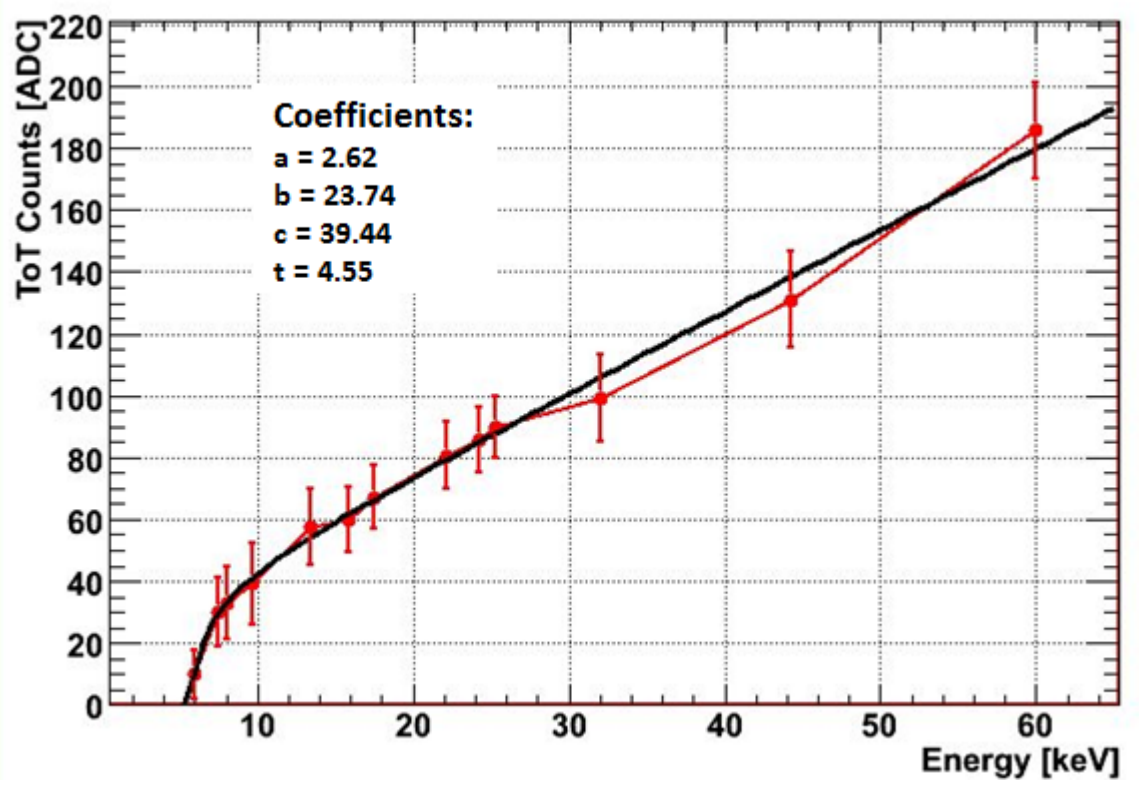

***Figure 4.23:** CdTe timepix ToT energy calibration*

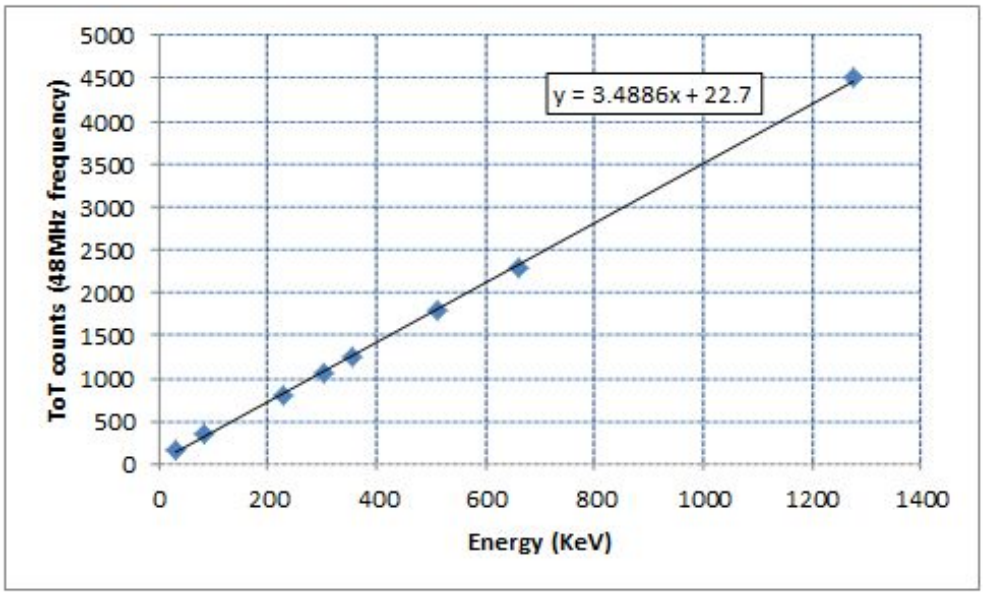

Figure 4.24: *55 µm CdTe Energy calibration with energy above ~100keV*

4.5 Spectroscopic performance

Spectroscopic performances of the *CdTe* Timepix detector have been characterised by using the gamma – ray source, target fluorescence from an x-ray tube and monochromatic beams from synchrotron radiation. This section discusses the experimental work conducted using gamma-ray/ X-ray sources and target fluorescence from x-ray tubes only.

γ-ray Source

In these studies ^{137}Cs and ^{22}Na γ-ray sources were used. The objective was to measure the energy resolution and pixel cluster sizes seen by CdTe Timepix detectors with different pixel pitches. Fig. 4.25 (a) and (b) compare the spectra of ^{137}Cs for both pixel pitch detectors. For the 55µm pixel the energy resolution of the 662 keV peak is found to be 8.4% compared to 5.7% for the 110 µm pixel. Fig. 4.25 (c) and (d) show maps of energy spectra dependence on average cluster size. It should be noted that the average cluster size

of the 55 µm pixel detector is 800 µm, which is 200 µm bigger than that of the 110 µm pixel. In addition Fig 4.26 (a) and (b) shows the comparison of the spectral performance for ^{22}Na (511 keV) for both pixel sizes. The energy resolution for 55 µm pixel pitch is 10% while that of the 110 µm pixel pitch detector is 7%. Fig. 4.26 (c) and (d) shows that the average cluster size of 55 µm pixel detector is 600 µm, which is 200 µm bigger than for the 110 µm pixel. There is no conclusive explanation for such a difference yet. However, it could be associated with different electric field profiles near the pixels of different sizes under the same biasing conditions and detector thicknesses. This results in additional diffusion of charge on the smaller pixel.

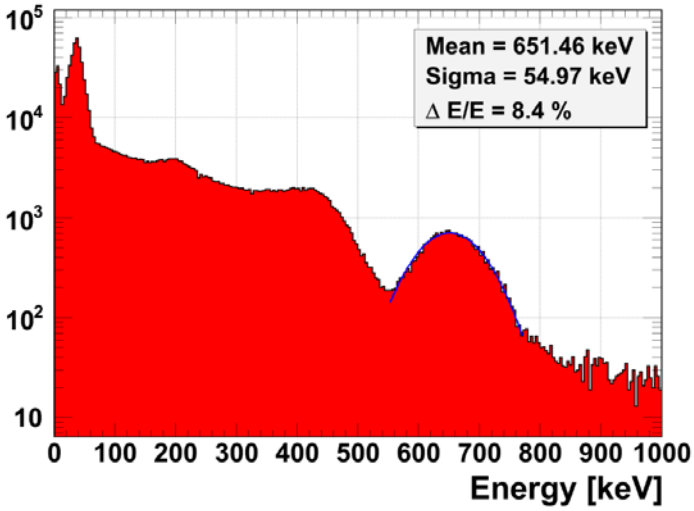

(a) 55 x 55µm pixel energy spectrum

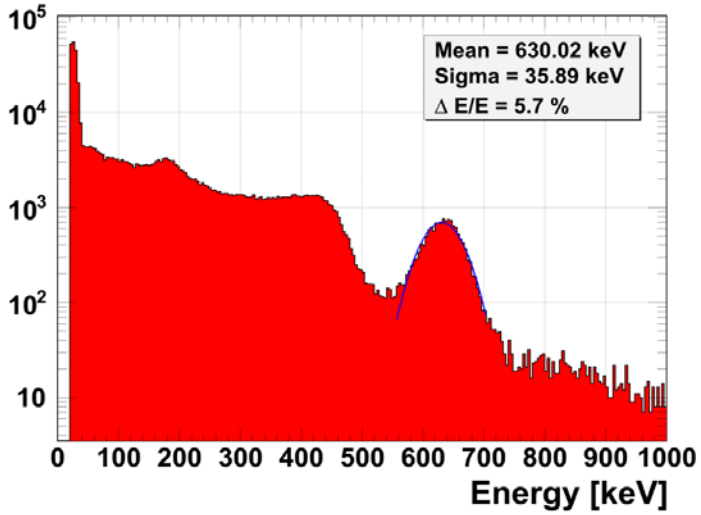

(b) 110 x 110 µm pixel energy spectrum

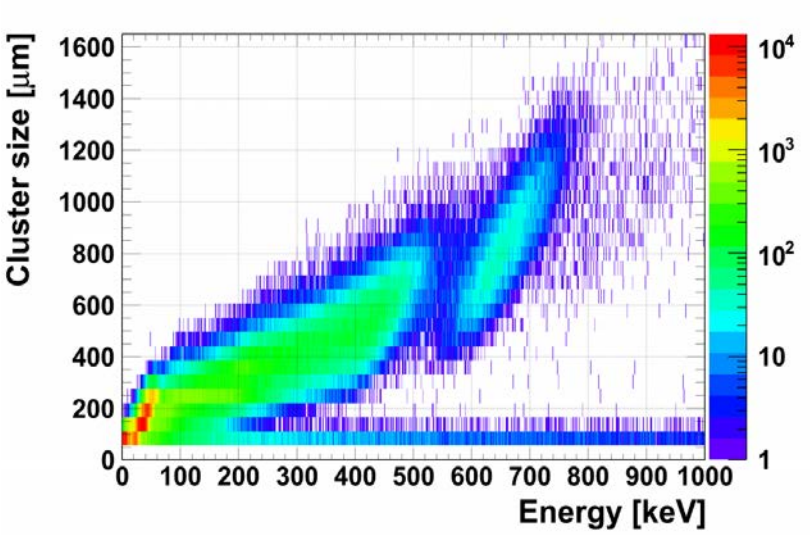

(c) 55 x55μm pixel cluster size-charge map

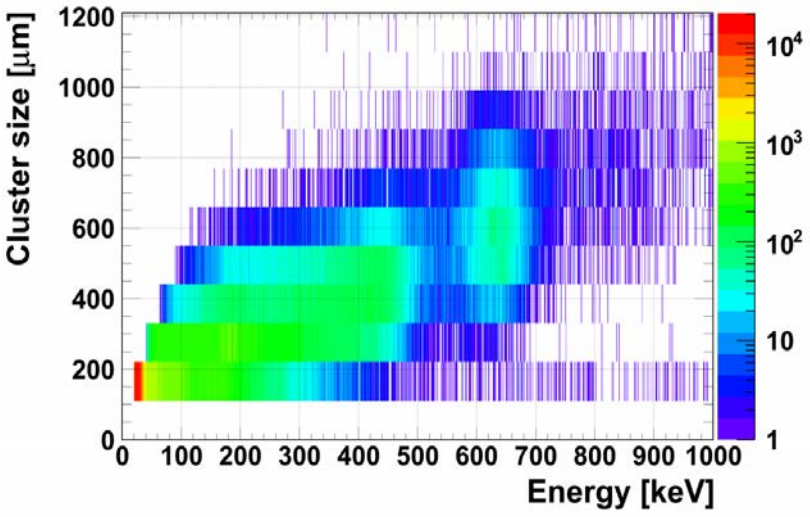

(d) 110 x110μm pixel cluster size –charge map

Figure 4.25: *^{137}Cs energy spectrum comparison between 55 μm and 110μm pixel 1 mm CdTe Timepix Detector*

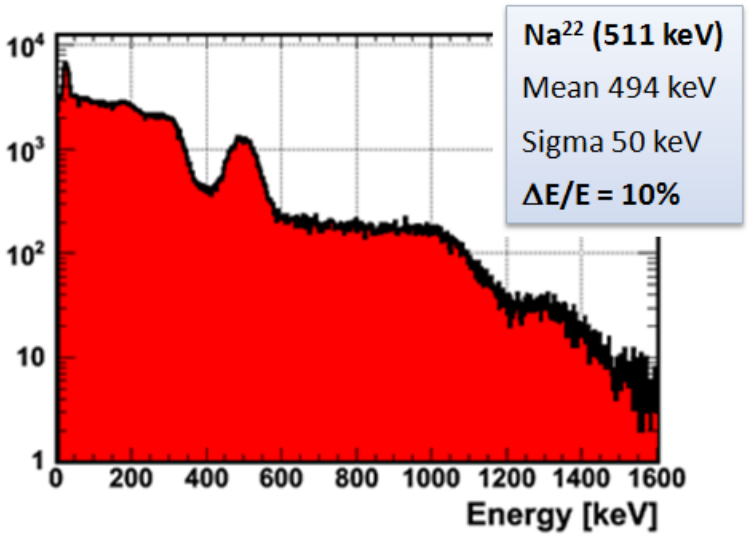

(a) 55 x 55µm pixel energy spectrum

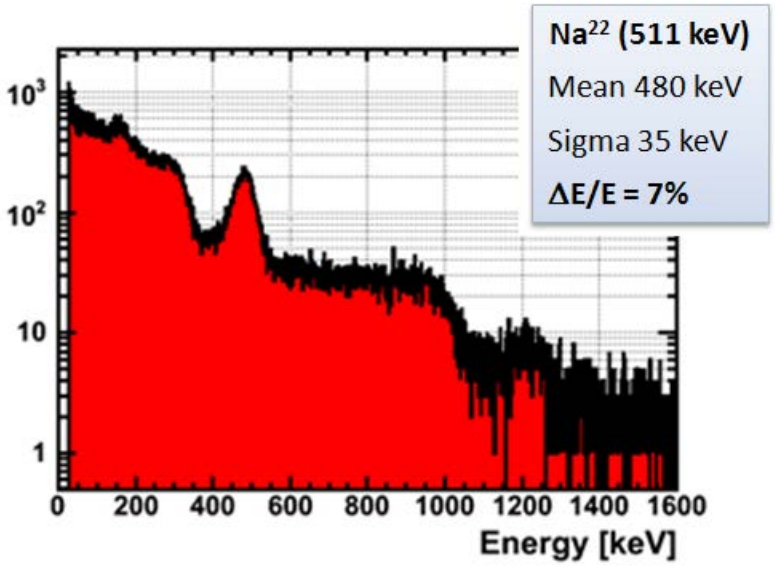

(b) 110 x 110 µm pixel energy spectrum

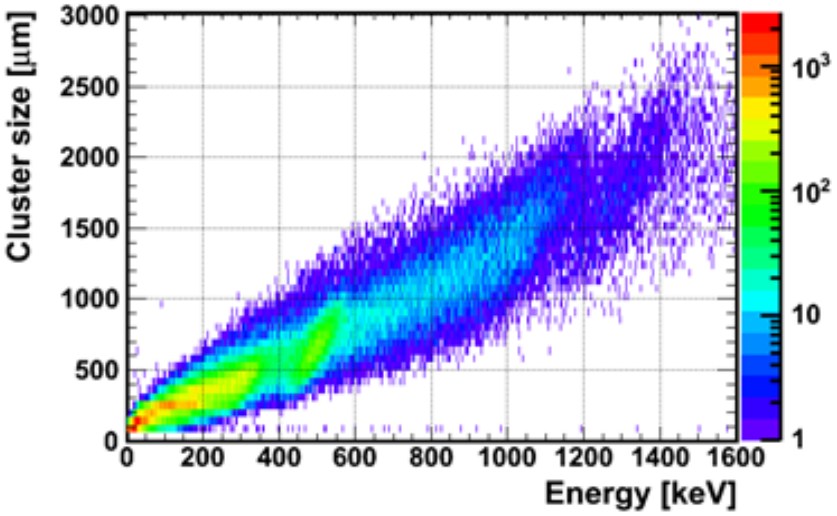

(c) 55 x55µm pixel cluster size-charge map

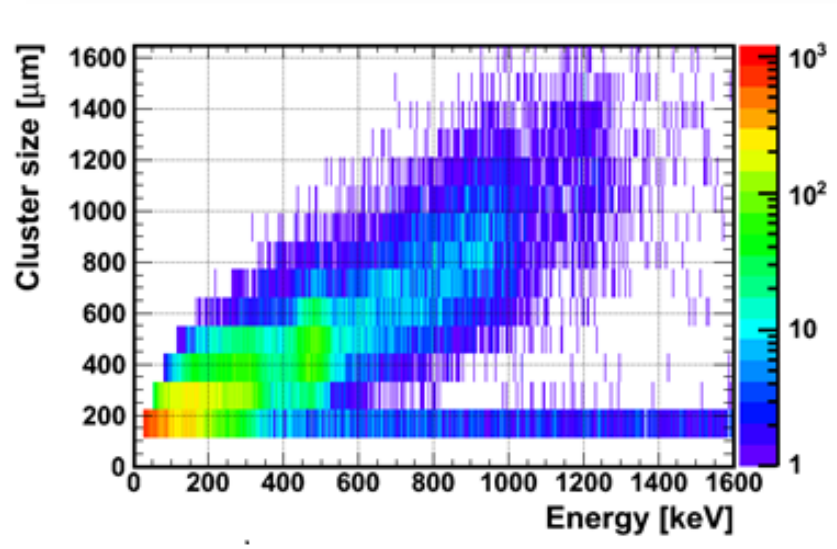

(d) 110 x110µm pixel cluster size –charge map

***Figure 4.26**: ^{22}Na energy spectrum comparison between 55 µm and 110µm pixel 1 mm CdTe Timepix Detector*

The effect of bias voltage on energy spectrum performance for the γ-ray measurements was investigated. The energy resolution of the 55 µm pixel detector was studied as a function of the bias voltage using the 511 keV peak of the ^{22}Na source. The effect of raising the bias can be seen in Fig.4.27. The resolution improves from 13% at -100 V bias voltage to 9% at -500 V. Below -100 V the energy spectrum is significantly

distorted, while above -500 V leakage current becomes too large (above -100 µA) to perform measurements.

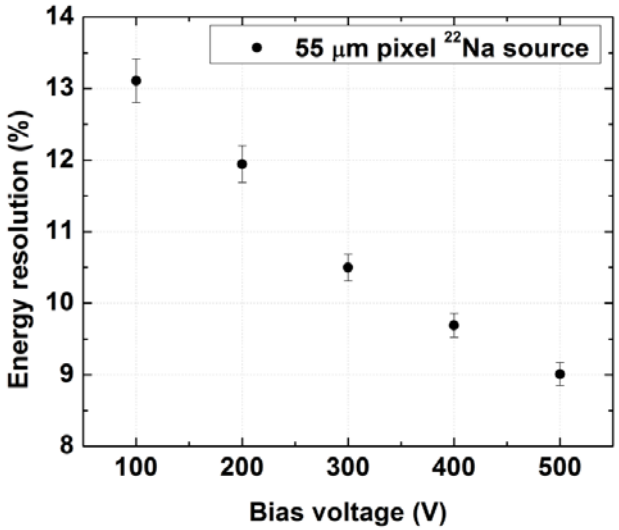

Figure 4.27: *^{22}Na 511 keV peak energy resolution dependence of the 55 µm pixel CdTe detector from bias voltage*

The stability of the detector operation under normal conditions was assessed over a period of 8 hours. The bias voltage was set to -300 V and energy spectrum of *^{22}Na* was taken every hour during the day at room temperature. Variation of energy resolution is shown in Fig.4.28. No degradation in the detector performance was observed. Leakage current was also stable at 9.5±0.8 µA.

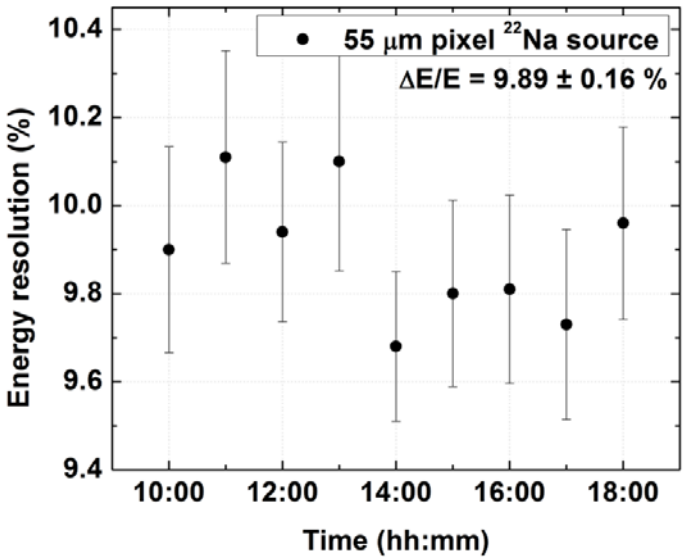

Figure 4.28: *^{22}Na 511 keV peak energy resolution time dependent stability of the 55 μm pixel CdTe detector.*

X-ray Fluorescence

Experiments were performed using an industrial x-ray tube facility at the Diamond light source. X-ray spectra were acquired on an X-ray tube generator with a Molybdenum anode target. The X-ray tube voltage range can be set between 0 – 50 kV and the current range from 0 to 50 mA in continuous output. For the experiment no filtration was used above the K-edges of the calibration foils at 50 mA. The detector was placed at an angle of 90 degrees to the collimator of the tube. The fluorescence from metal sheets placed 45 degrees to the incident beam and the detector was used to produce quasi-monoenergetic X-rays for energy spectra estimation. Table 4.1 shows the result of energy resolution of 110 μm CdTe Timepix detector. All the measurement applied cluster analysis. Fig. 4.29 shows the energy spectrum of K-α.

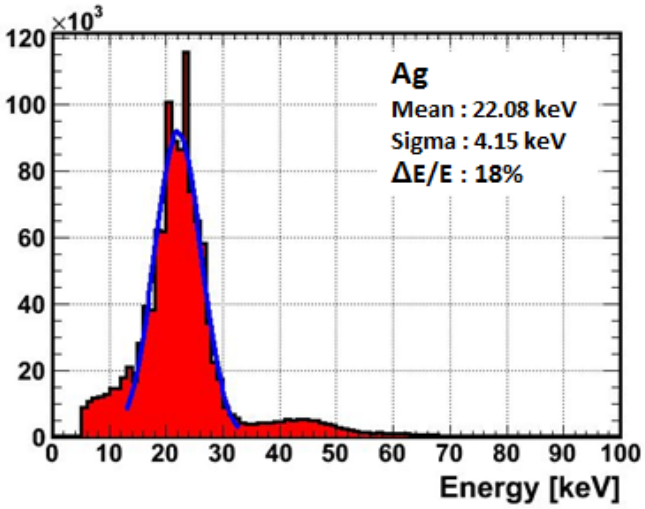
×10³
Ag
Mean : 22.08 keV
Sigma : 4.15 keV
ΔE/E : 18%
Energy [keV]

(a) Ag

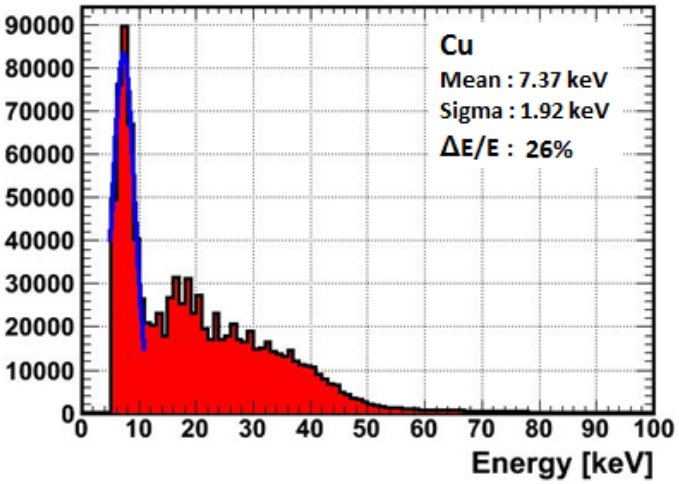
Cu
Mean : 7.37 keV
Sigma : 1.92 keV
ΔE/E : 26%
Energy [keV]

(b) Cu

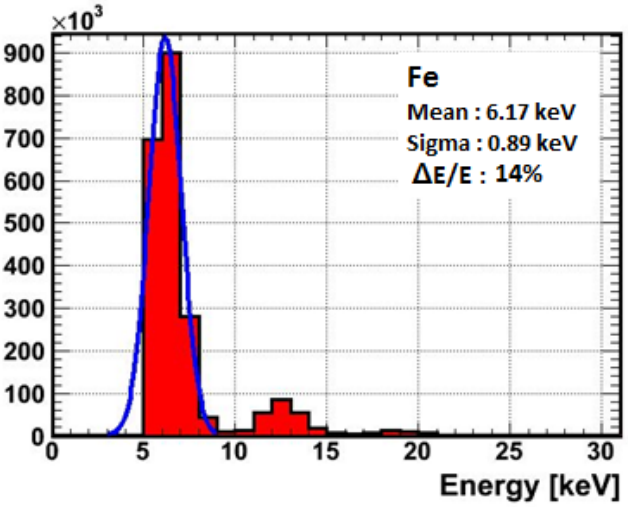
×10³
Fe
Mean : 6.17 keV
Sigma : 0.89 keV
ΔE/E : 14%
Energy [keV]

(c) Fe

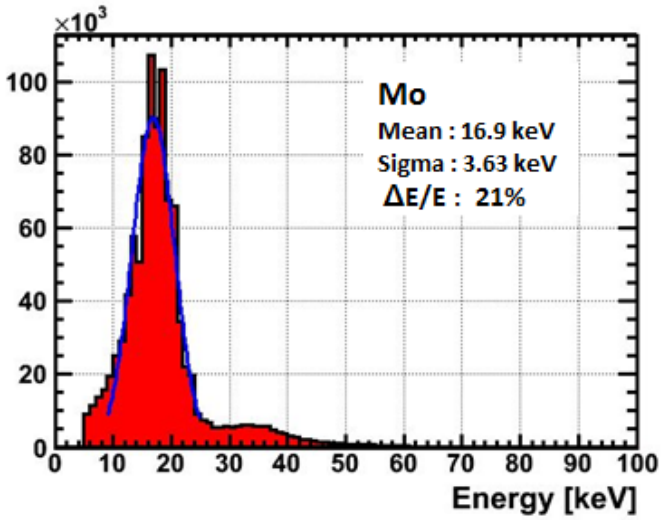

(d) Mo

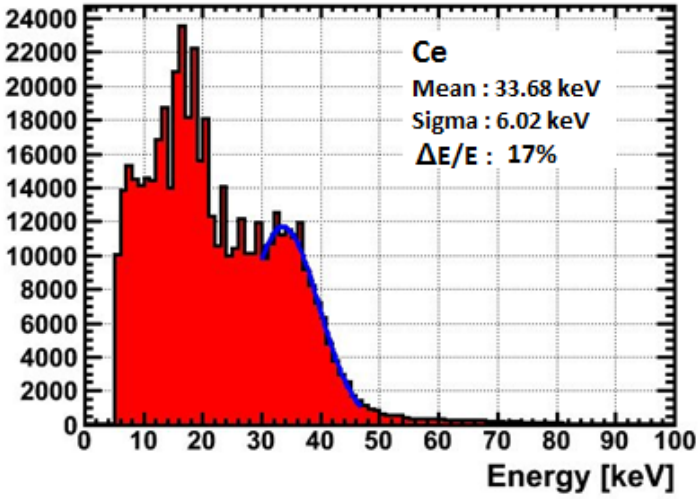

(e) Ce

Figure 4.29 : K-α x-ray energy spectrum

Table 4.1 *Energy resolution of X-ray Tube 110 µm CdTe Timepix Detector.*

X-ray	Spectrum Energy, keV	Energy Resolution, R
Ag	22.1	18%
Cu	8.0	26%
Fe	6.4	14%
Mo	17.5	21%
Ce	34	17%

4.6 Experiment at Synchrotron beam line

Synchrotron radiation measurements were performed at the Extreme Conditions beam line I15 of the Diamond Light Source [71]. The schematic and photograph of the experimental setup is shown in Fig.4.30 (a). The detector was placed perpendicular to the incident photon flux and aligned with a laser pointer.

- 1st Experiment (2011):

  For 110 x110 µm pixel pitch *CdTe* Timepix detector, a scan of 220 µm across three pixels was performed at energies of 25, 29, 33, 40 and 77 keV from the centre of the left most pixel to centre of the rightmost pixel. The step size of 10 µm was chosen to ensure adequate oversampling. The beam size was measured to be 20 µm FWHM at 40 keV. Energy spectra plots from the data were reconstructed from the beam incident in the middle of the pixel under test. Fig. 4.30 (b) shows the pencil beam of synchrotron positioned at the centre of the pixel.

- 2nd Experiment (2012):

  In order to compare the performance between pixel sizes the experiment was set-up so that the monochromatic X-ray Synchrotron beam was focussed on the centre of a pixel. Energy resolutions of the detectors were directly compared at two energies, 25 keV and 79 keV.

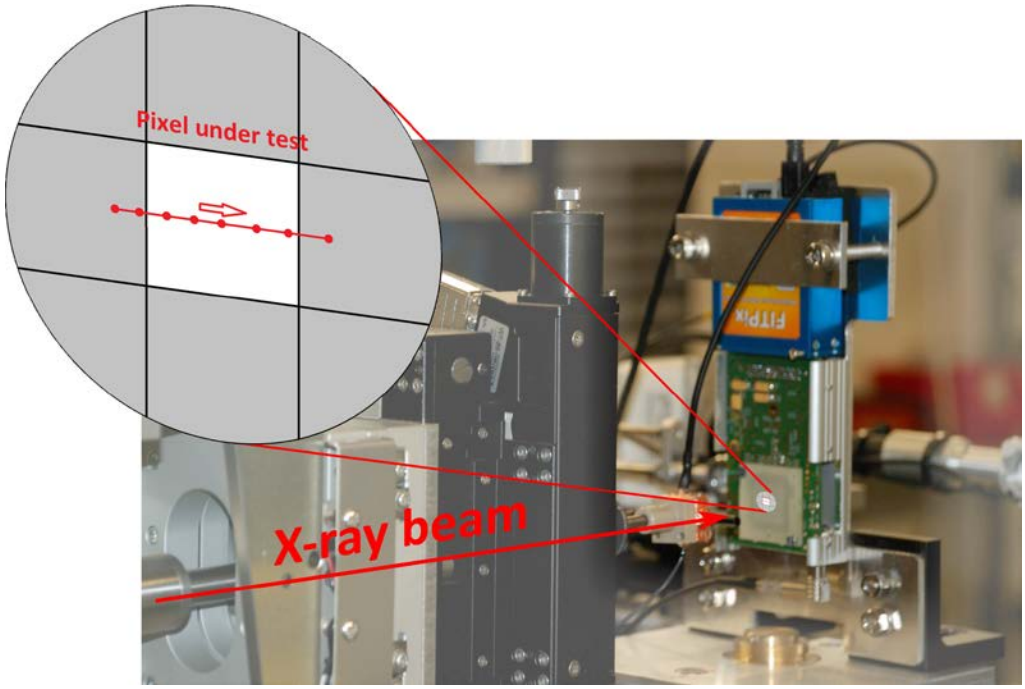

(a)

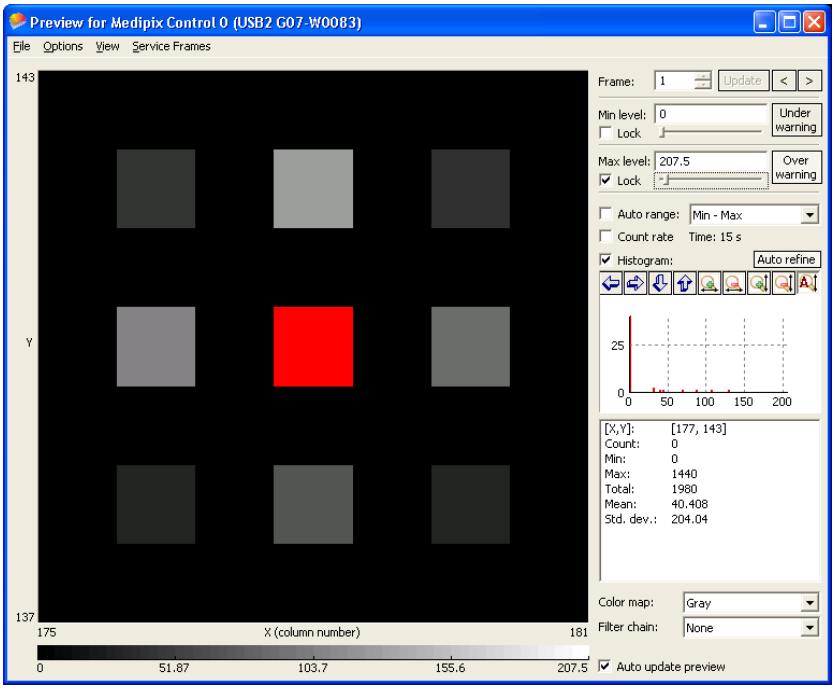

(b)

Figure 4.30: *(a) Schematic and photo of experimental setup at I15 beam line in Diamond synchrotron. The normally incident monochromatic X-ray beam was scanned across three pixels in ToT mode. (b) Pencil beam of monochromatic synchrotron beam focussed on the centre of the pixel.*

Beam profile reconstruction

The I15 beam line cannot provide reliable information on the X-ray beam size incident on the detector, especially at energies above ~ 40 keV. Nevertheless, in the charge sharing and fluorescence studies it has been seen that the secondary photon range is comparable to the pixel size as well as the beam size. Hence it is important to have a very clear quantitative understanding on the convolution of the beam size with other effects.

In order to reconstruct an effective beam size a pixel was oversampled by steping the beam across it at 10 µm steps from the centre of the neighbour pixel to the centre of the following pixel. A toy simulation model for a 55 µm pixel was created in ROOT to assist beam size separation from the two other main contributing effects - charge sharing / fluorescence and pixel energy threshold. The ideal pixel response to a point like 25 keV beam is shown in Fig. 4.31 (a). It is represented by a sharp step function. Introduction of the finite size Gaussian beam with FWHM between 2.5 and 10 µm results in a convolution shown in Fig. 4.31 (b). Fig 4.31 (c) shows how charge sharing can effect the beam size. The effect of threshold imposed on the pixel is depicted in Fig. 4.31 (d). The response function shrinks as threshold is increased. The results of the toy model simulations point to a few assumptions that need to be taken into account for the beam size reconstruction. The assumptions for the toy model are:

- The variation of the incident beam size affects the shape of the pixel response function.

- Charge sharing and threshold are responsible for the broadening of the pixel response only.

- The threshold is set to E/2 for each measurement to study to minimise the effects of charge sharing.

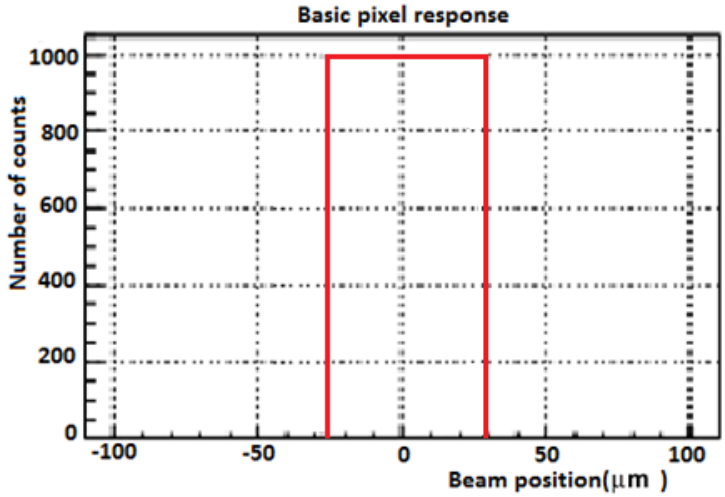
Basic pixel response
Number of counts
1000
800
600
400
200
0
-100
-50
0
50
100
Beam position(μm)

(a)

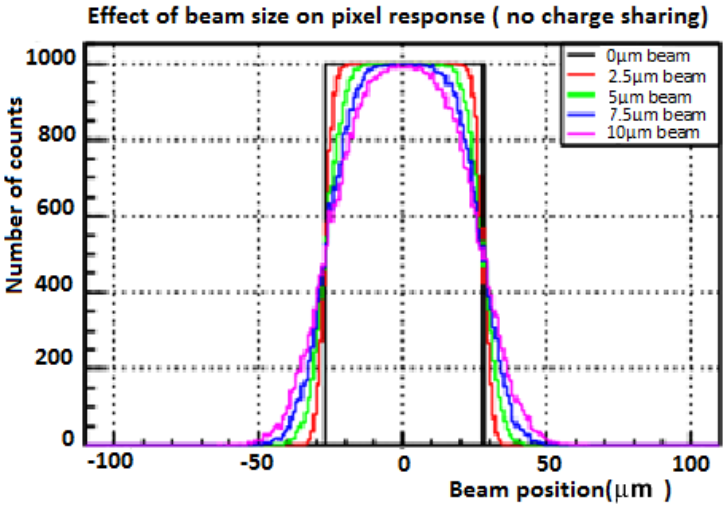
Effect of beam size on pixel response (no charge sharing)
Number of counts
1000
800
600
400
200
0
-100
-50
0
50
100
Beam position(μm)
0μm beam
2.5μm beam
5μm beam
7.5μm beam
10μm beam

(b)

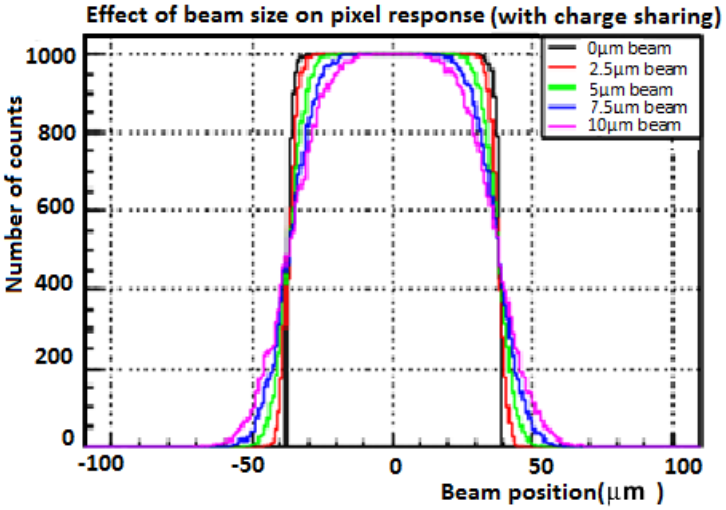
Effect of beam size on pixel response (with charge sharing)
Number of counts
1000
800
600
400
200
0
-100
-50
0
50
100
Beam position(μm)
0μm beam
2.5μm beam
5μm beam
7.5μm beam
10μm beam

(c)

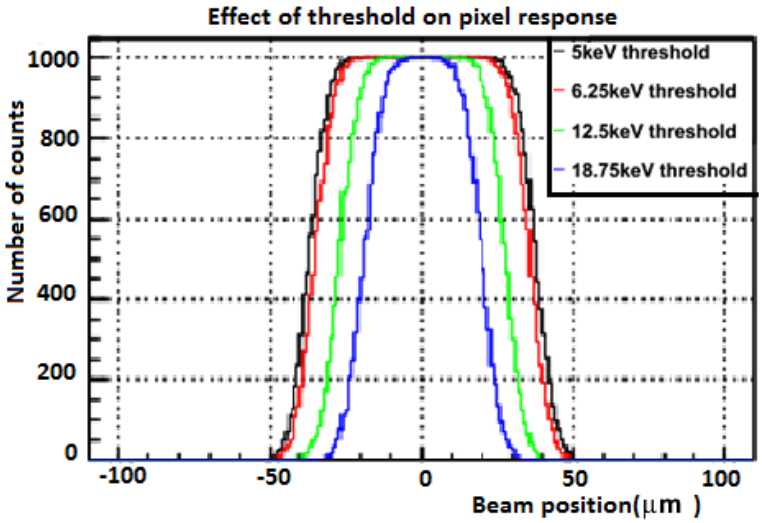

(d)

Figure 4.31:*Beam profile reconstruction: (a) Basic pixel response, (b) Effect of beam size on pixel response (no charge sharing), (c) effect of beam size on pixel response (with charge sharing), (d) Effect of threshold on pixel response*

Taking into account these assumptions, the incident X-ray beam size can be de-convoluted from the recorded pixel response in the following way. The acquired pixel response is fitted with an Error function (ERF function). The new function is differentiated and the result is fitted with a Gaussian function. Sigma or FWHM extracted from the fit represents the X-ray beam size incident on the detector. Using this technique the effective beam size was measured to be σ = 4.71 μm at 25 *keV* and σ = 9.51 *μm* at 79 *keV*. Fig. 4.32 shows the result of the process as described earlier.

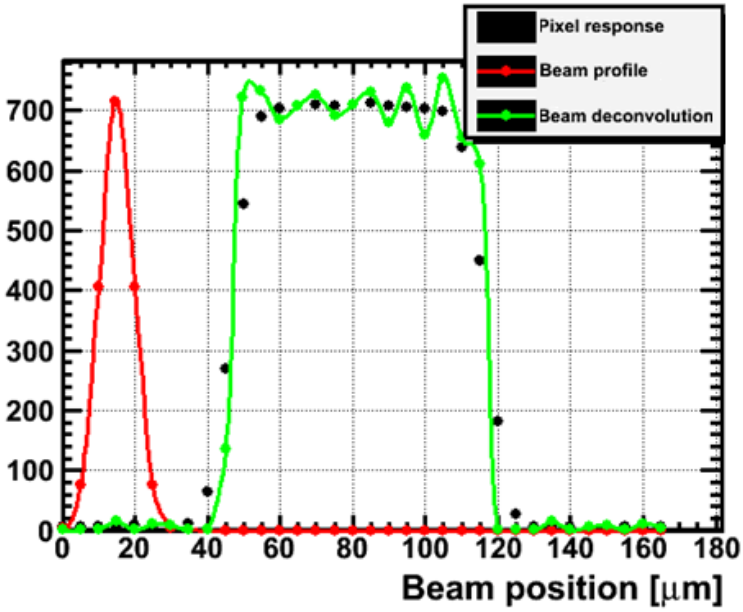

(a)

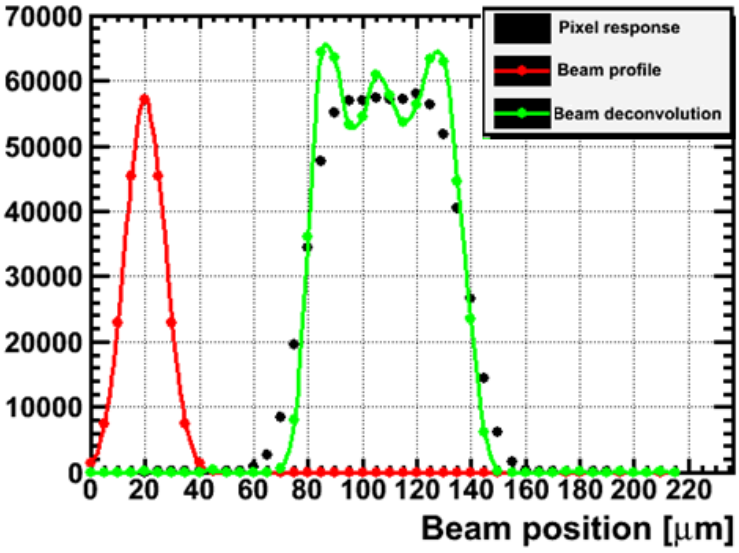

(b)

Figure 4.32: *Beam profile and beam deconvolution: (a) 25 keV (b) 79 keV*

Charge sharing

The energy resolution of the pixelated detector is influenced by the charge sharing effect [72]-[74]. This effect originates from the fact that the charge created by the incoming photon spreads out between several adjacent pixels (depending on the place of interaction and the detector parameters, e.g. bias voltage). Single photon counting detectors such as Timepix compare the collected charge in each pixel to a certain threshold level and, if it is lower, the event is not registered and the charge is lost. As a consequence, the energy resolution deteriorates.

A collimated beam of synchrotron x-rays was used to probe the 110 μm pixel-pitch detector response across a single pixel. The collimated beam was provided by the I15 beam line at the Diamond Light Source Synchrotron research facility. This beam line is capable of providing variable monochromatic beam energy between 15 keV and 80 keV. The beam was collimated using two sets of slits where the first set sets the width of the beam to be 10 μm and the second set was responsible for setting the height to be 10 μm. The detector was mounted on precision translational and rotational stages giving 6 degrees of freedom.

The pencil beam is used to perform a pixel scan of the surface of the detector. A 220 μm scan across three pixels was performed at 25 and 40 keV. With this method the point spread function (PSF) of a single pixel could be obtained. The PSF profile for 25 and 40 keV are shown in Fig. 4.33 and 4.34. The choice of 25 and 40 keV is motivated by the fact that both Cd and Te fluorescence edges occur above 25 keV and so will be present in only one of the data sets.

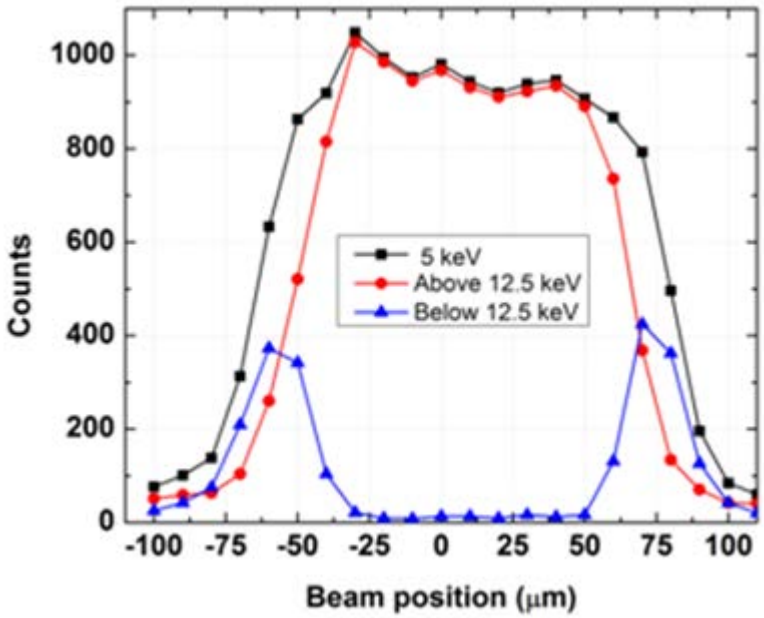

Figure 4.33: *Counts recorded on two neighbour pixel at 25 keV energy (110 μm pixel pitch).*

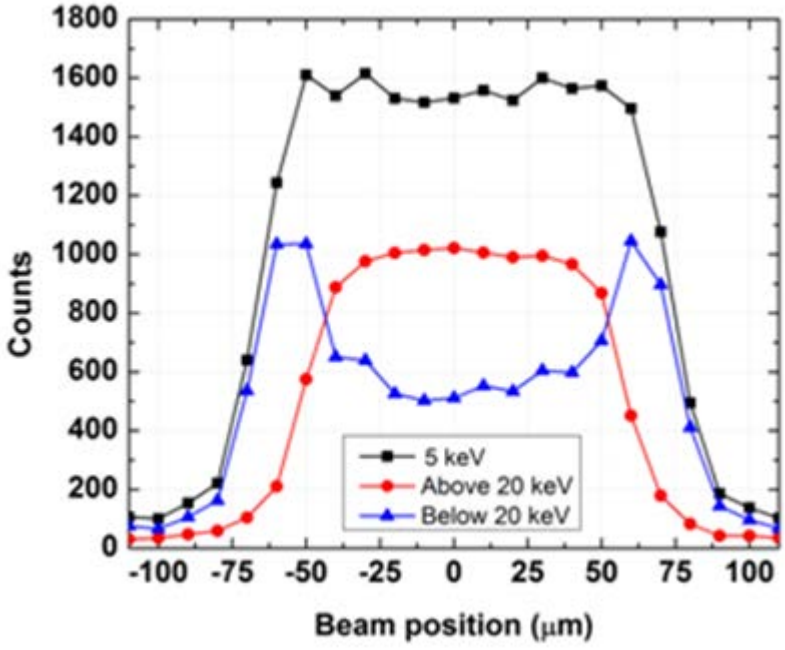

Figure 4.34: *Counts recorded on two neighbor pixel at 40 keV energy (110 μm pixel pitch).*

Fig. 4.35 shows the energy to count conversion for pixels #175 - #139, #177- #139 and # 179 - #139 with different threshold settings for the 25 keV beam. Superimposed count profiles from neighbouring pixel (*x-1, x, x+1*) show the extent of charge sharing across the pixels. The counting threshold were set at three different energies, such that the first threshold was just above noise (> 5 keV), the next just above half of the beam energyenergy (> 12.5 keV) and the last below half of energy (< 12.5 keV). The threshold energy below 12.5 keV shows where charge sharing occurs as there are two peaks on the edge of the pixel. From the observation also it shows there are almost no counts inside the pixel. Threshold above >12.5 keV data shows spurious counts from both the fluorescence and charge sharing. Meanwhile Fig.4.36 shows the results of the same measurements with a beam energy of 40 keV. In this case the measurement with threshold below < 20 keV had both charge sharing and fluorescence.

The measured values of FWHM for the 25 keV and 40 keV energies are shown in Fig. 4.37 and 4.38. For the 25 keV beam (threshold below *E/2*) the FWHM of the charge sharing peaks at the edges of the pixel are 10.98 and 10.50. For the 40 keV energy (threshold below *E/2*) the values increase to 13.01 and 12.04. These features happen due to the effect of charge sharing and fluorescence.

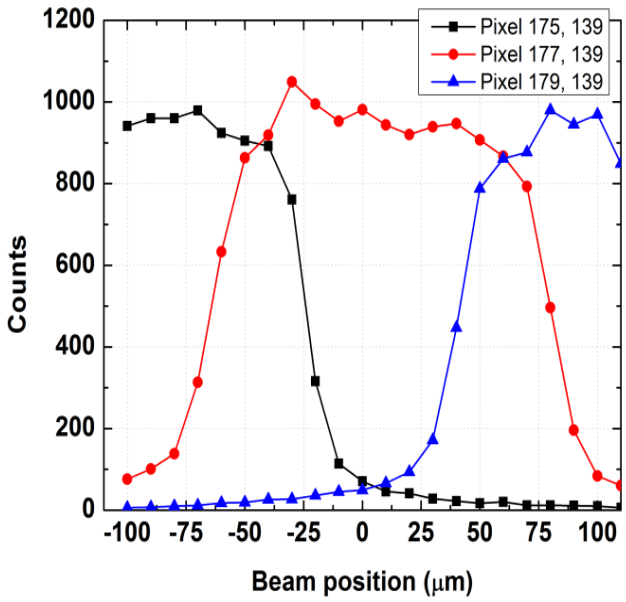

(a) Threshold above noise (>5 keV)

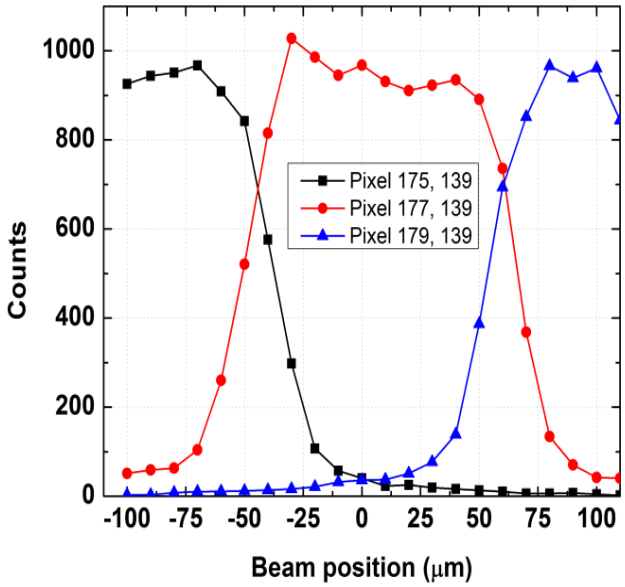

(b) Threshold above E/2 (>12.5 keV)

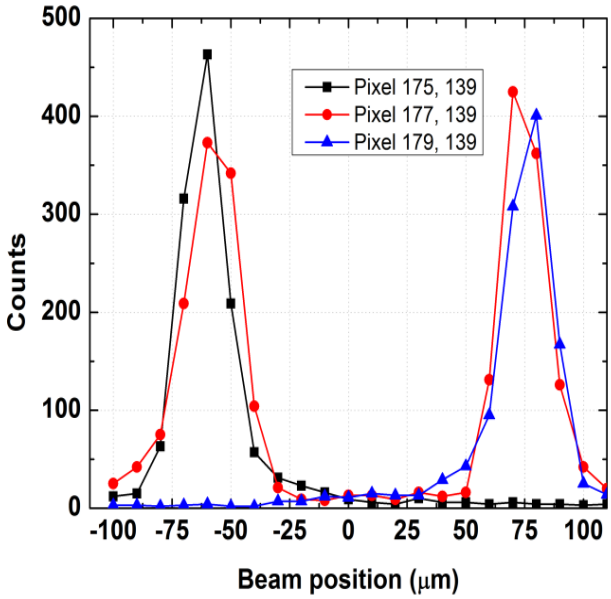

(c) Threshold below E/2 (<12.5 keV)

Figure 4.35: *25 keV pixel scan (110 μm pixel pitch).*

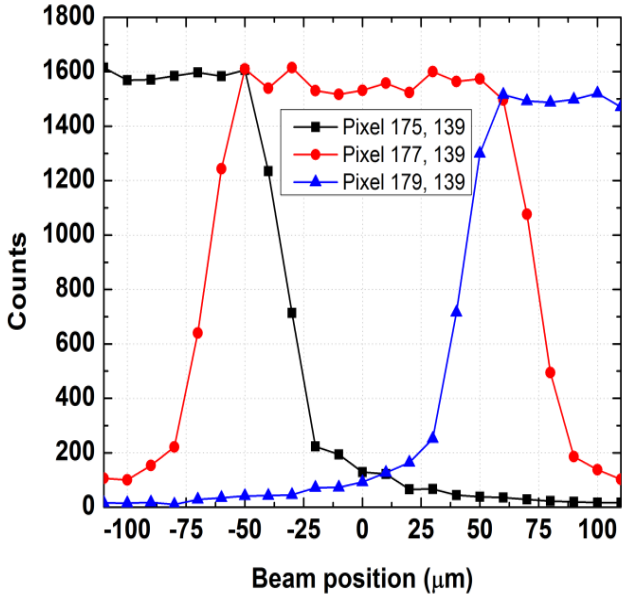

(a) Threshold above noise (>5 keV)

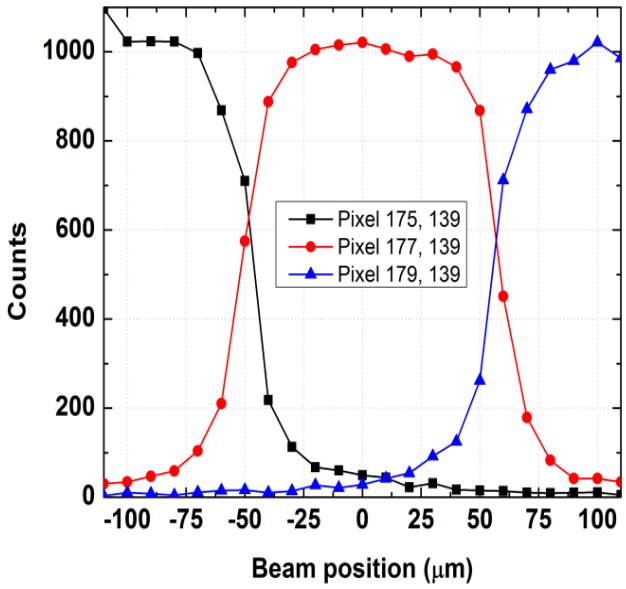

(b) Threshold above E/2 (>20 keV)

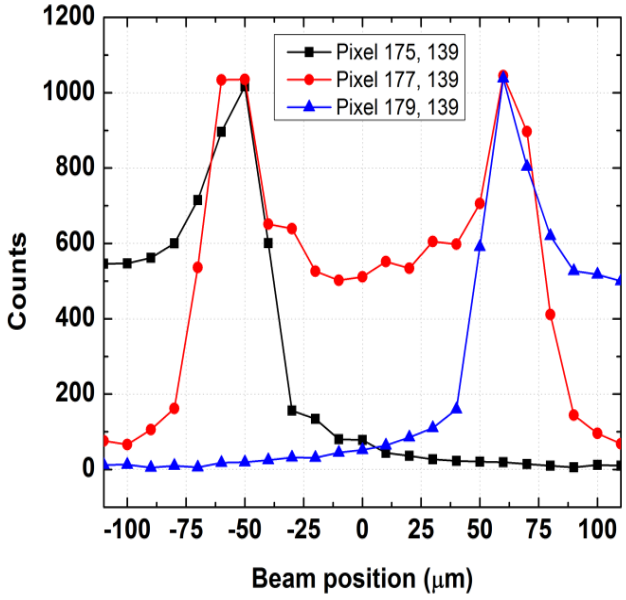

(c) Threshold below E/2 (<20 keV)

Figure 4.36: *40 keV pixel scan(110 μm pixel pitch).*

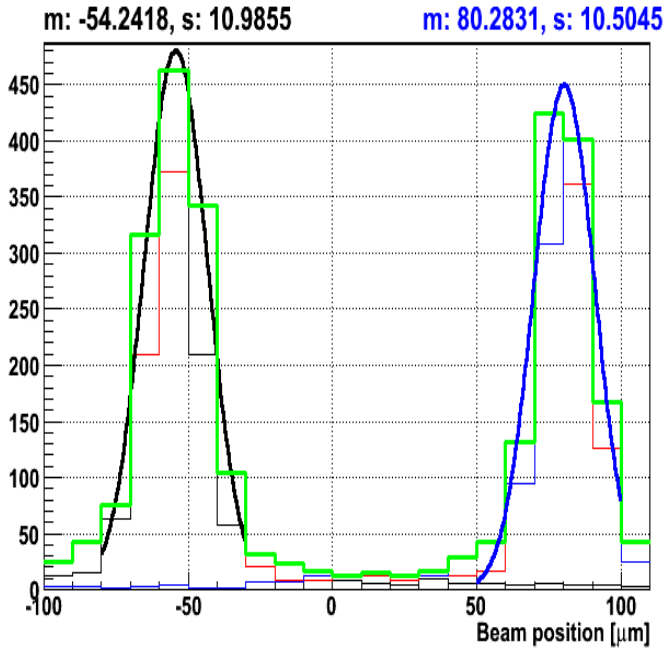

Figure 4.37*: FWHM for 25 keV (charge sharing effect)*

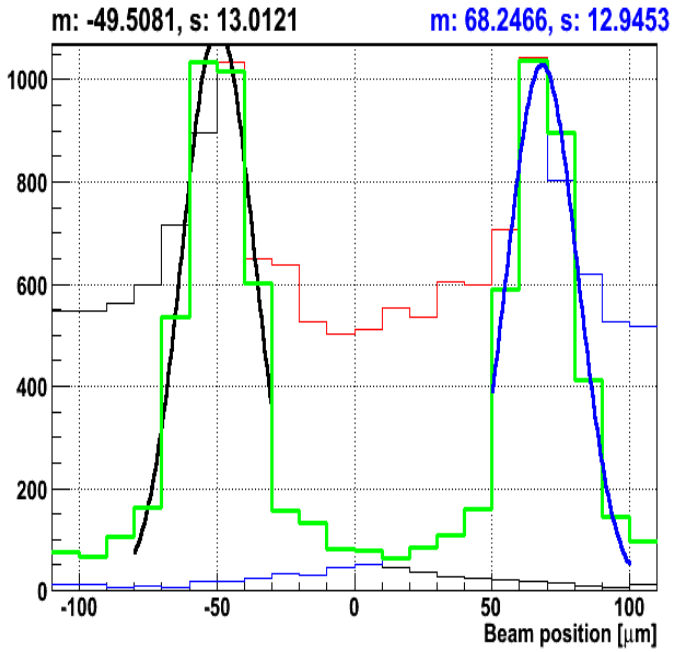

Figure 4.38: *FWHM for 40 keV (Charge sharing + fluorescence effect)*

Energy resolution analysis

The spectroscopic performances of both 55mm and 110mm detector assemblies were evaluated in the range of 25, 29, 33, 40, 77 and 79 keV using monochromatic synchrotron radiation. The thresholds for both detectors were set globally to ~ 5 keV. The default Timepix clock was set to 48MHz and the bias voltage to -300V. The chip was operated in an electron collection mode. No spectra correction or enhancement was performed, since the goal of this study was to establish the bottom line performance of the device.

In the first experiment at Diamond; Fig. 4.39, 4.40, 4.41, 4.42 and 4.43 shows spectra recorded by the 110 μm pitch detector under monochromatic synchrotron radiation at 25, 29, 33, 40 and 77 keV. The energy resolution, calculated as $R = \Delta E / E$, is as shown in Table 4.2. The results indicate that the energy resolution improves dramatically with increasing beam energy as shown in Fig. 4.44.

For the 77 keV plot both escape and fluorescence peaks are clearly seen. The escape occurs when a photoelectrical event removes a core electron from an atom in the detector leaving a vacancy which then has to be filled. The excess energy is typically released as a fluorescent X-ray photon which escapes from the detector and can be seen in Fig 4.43.

Table 4.2: *Result of Energy resolution for 110 µm CdTe Timepix Detector*

Spectrum Energy, keV	Energy Resolution, R
25	9.0%
29	8.6%
33	8.1%
40	7.0%
77	3.9%

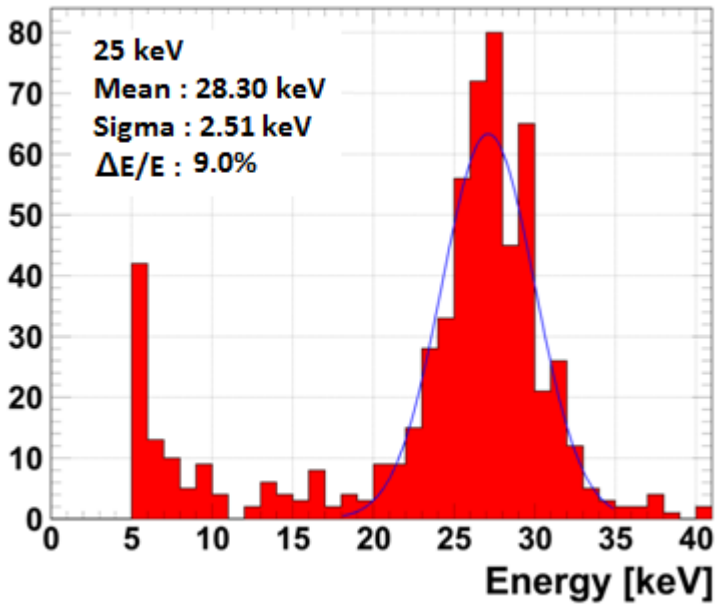

Figure 4.39: *25 keV spectrum for CdTe Timepix detector*

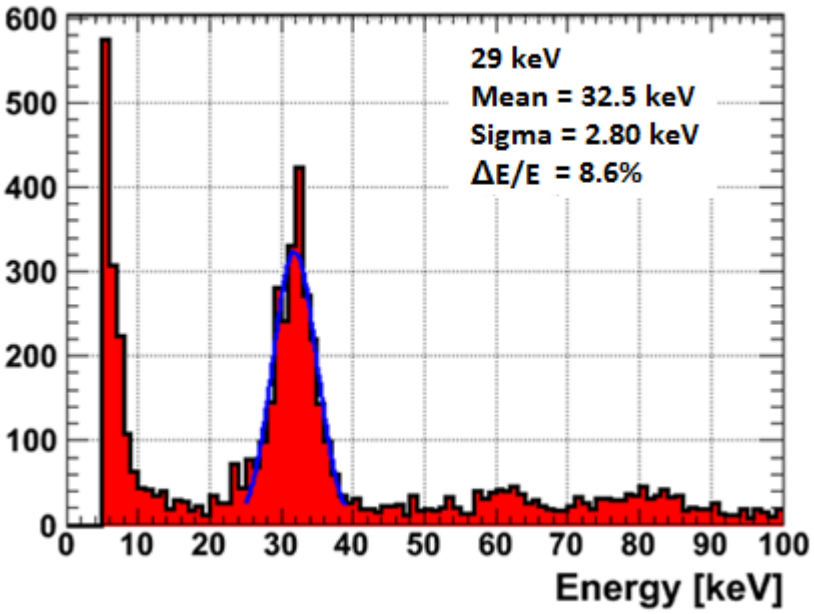

Figure 4.40: *29 keV spectrum for CdTe Timepix detector*

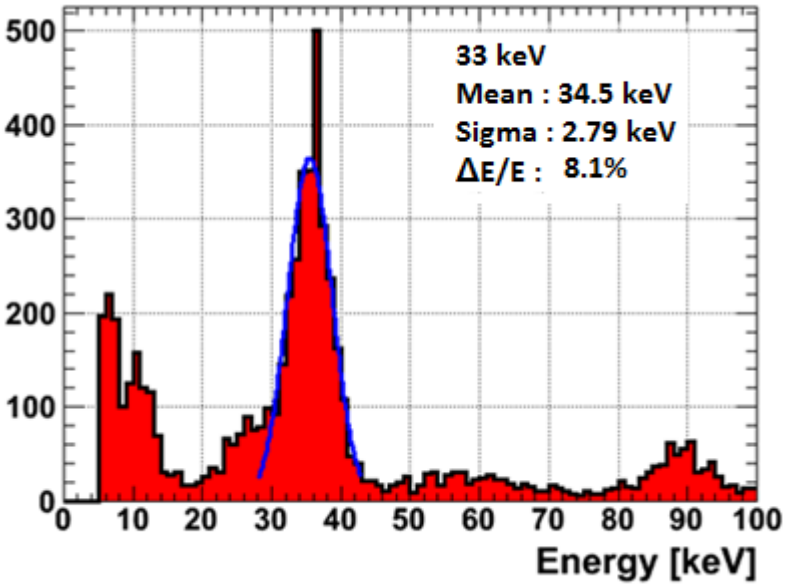

Figure 4.41: *33 keV spectrum for CdTe Timepix detector*

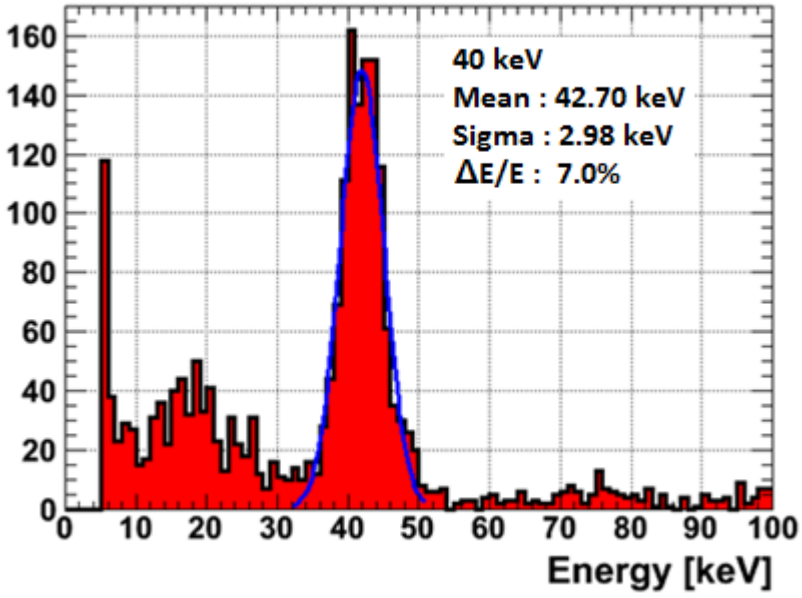

Figure 4.42: *40 keV spectrum for CdTe Timepix detector*

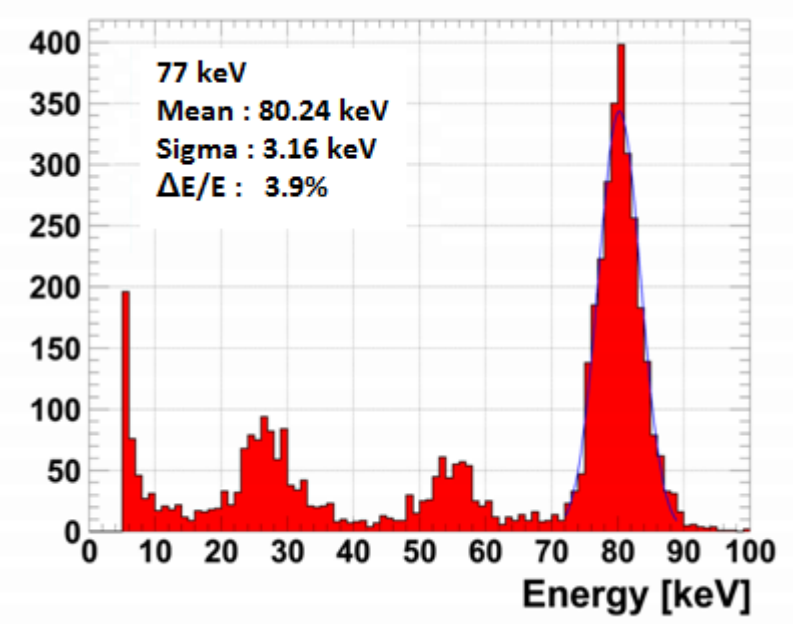

Figure 4.43: *77 keV spectrum for CdTe Timepix detector*

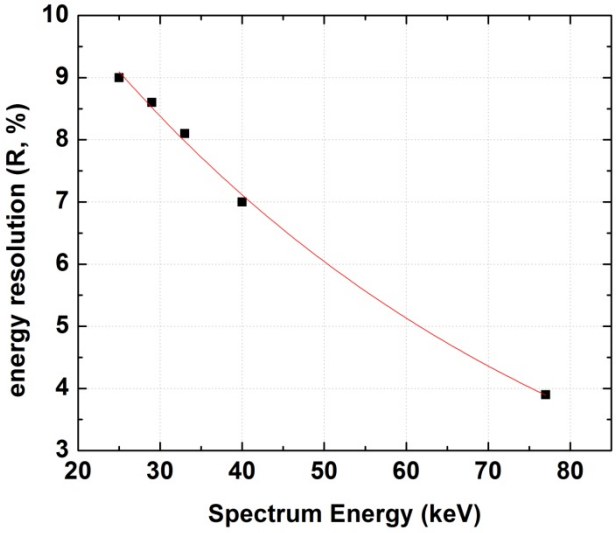

Fig. 4.44: *Energy resolution performance*

The second experiment at Diamond was carried out to compare Energy resolutions of the detectors at two energies, 25 keV and 79 keV, with the X-ray beam incident at the centre of a pixel. At 25 keV both 55 and 110 µm assemblies demonstrated similar performance, see Fig. 4.45. The energy resolution was extracted from the pixel of interest only. The energy resolutions are 7.2% for 55 µm and 8.9% for 110 µm pixel. Both detectors exhibit similar energy resolution performance. In this energy no shared events were identified in either of the assemblies, rendering clustering unnecessary. The result also indicates that the detector performance for 110 µm at 25 keV energy is similar to the energy resolution which was done one year before.

For the 79 keV beam energy the charge cloud size generated becomes comparable to the pixel size. Fluorescence also contributes to the growth of the electron-hole cloud size drifted towards the pixels. The following four plots in Fig. 4.46 show both clustered and single pixel spectra for 55 and 110 µm pixel detectors. The non clustered spectrum for the 55 µm pixel indicates that most of the charge from 79 keV X-rays does not find its way to the main pixel but is shared with neighbouring pixels. This is indicated by the inflated number of counts in the spectrum in the energy range below approximately 20 keV. Clustering allows the recovery of the 79 keV energy peak. A Gaussian fit shows energy

resolution of σ/E_o = 14.2%. The single pixel spectrum from the 110 µm detector shows a substantial improvement in energy resolution compared to that from the 55 µm assembly. The intrinsic single pixel resolution was found to be σ/E_o = 4.3%. The shared charge was also clustered in order to achieve as complete a peak reconstruction as possible. This, however degraded energy resolution to σ/E_o = 7.4%.

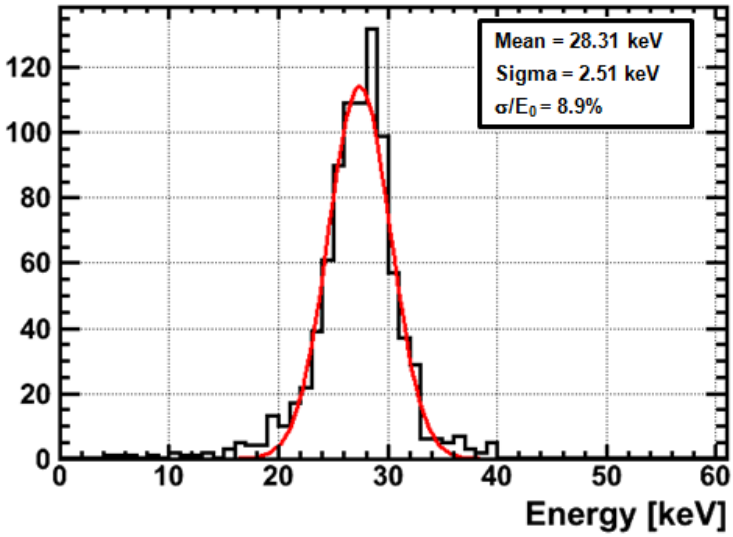

(a)

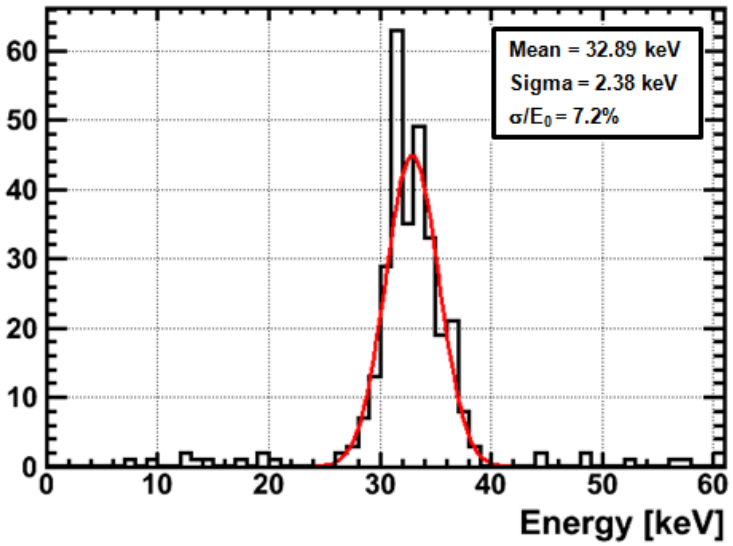

(b)

Figure 4.45: *Spectrum of 25 keV: (a) 110 µm, (b) 55 µm*

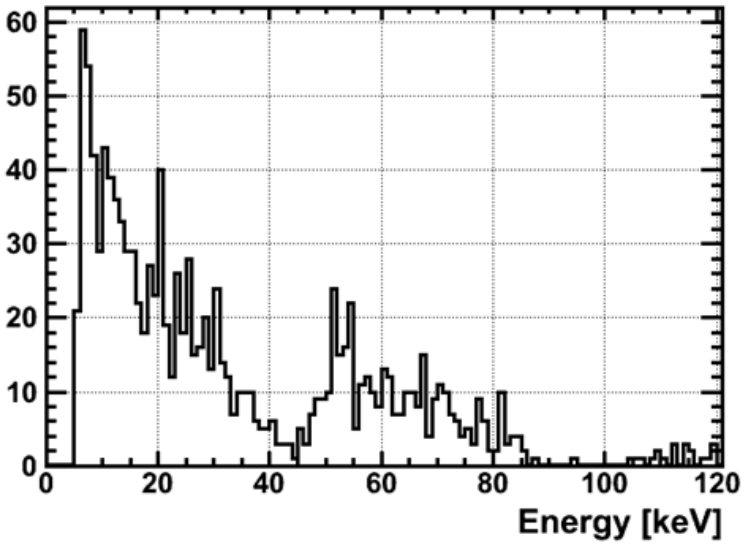

(a) No clustering: 55 µm CdTe Timepix detector

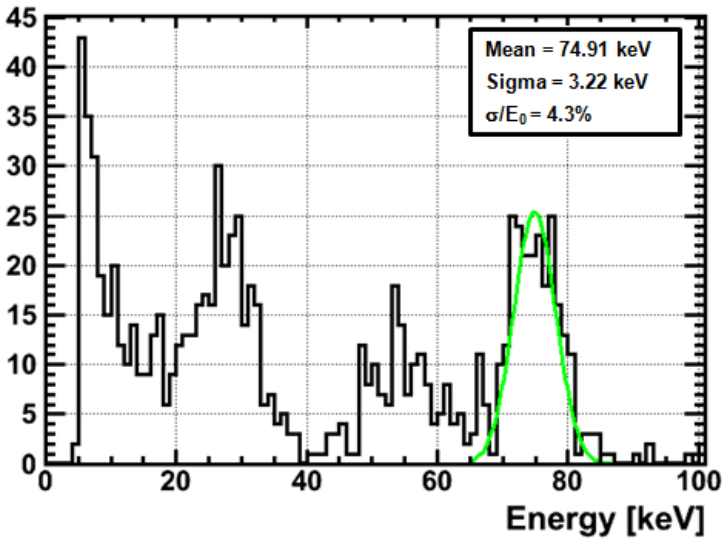

(b) No clustering: 110 µm CdTe Timepix detector

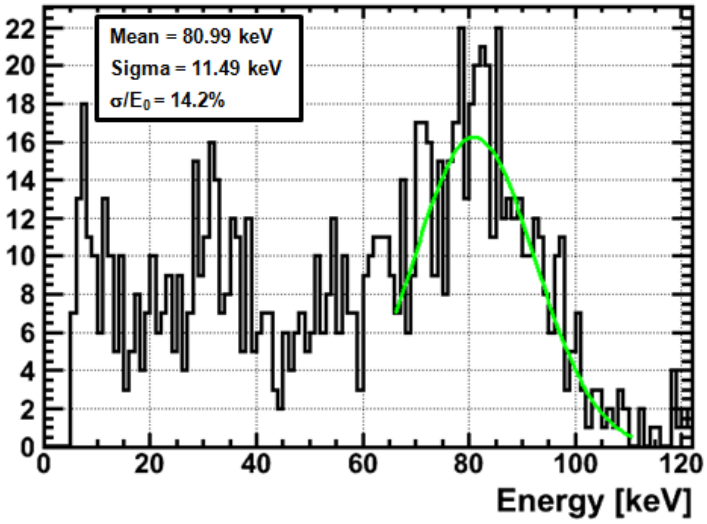

(c) Clustering: 55 µm CdTe Timepix detector

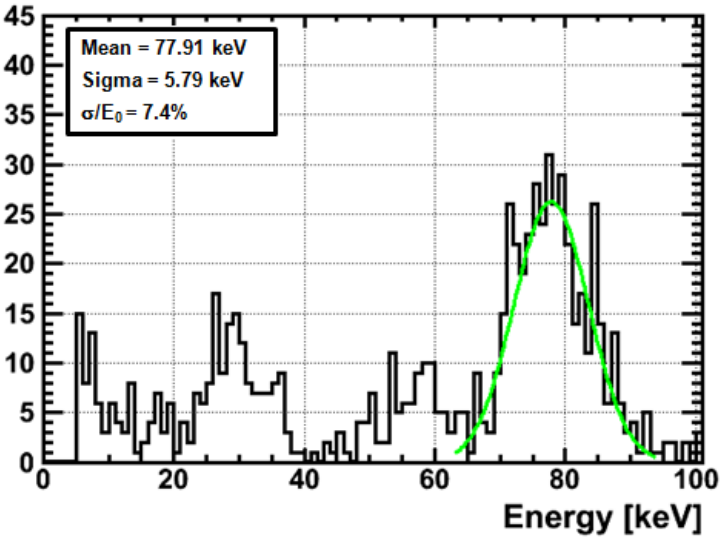

(d) Clustering: 110 µm CdTe Timepix detector

Figure 4.46: *Clustering analysis of 55 and 110 µm CdTe Timepix detector*

Threshold scan

A threshold scan (also known as DAC Scan) has been performed to make a comparison between the two pixel pitch detectors in counting mode for 79 keV beam energy. The modified step function described previously was fitted to the THL DAC scan plot and the energy resolution was extracted in the same way for both detectors giving a direct comparison. From the scan the 79 keV produces in each single pixel measurement two peak in the spectrum; one at 79 keV and also an escape peak as shown in Fig. 4.47 for 55 µm and for 110 µm pixel pitches respectively. Energy resolution recovered from the 79 keV data sets are σ/E_0 = 2.4% for 55 µm and σ/E_0 = 1.5% 110 µm pixel. Meanwhile, for the escape peak σ/E_0 = 6.6 % for 55 µm and σ/E_0 = 5.7% 110 µm pixel. The result shows that the 110 µm *CdTe* Timepix detector a 60% better resolution compared to the 55 µm assembly. The same energy resolution extraction procedure was performed for the pixel of interest only. It was found that the numbers match before and after clustering (Fig. 4.48), indicating that clustering does not degrade the detector performance in counting mode.

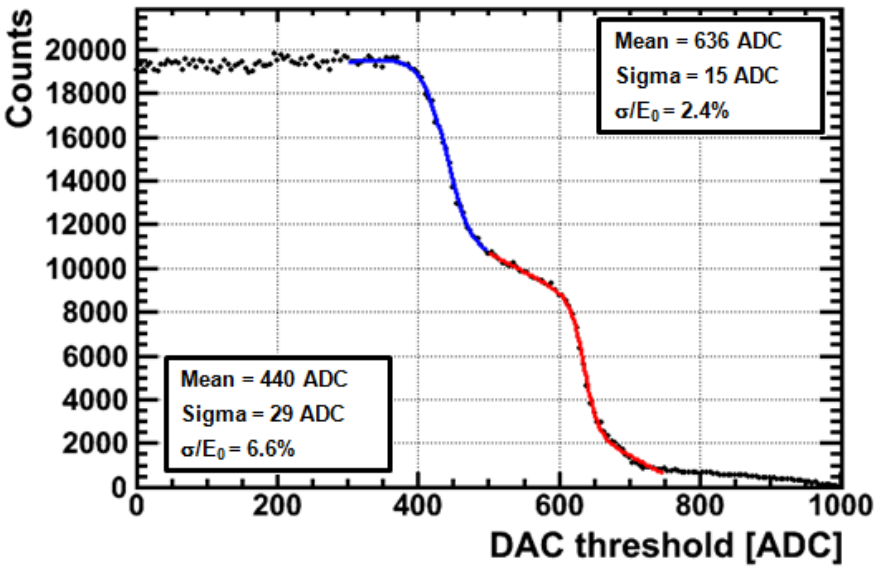

(a)

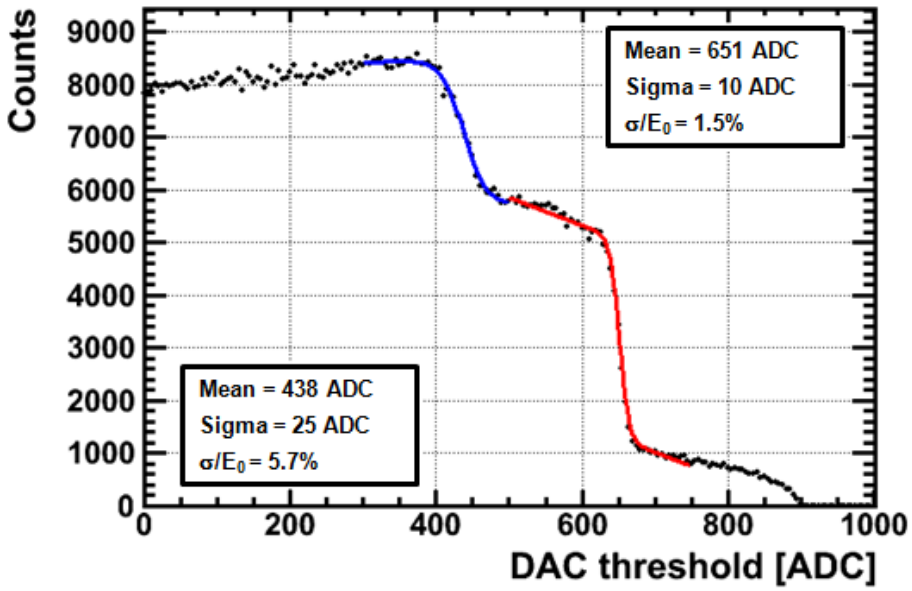

(b)

Figure 4.47: *Threshold scan at 79 keV : (a) 55 µm Timepix detector, (b) 110 µm Timepix detector*

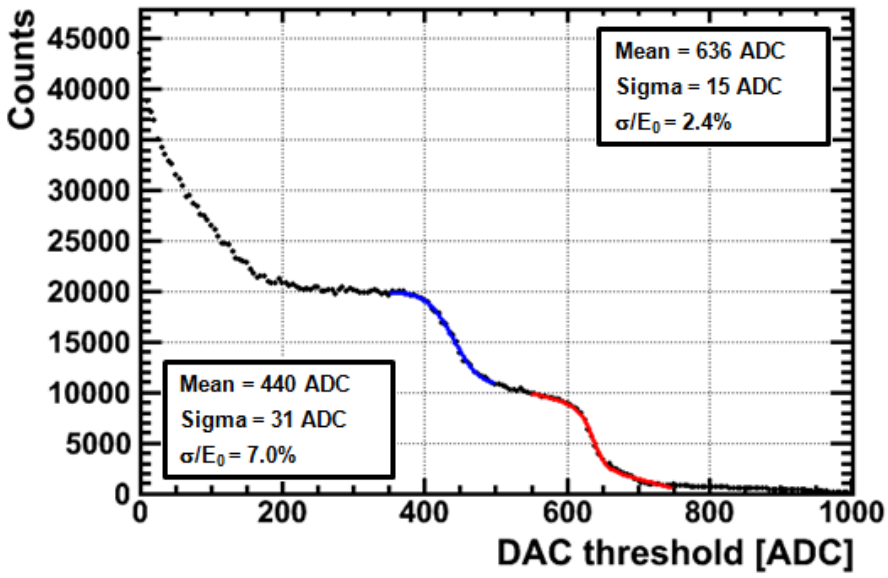

(a)

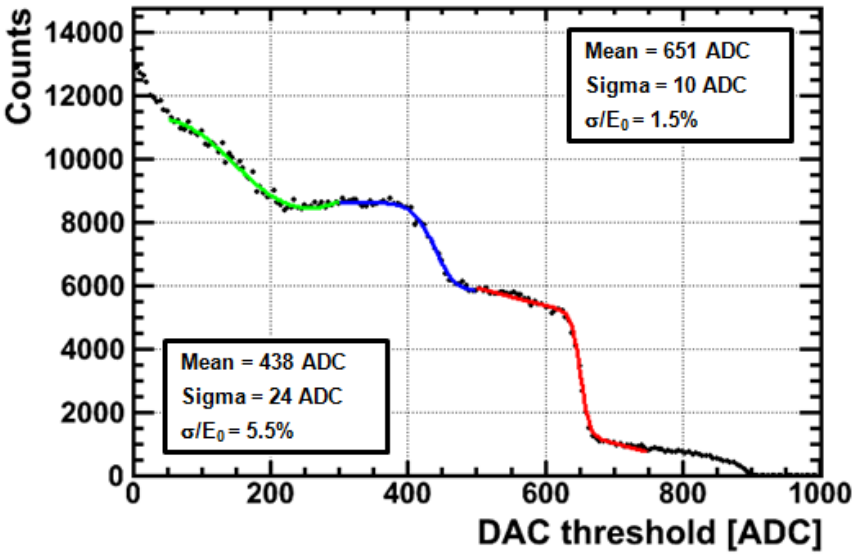

(b)

Figure 4.48: *Cluster charge analysis at 79 keV : (a) 55µm Timepix detector, (b) 110 µm Timepix detector*

Bias voltage variation

The influence of bias voltage on the detector performance was studied at 25 keV for 55 µm and 79 keV for 110 µm detectors in counting mode. Bias voltages between -500 V and -50 V were applied to the detector and approximately 5 minutes was given for the leakage current flow to settle. The DAC threshold of the detector was scanned between the noise level and relevant energy. The S-curve was fitted to the plot and the energy resolution about the peak position was extracted. Figure 4.49 shows a series of DAC scan curves for the 55 µm detector at 25 keV. The relatively large shift in the peak position indicates a significant level of the incomplete charge collection as the bias voltage is decreased. However, the 25 keV peak remains evident at all bias voltages tested except for -50 V. At -50V the reverse bias is not sufficient to create detectable signals above threshold. During this measurement some effects due to pile up was detected. This happens due to large photon fluxes corresponding to an increased probability of pulse spacings shorter than the time needed for the signal to return to baseline. When this happens the previous signal

charge is not fully dissipated so that the charge of the new pulse is added to the remainder of the previous one.

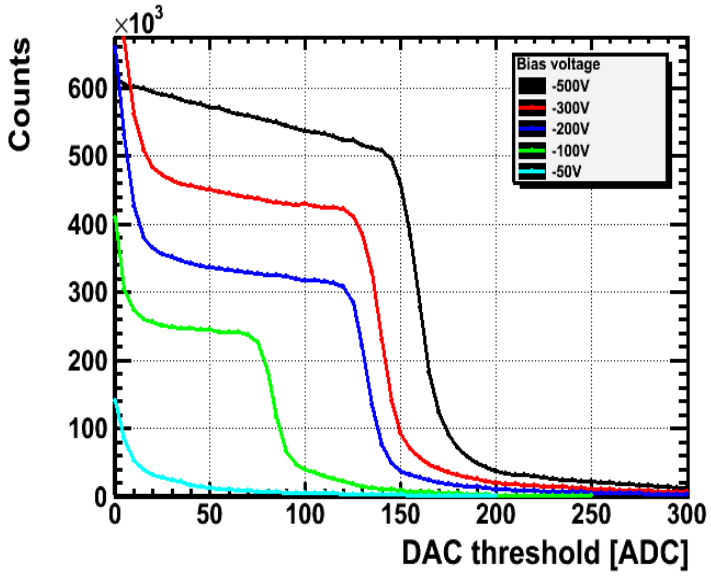

Figure 4.49: *DAC scan with different bias voltage for 55µm CdTe timepix Detector*

Fig. 4.50 shows that -200 V is the optimum voltage setting for good energy resolution for 55 µm CdTe Timepix detector

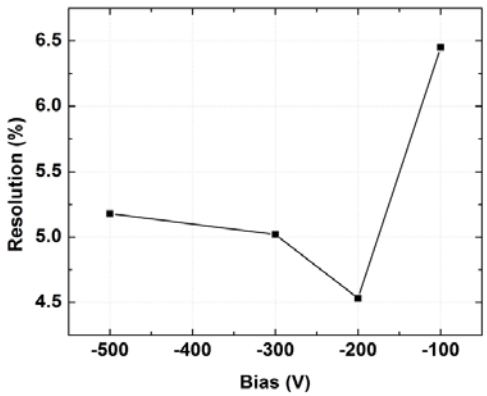

Figure 4.50: *55 µm; Effect of Energy resolution with different bias voltage*

The 110 µm pixel detector was tested at 79 keV. No significant shift in the peak position was observed at various bias voltages (see Fig 4.51). Fig 4.52 shows the energy resolution in different bias voltage for the 110 µm pixel detector. Energy resolution varied

between -100 V and -500 V, reaching a maximum value at -400 V. The analysis shows the best energy resolution achieved is σ/E_o =1.3%..

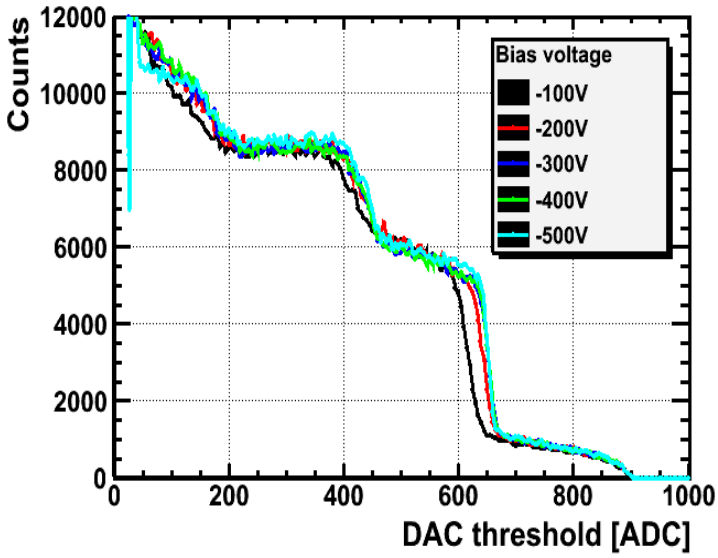

Figure 4.51: *DAC scan with different bias voltage for 110 µm CdTe timepix Detector*

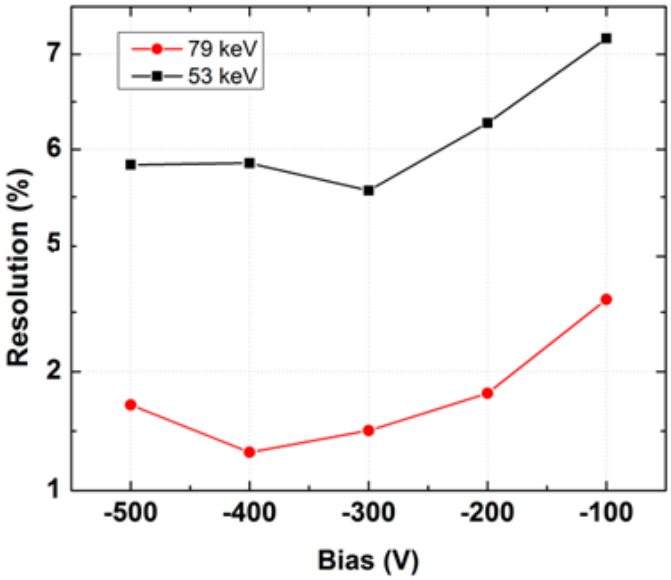

Figure 4.52: *Energy resolution for 79 keV and 53 keV*

Gain variation

In order to optimise the assembly performance, the detector gain was varied, keeping bias voltage at -300 V. Both 55 and 110 µm detectors were scanned with gain, IKRUM, varied between 5 and 100 ADC units. Two corresponding plots are shown in Fig. 4.53 and 4.54. At the higher gain of 5 ADC even though the dynamic range of the sensor is used to the highest extent, double counting becomes noticeable. The highest gain available was tested on the 55 µm detector at 25 keV. The performance of the detector is significantly influenced by double counting. This can be seen in Fig.4.55.

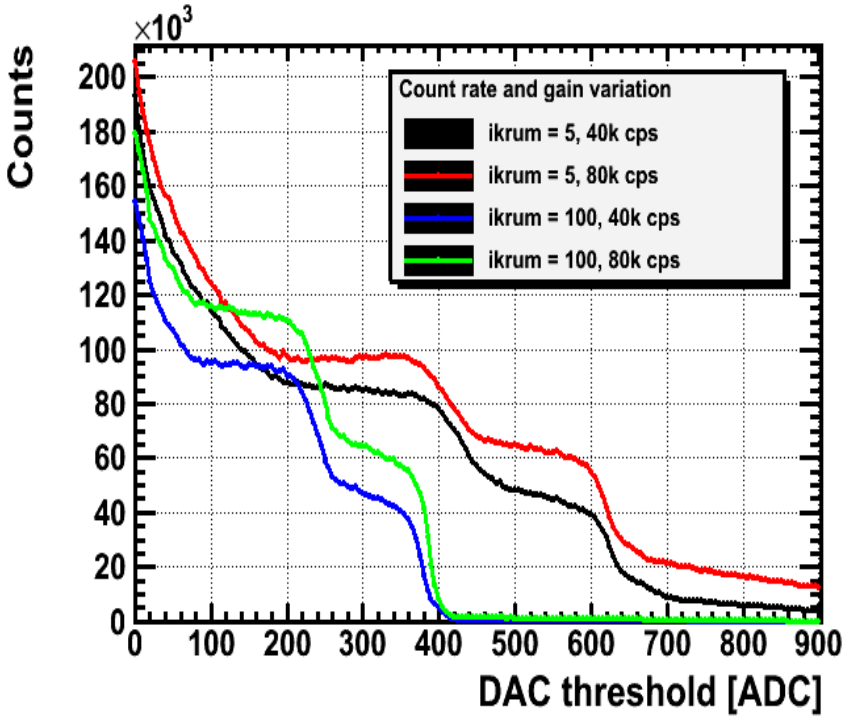

Figure 4.53: *Analysis of gain for 55 µm CdTe Timepix detector.*

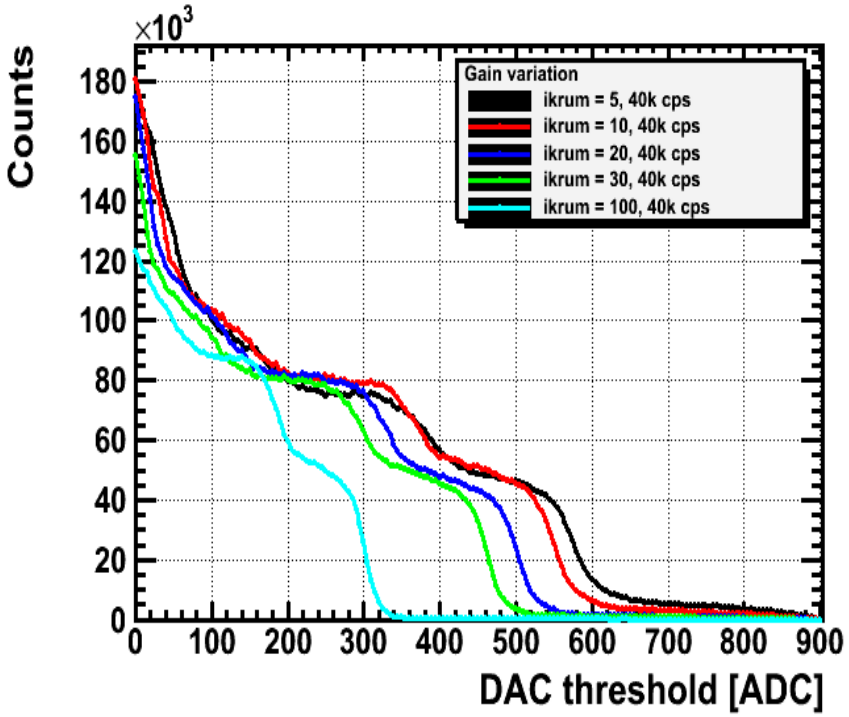

Figure 4.54: *Analysis of gain for 110 µm CdTe Timepix detector.*

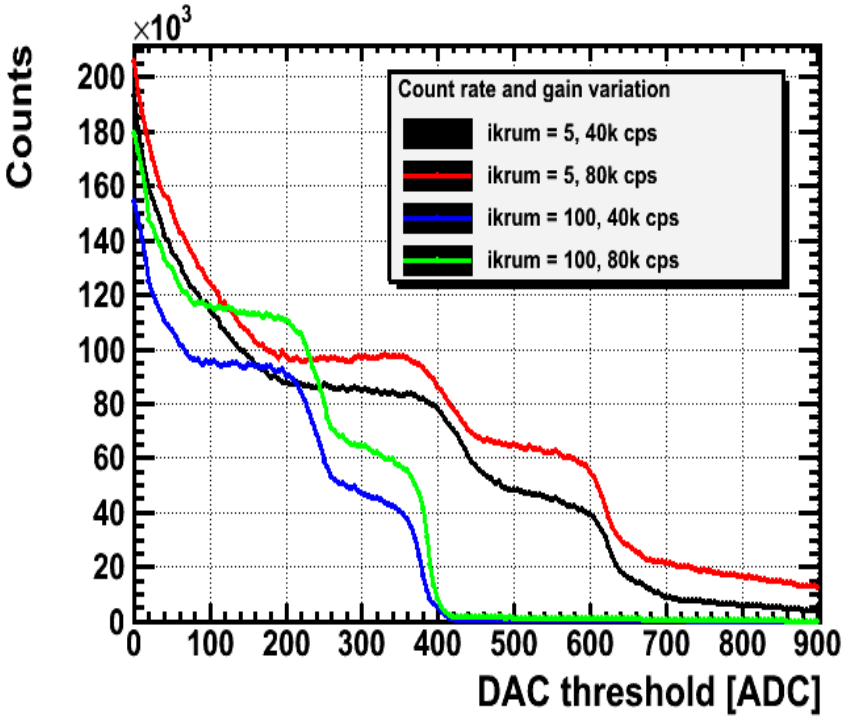

Figure 4.55: *Effect of double counting for 55 µm CdTe Timepix detector*

Count rate studies in counting mode

The performance of both detectors was compared at two count rates of 40 k and 80 k counts per second (cps) per pixel at 79 keV. No significant degradation of energy resolution or baseline shift was observed for the 55 µm pixel detector, while for the 110 µm assembly the peak mean was shifted by 0.25% resulting in an energy resolution degradation of 3.75%. The results are plotted in Fig. 4.56. The results also show that high count rates degrade the measurement at high gain only. The optimal IKrum for best energy resolution seems to be ~ 10.

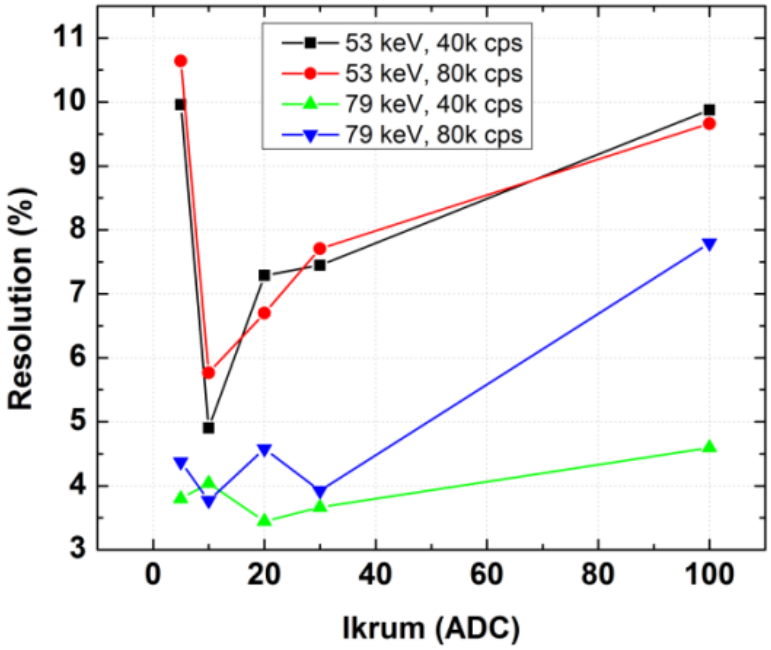

***Figure 4.56**: Energy resolution for 110 µm CdTe Timepix detector in different count rate at 79 keV*

Overall performance of energy spectrum

A combined comparison of the energy resolution between 55µm and 110 µm pixel pitches on γ-ray sources and synchrotron radiation is shown in Fig 4.57. On average the 110 µm pixel detector demonstrates the energy resolution better by a factor of two at energies above ~ 50 keV. Rather poor energy resolution was observed on both detectors for X-ray fluorescence and source energies below ~ 60 keV. This could be associated with non-optimised amplifier settings during the experiment.

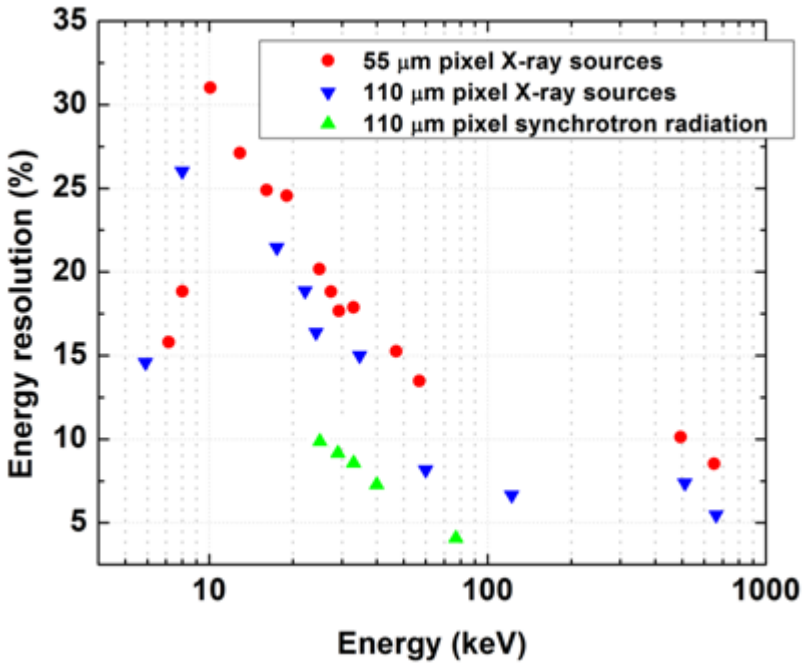

***Figure 4.57**: Energy resolution comparison between 55 µm and 110 µm pixel detectors recorded at Diamond synchrotron and fluorescence/X-ray sources.*

4.7 Material defect studies

The material defect studies were carried out with the 55 x 55 μm *CdTe* Timepix detectors. The measurement was set up using 60 kVp X-ray tube and synchrotron radiation. The images of defects were taken at reverse biases of -50 V, -150 V, -300 V and -500 V using a 60 kVp X-ray tube and are presented in Fig 4.58. The height of images is 14 mm. The results indicate that the visibility of defects is obvious at high bias voltage. On the other hand, the defect in forward bias is shown in Fig 4.59. The bright lines defects are shown in Figs. 4.58 and 4.59. These defects occurred because of the small-angle (sub-) grain boundaries and/or dislocation networks in the crystal [75], [76].

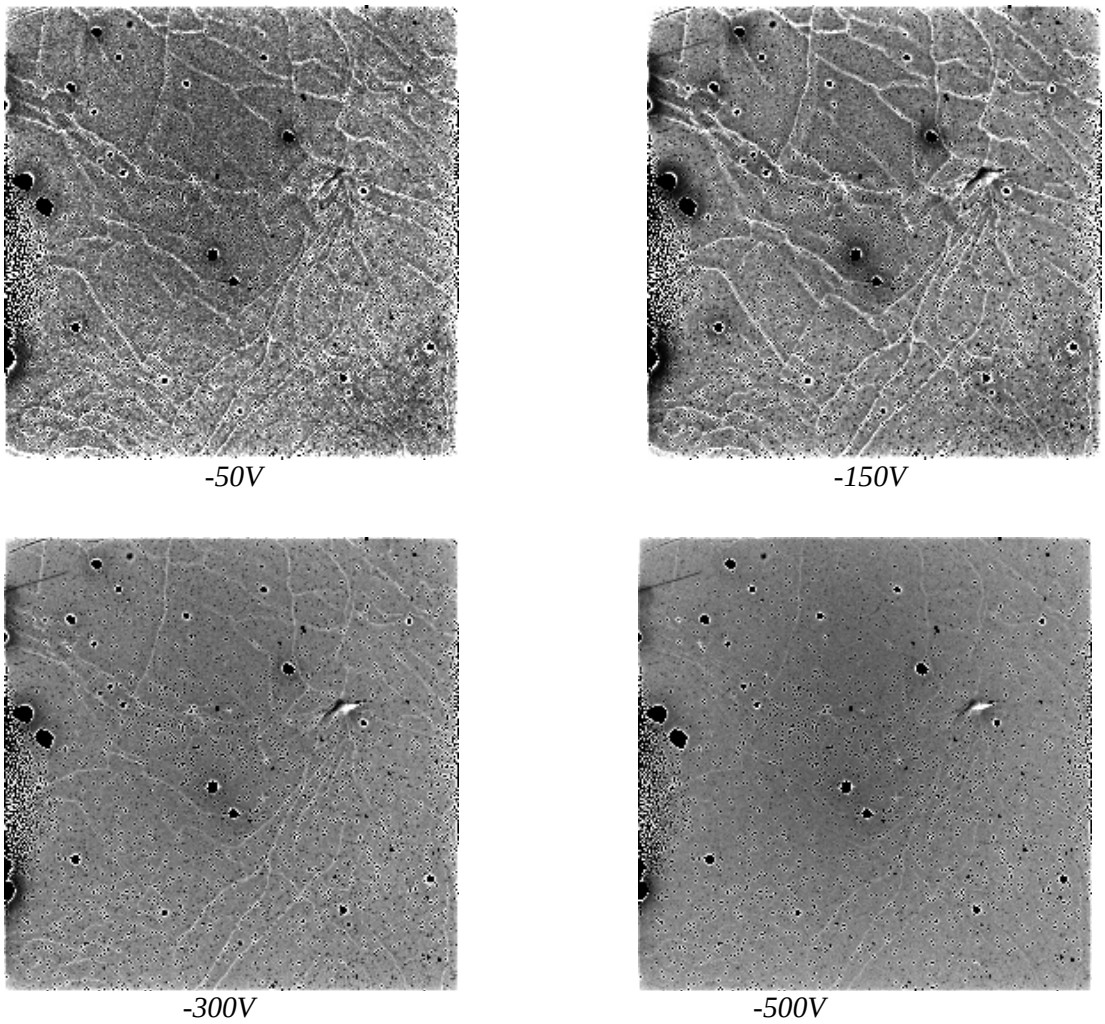

Figure 4.58: *Detect studies at reverse bias.*

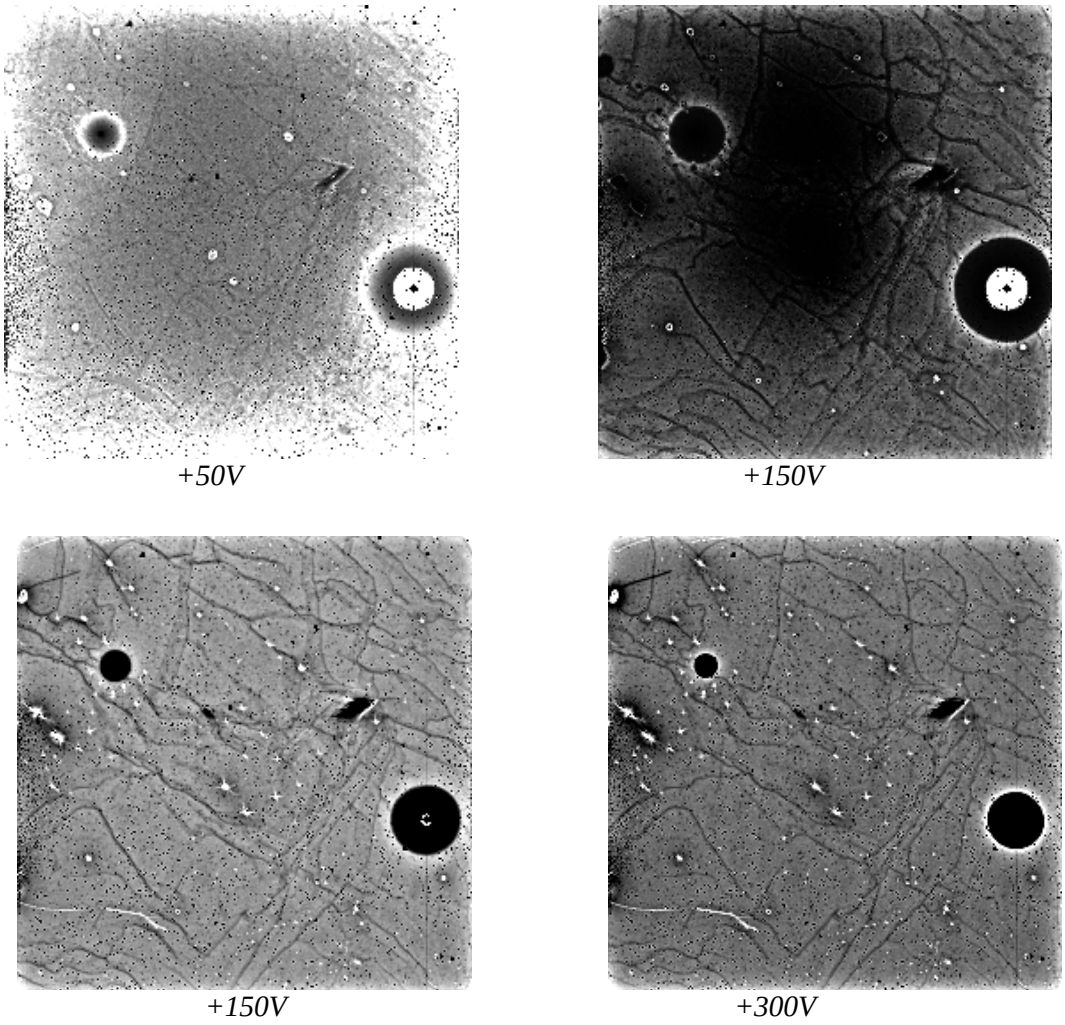

Figure 4.59: *Detect studies at foward bias.*

The sensor displays a strange behavior for the ring defect as shown in Fig 4.59 as it appears in hole collection mode only. A micro focus beam 79 keV inclined at 30 degree to the sensor surface has been used to scan the defect area, both in electron and hole collection mode. There are no traces of the defect in electron collection mode, neither in the sum of all scans (Fig. 4.60) nor in any of the layers at individual depths that can be produced. From the individual scan at positive bias a strong distortion in the electrical field around the defect was encountered. The leakage current in the sensor is considerably higher with positive bias (hole collection) than in electron collection mode. This is due to the current flow through the center of the defect creating the distorted field. The fact that holes flow out from the defect indicates that the potential around the defect is higher than in the surrounding pixels. As a result of a visible line through the defect there is also

evidence that the readout electronics is affected. It is evident that the defect acts like a diode but more investigations are needed to understand the nature of the defect.

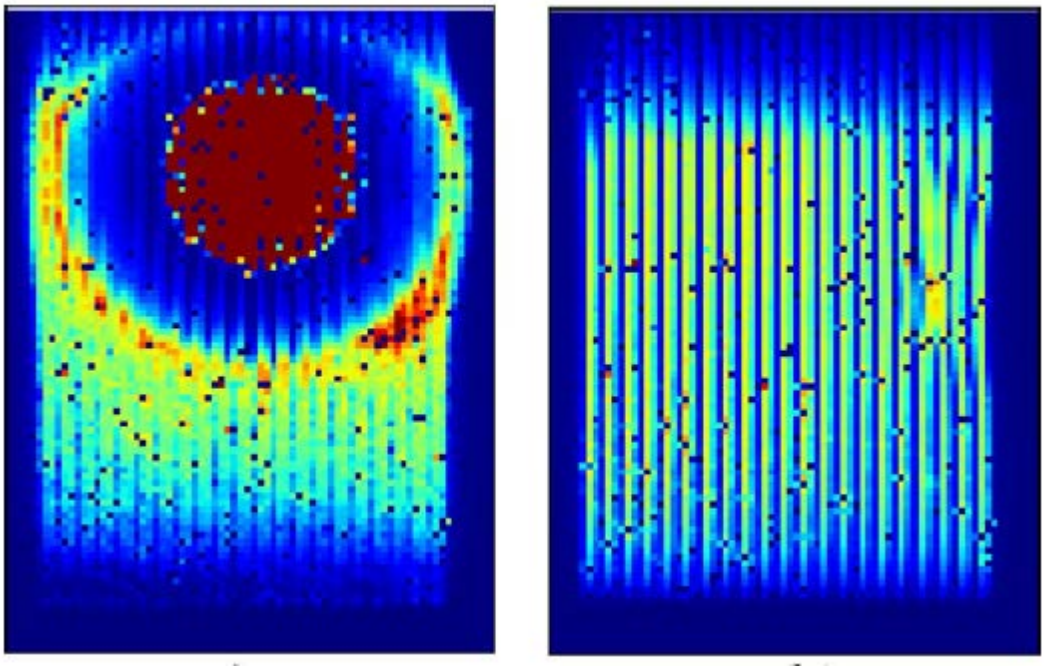

(a) (b)

Figure 4.60: *Sum of all the scan steps in a tilted raster scan over the defect for both positive and negative polarity. The scan was performed at 30^{o} to the sensor surface. The colour scale represents number of counts and red area in the centre on the +100 V scan is due to noisy pixels. (a) +100V, (b) -300 V.*

4.8 Conclusion

Two 1 mm thick CdTe detectors with pixel pitches of 55 μm and 110 μm bump-bonded to the Timepix readout ASIC were characterised by means of spectroscopic energy measurements from a monochromatic X-ray source at Diamond Light Source, various radioactive γ-sources and a laboratory X-ray tube. The imaging performance of the detectors was assessed in terms of modulation transfer function at different spatial frequencies.

The measured mobility lifetime values for electrons and holes for the whole sensor agreed with those previously published. The extracted mean $\mu\tau$ value for electrons from fitting the data was found to be 1.35 ± 0.04 x 10^{-3} cm^2/V and agreed with the previously published value 1.9±0.6 x 10^{-3} cm^2/V [67]. The extracted $\mu\tau$ value for holes is 2.1 ± 0.3 x 10^{-4} cm^2/V. This result is more than twice the previous published one 0.75±0.25 x 10^{-4} cm^2/V [67].

The CdTe detector with 55 μm pitch demonstrates reasonable imaging performance. A 70% contrast at 4 *lp/mm* was achieved for the 55 μm pixel pitch detector with the 60 kVp X-ray tube and 5 keV noise level. No significant degradation in performance was observed for X-ray tube energies of 20 – 60 keV. The optimal bias voltage for imaging was found to be 400–500V for the 1 mm thick CdTe detector. As expected, around half the contrast transfer (30%) was recorded for 110 μm compared to the 55 μm pixel detector at 4 *lp/mm.*

The energy resolution was found to be systematically better for the 110mm pixel detector for the energy ranges 10–1000 keV. At energies above ~1000 keV both detectors demonstrated acceptable spectroscopic performances. For example, the ^{137}Cs 662 keV peak gives $\Delta E/E$ = 8.4% for the 55μm pixel, compared to 5.7% for the 110 μm pixel at -300V bias voltage. The linear relationship between bias voltage and energy resolution was demonstrated for 511 keV γ-rays. The systematic difference in energy resolution between two pixel pitches is associated with pixel-to-pixel non uniform response not only in the ASIC but potentially related to the CdTe material itself. The small pixel size induces an important charge sharing effect which limits the spectroscopic capabilities of the sensor. Charge-sharing is a major drawback in building spectroscopic detectors with such high spatial resolution [77]. This can be improved by post-treatment algorithms based on the summing of signal from several adjacent pixels such as is done with Medipix3. Decreasing the sensor thickness may also be an option to reduce charge sharing.

The results of spectrum analysis also indicate that Counting mode is better than ToT mode by factor around 3-7. The experiment at diamond with energy beam setting at

79 keV shows that the 110 µm CdTe Timepix detector has an energy resolution for counting mode about 1.5% either in clusters or without cluster. Meanwhile, in ToT mode the value is 4.3% without clustering and 7.4% with clustered charge.

In defect studies, bright line defects show sufficient response and stable over time. However, these lines can be corrected with flat field images. Meanwhile, the ring defect is more difficult or impossible to correct.

Chapter 5

Imaging with a *CdTe* Timepix detector

5.0 Introduction

This chapter discusses the application of the *CdTe* Timepix detector to x-ray computed tomography imaging. X-ray Computed Tomography (CT) is a non-destructive technique for visualizing interior features within solid objects, and for obtaining digital information on their 3-D geometries and properties. In the previous chapter the quality of detector performance and energy resolution have been described, showing that the *CdTe* Timepix detector has sufficient performance to enable it to be used for X-ray tomography. Following a brief history of x-ray computed tomography and a description of artifacts and their origins in the reconstruction of the tomogram, the chapter describes the experimental arrangement of a simple x-ray tomography set-up. Finally, there is a discussion about novel techniques used to eliminate the most common artifact effects which arise in the reconstruction. Through the use of these techniques a good quality image can be produced which is will find applications in CT imaging.

5.1 X-ray Computed Tomography

A tomogram is a technical term for a CT image. It is also called a slice because it corresponds to what the object being scanned would look like if it were sliced open along a plane. A CT slice corresponds to a certain thickness of the object being scanned. So, while a typical digital image is composed of pixels, a CT slice image is composed of voxels (volume elements).

Tomographic imaging directs X-rays at an object from multiple orientations and measures the decrease in intensity along a series of linear paths. Beer's Law is applied to characterize the decrease in intensity, as a function of X-ray energy, path length, and material linear attenuation coefficient [78]. A specialized algorithm is then used to reconstruct the distribution of X-ray attenuation in the volume being imaged.

The simplest form of Beer's Law for a monochromatic X-ray beam through a homogeneous material is [79]:

$$I = I_o exp[-\mu x] \quad 5.0$$

where I_0 and I are the initial and final X-ray intensity, μ is the material's linear attenuation coefficient (units 1/length) and x is the length of the X-ray path. If there are multiple materials, the equation becomes:

$$I = I_o exp[\sum_i(-\mu_i x_i)] \quad 5.1$$

where each increment i reflects a single material with attenuation coefficient μ_i with linear extent x_i. This equation can be solved directly with a well-calibrated system using a monochromatic X-ray source (i.e. Synchrotron, or gamma-ray emitter). If a polychromatic

X-ray source is used the complete solution would require solving the equation over the range of the X-ray energy (*E*) spectrum utilized. However, this has to take into account the fact that the attenuation coefficient is a strong function of X-ray energy,

$$I = \int I_o(E) exp[\sum_i (-\mu_i(E) x_i)]\, dE \qquad 5.2$$

The solution to such a calculation is usually problematic, as most reconstruction strategies, solve for a single μ value at each spatial position. In such cases, μ is taken as an effective linear attenuation coefficient, rather than an absolute. As the effective attenuation is a function of both the X-ray spectrum and the properties of the scan object, this complicates absolute calibration. It also leads to beam-hardening artifacts: changes in image gray levels caused by preferential attenuation of low-energy X-rays.

A number of methods image reconstruction by which the X-ray attenuation data can be converted into a tomography image have been produced by researchers [80]. In this work Ramp filter in "filtered back projection" has been applied, where the linear data acquired at each angular orientation are convolved with a specially designed filter and then back projected across a pixel field at the same angle. The source code for image reconstruction developed in this project shown in Appendix C.

In the case of X-ray tomography, similar to X-ray radiography, the quantity being imaged is the distribution of the attenuation coefficient $\mu(x)$ within the object of interest. The different is only the technique to produce the tomogram where the X-ray radiography the image can produce staright foward after exposed to x-ray. Meanwhile tomography produces by combination of image in radiography in every angle projection. Fig. 5.1 shows the image X-ray radiography of a pencil and also computed tomography image taken using the CdTe Timepix detector.

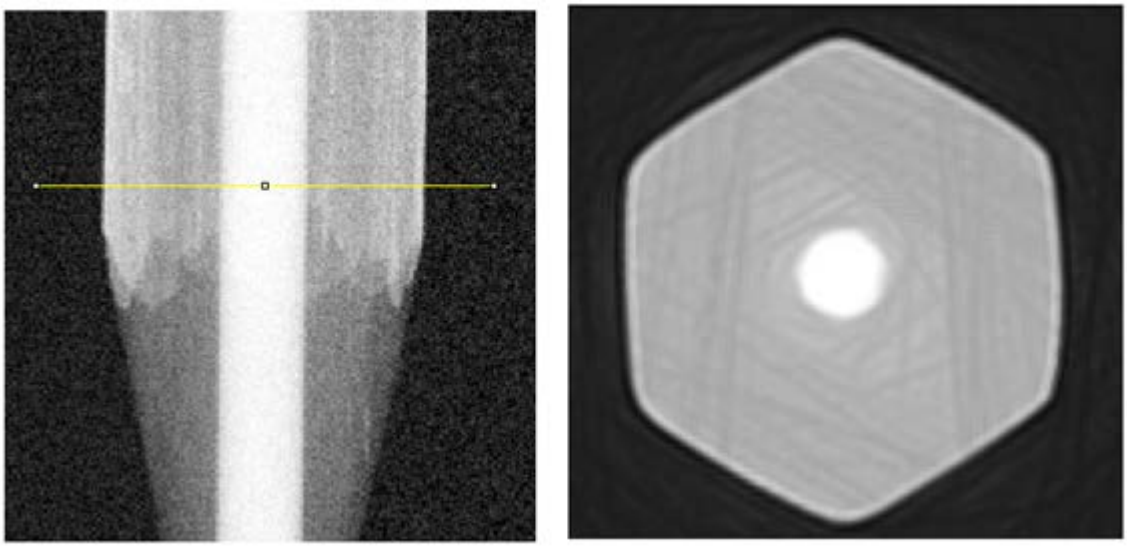

(a) Line image of a pencil *(b) Tomogram image of a pencil at yellow line in (a)*

***Figure 5.1**: Images taken by the CdTe Timepix detector*

5.2 Artifacts in X-ray CT

In this section, various sources of artifacts in X-ray CT images will be briefly reviewed. In computed tomography, the term artifact is applied to any systematic discrepancy between the CT numbers in the reconstructed image and the true attenuation coefficients of the object. CT images are inherently more prone to artifacts than conventional radiographs because the image is reconstructed from something on the order of a million independent detector measurements. The reconstruction technique assumes that all these measurements are consistent, so any error of measurement will usually reflect itself as an error in the reconstructed image. This chapter also looks at the novel use of the CdTe Timepix detector to prevent and eliminate artifacts which normally occur in the tomogram.

5.2.1 Beam Hardening.

Typical X-ray tube spectra are polychromatic, where an x-ray beam is composed of individual photons with a range of energies. Consequently, the beam traversing through an object will become “harder”. It is because of the energy being increased by the preferential absorption of the low energy photons [81] as the low energy photons have a larger interaction cross-section than the high-energy photons. This situation is as known as beam hardening artifact.

The presence of metal objects in the scan field can lead to severe streaking artifacts [82]-[84]. Fig. 5.2 shows the effect of a beam hardening artifact with streaking patterns.

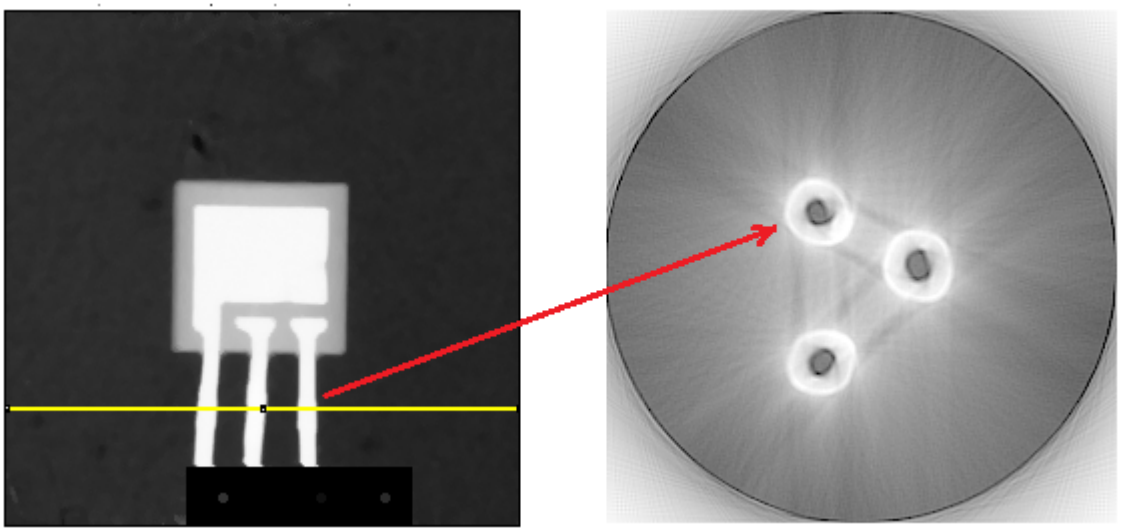

Figure 5.2: *Beam hardening effect with streaking patterns taken with the CdTe Timepix detector.*

5.2.2 Ring Artifacts

When the position in the alignment of x-ray tube, object and detectors is not well calibrated, the ring type of artifact appears [81]. The detector will give a consistently erroneous reading at each angular position, resulting in a circular/ring artifacts [85]. An imperfect data collection from the pixel detector can also cause a ring artifact where the causes for the incorrect pixel response are manifold. These variations are observed in the reconstructed images showing concentric rings which are superimposed on the reconstructed image. Fig 5.3 shows a tomogram with ring artifacts caused by imperfect data collection.

To diminish the effects of false pixel responses different pre- and post-processing ring artifact correction algorithms were developed. Nevertheless, pre-processing algorithms based on flat-field corrections, moving detector arrays during acquisition and sinogram processing still do not remove ring artifacts to a sufficient degree [86], [87]. In this research, a new algorithm has been developed to use an image projection along a line for the image reconstruction to eliminate the ring artifact.

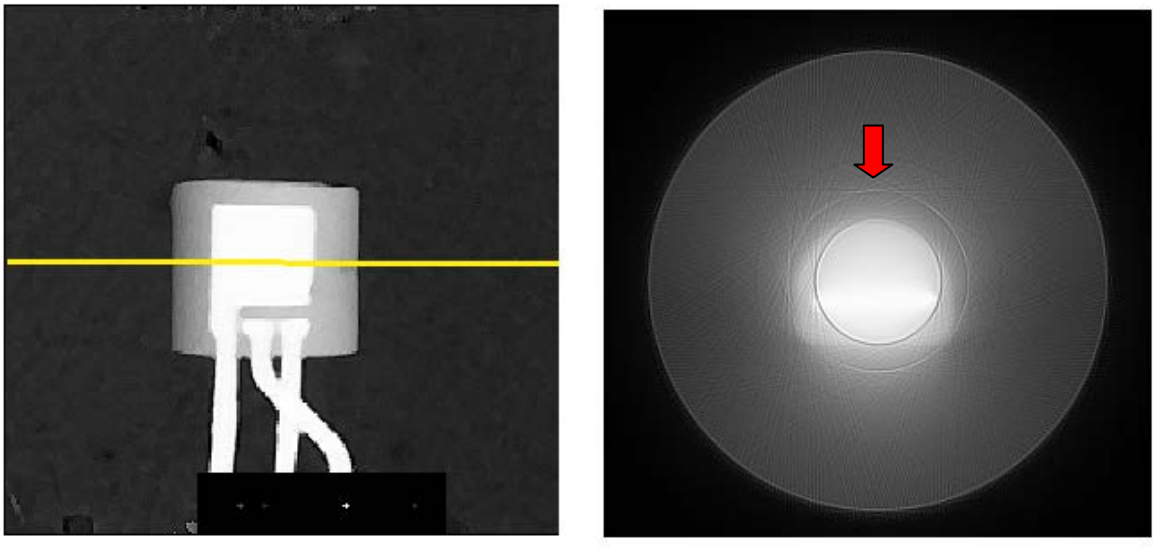

a) Line image *b) Tomogram*

Figure 5.3: *Ring artifact*

5.2.3 Noise.

The data projection measured with CT scanners contains noise originating from two main sources:

- The quantum noise inherent to X-ray generation and detection.

- Noise due to detection processes: the dead pixel, glowing pixel, electronic noise in the detector and the data acquisition system.

The number of quanta of a given X-ray energy measured by a CT detector cell obeys a Poisson distribution. Since photons corresponding to different energies are integrated during the detection, the noise in the total recorded signal follows a compound Poisson distribution [88], [89]. Nevertheless, the basic property of the Poisson-like distributions is conserved: the larger the mean value of the signal, the larger the signal-to-noise ratio. The relative noise contribution is therefore stronger for projection lines crossing highly attenuating or large structures.

The noise present in the projection data obviously propagates into the reconstructed images. One of the consequences of this is the reduction in the detection ability for low-contrast structures; they may become almost completely obscured by the noise. When, excessive noise is encountered in the projection data due to the presence of highly attenuating structures or the large size of the object being scanned, the non-linearity of the logarithm may lead to noise-induced streaks in the reconstructions. Such an artifact is visible around the metallic implant that can be seen in Fig. 5.3. In order to address such issues, the noise in the projection should be kept to a minimum. This can be achieved by increasing the scanning time or the intensity of the radiation [88]. In these studies this has been done to overcome this issue by using the removed outliers filter which has been created in a software routine.

5.3 Experimental setup industrial X-ray tomography

The experiment setup is based on a setup for cone beam projection tomography. The X-ray generator and detector are fixed and the sample/object is rotated. The minimum interval rotation is 1 degree. Fig. 5.4 shows the setup of a low cost x-ray tomography apparatus. The setup consists of the following principal components:

- Mini-X-ray Tube 50kVp (120^{o} cone beam, 2mm focal spot size) [90]
- Rotating stepper motor and position control [91]
- CdTe Timepix detector.

In this work, two types of samples have been studied with different mass attenuation coefficients. The first sample is a pencil, which consists of a layer of paint coating (outside layer of the pencil), wood and carbon. The pencil has been chosen so that studies of image reconstruction using the different density profile can be conducted. While for the second sample a voltage regulator has been chosen which contains a bulk of polypropylene and aluminium metal. This sample has been chosen to study the effect of the presence of metal on artifact generation and also on beam hardening.

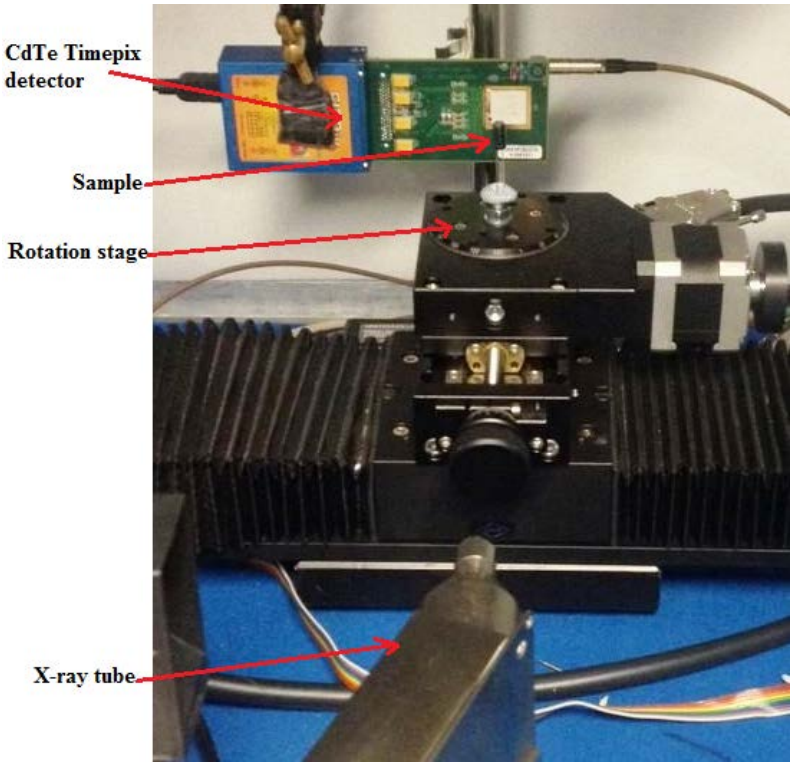

Figure 5.4: *Industrial X-ray tomography setup*

5.4 Result and discussion

The imaging techniques used for this work involved the use and development of both hardware and software parts. Both of these need to be optimised and taken into consideration when performing the image reconstruction. On the hardware side there is the alignment and distance between x-ray tube, sample and detector. In addition a collimated beam should be used in order to reduce beam hardening and background scattering. For the software part there is the flat field correction, noise filtering and arrangement of data projections. ImageJ software has been used to produce the tomographic images using the filtered back projection algorithm (Appendix C). This software enables fast processing of the data to reconstruct the entire image and produce the tomogram.

Hardware part

The optimisation of distance between the x-ray tube and sample is critically important. The distance between x-ray tube and object is set in order to obtain a focused image from the x-ray tube and obtain the best quality image. The closer the x-ray tube is to the sample, the greater the beam hardening artifact effects that become apparent in the reconstructed image. To get an optimal image the CdTe Timepix detector is placed as close as possible to the sample and the centered on the tube-sample-detector axis. Increasing the separation of the detector from the sample gives a magnified projection. The further the sample is from the tube the smaller the image will be. Fig. 5.5 shows the schematic arrangement of an X-ray CT system where Fig. 5.5 (a) show the distance between x-ray tube and detector is around 14 cm and for Fig.5.5 (b) is around 28 cm. The resultant image is shown in Fig 5.6 (a) for a 14 cm separation between tube and sample and Fig. 5.6 (b) for a separation of 28 cm. The image in Fig 5.6 (a) shows the blurring and the beam hardening effect. However, when the distance of the sample is increased a better quality of the image is produced (Fig. 5.6 (b)).

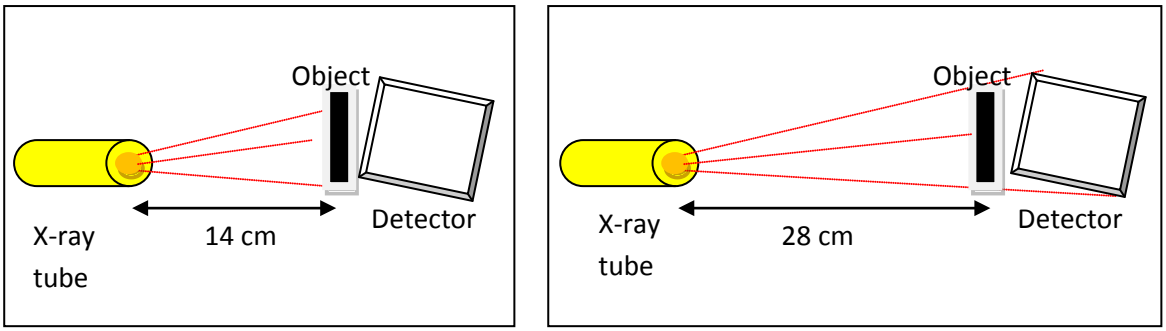

Figure 5.5: *Schematic setup of the CT arrangement. (a) The distance between tube and sample is around 14cm (b) The distance is around 28cm.*

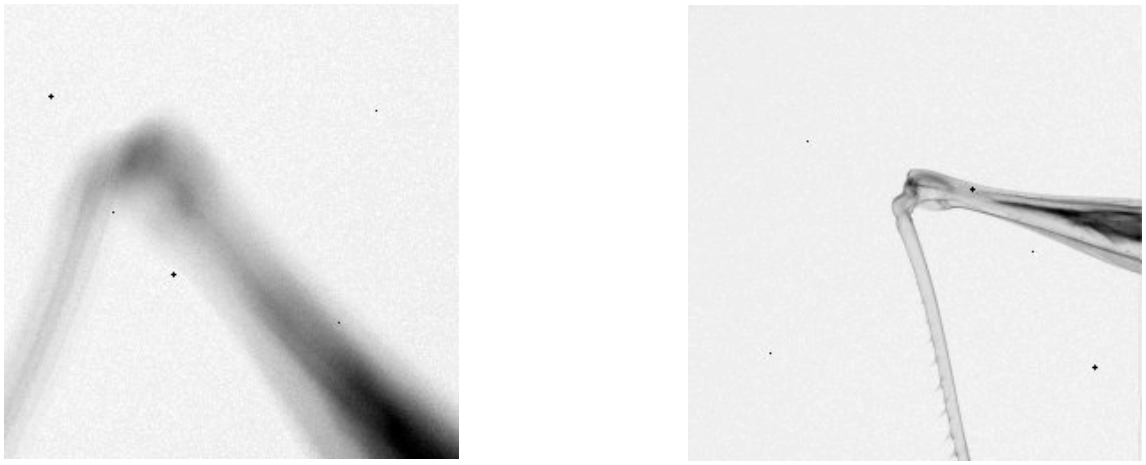

(a) *(b)*

Figure 5.6: *(a) The lower seperation of x-ray tube with sample is seen to produce blur and shows the beam hardening effect. (b) Optimising the separation produces an image of much higher quality*

A collimator is applied to the beam in order to reduce the scattered background effect and beam hardening. A collimator slit is placed in front of the cone beam x-ray tube so that only the photons travelling along a straight line into the region of interest are incident on the sample. Fig. 5.7 shows an image of an insect after the collimated beam has been applied. The image shows that the scattered effect and beam hardening artifact were greatly reduced and produce good quality images.

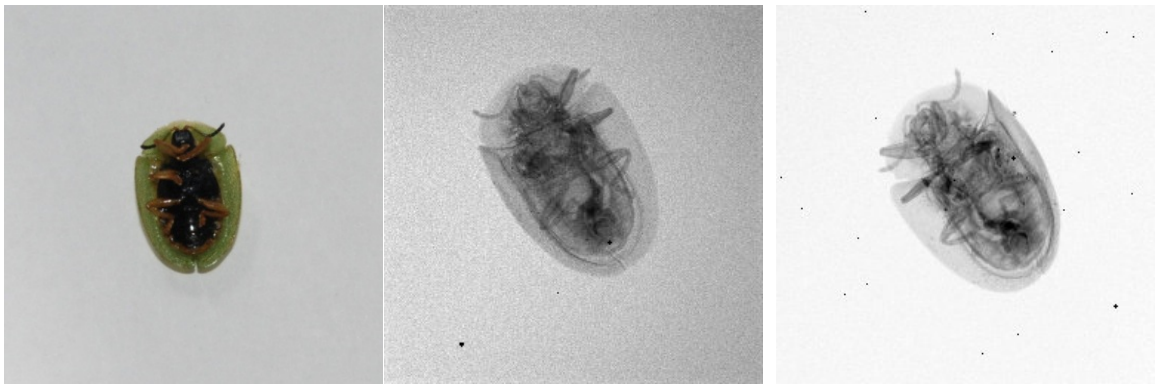

(a) Photographic image *(b) Without collimator* *(c) After collimator*

Figure 5.7: *Image of insect after application of a collimated beam.*

Software part

The software manipulation has three principal adjustment components that are carried out before performing image reconstruction. Firstly a flat field correction is applied to normalize the pixel response across the array in terms of intensity and energy of the polychromatic x-ray beam. The second adjustment applies a noise filter to remove the noise of dead and glowing pixels. The last part arranges the data projection to perform the tomogram.

Flat field correction.

Before the tomography imaging system can be used, the system must be normalized to compensate for non-uniformities in the individual pixels and in the readout chip. This happens due to variations in the sensor layer and the electronics readout threshold equalization [92] of the detector rendering it necessary to minimize differences in the energy response of the detector pixels across the array. Furthermore, as the counting rates of the pixels may vary due to detector inhomogeneities and variations in electronic gain and due to variations in the X-ray beam, a flat field correction is necessary to match the counting-rates of all pixels under X-ray radiation in order to achieve a flat pixel efficiency map leading to a homogeneous image [92]. These normalizations must consider the real operation of the system in order to produce a meaningful correction matrix.

A flat field measurement consists of two simple measurements. One image acquisition has to be made with detector irradiation (bright field) to achieve an effective pixel gain map. In addition, another acquisition has to be performed without irradiation (dark field) to realise a measure of the dark current for each pixel. For photon counting detectors that are used above their noise edge, which is usually true for X-ray imaging applications, the dark field measurement is not necessary because no hits are recorded due to dark current. The setup of the detector and also of the remaining measurement system must be identical for the flat field measurement and the object measured. A homogenous

object with roughly the same attenuation as the measurement object should be used for the flat field measurement. This is due to the beam hardening correlated variances in the pixel gain map caused by the X-ray attenuation of the object. For objects with widely different attenuations some more advanced flat field measurements have to be performed to calculate the beam hardening [93]. After taking the object image and the flat field measurement, the object measurement has to be divided by the flat field measurement to achieve the flat field corrected image [92];

$$I_{ffc} = \frac{I_s}{I_{ff}} \mu_{ff} \tag{5.1}$$

where I_{ffc} is the image with flat field correction, I_s is the image sample, I_{ff} is the flat field image and μ_{ff} is the average flat field signal. The number of flat field measurements taken in X-ray imaging applications to maximize the SNR normally exceeds the number of object measurements by far [94]. Fig. 5.8 shows the image of the flat field correction.

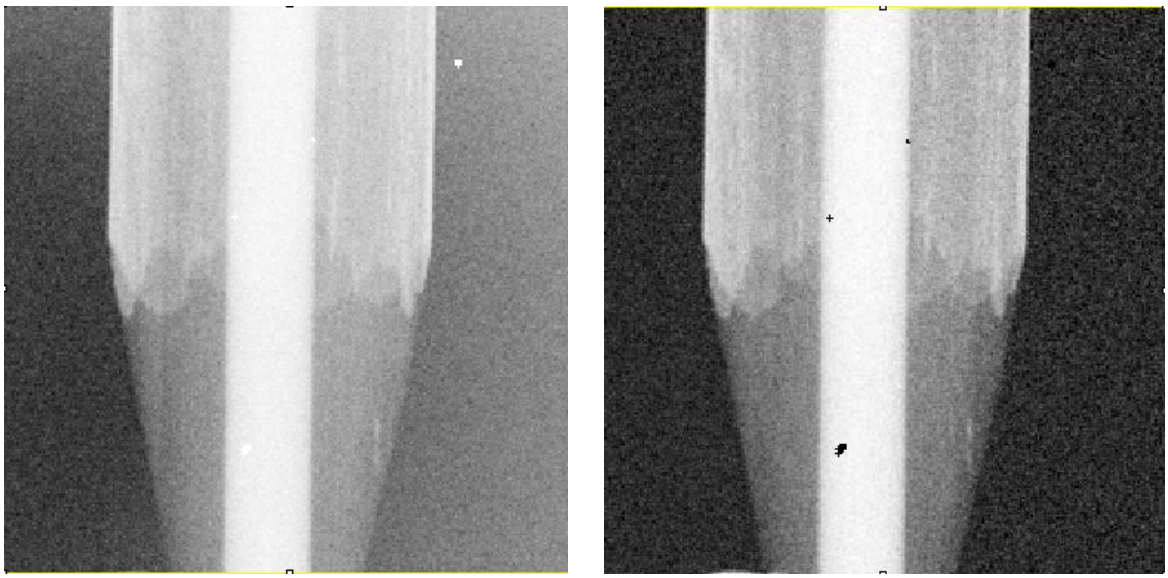

(a) Without flat field correction *(b) Flat field correction*

Figure 5.8: *Flat field correction technique.*

Fig. 5.9 shows the profile of images in Fig. 5.8. The results show that the flat field correction, image is capable of reducing the noise background of the image and making the image sharper. The signal to noise ratio (SNR) for the flat field corrected image is 187. Meanwhile, for image without flat field correction the SNR is 5.26. These measurements indicate that the flat field correction increases the image performance to produce quality images.

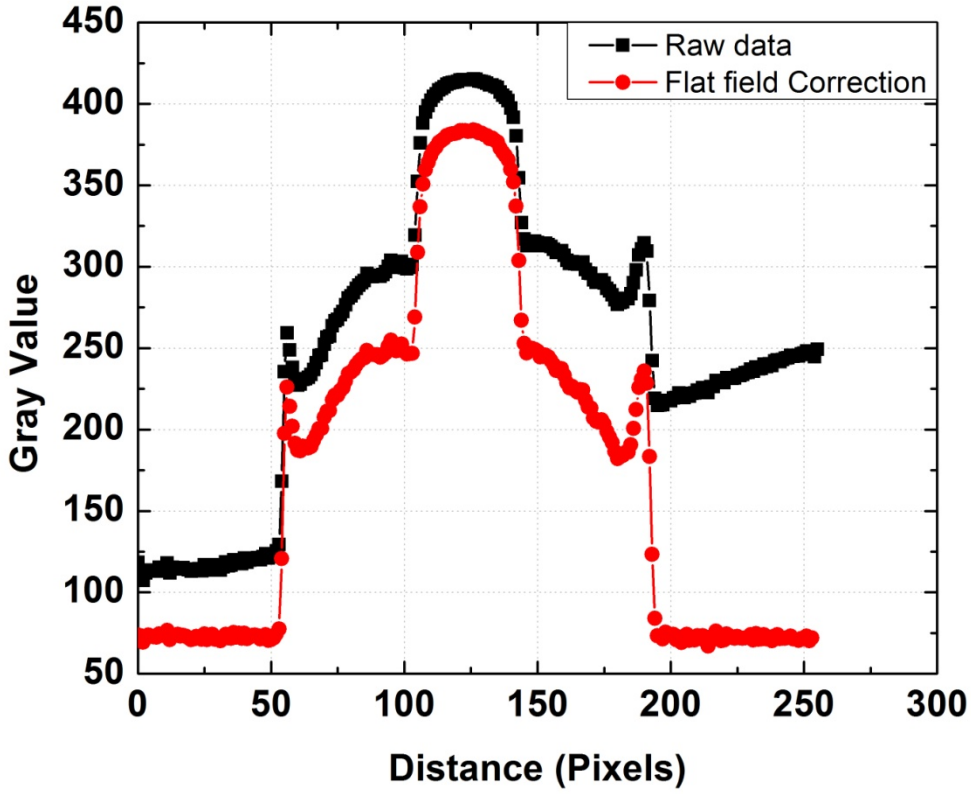

Figure 5.9: *Projection into X-axis profile.*

Noise Filter

The next step after performing the flat field correction, is to apply a "*remove outlier*" algorithm to the image. The "*remove outlier"* algorithm eliminates the noise from dead and glowing (hot) pixels where contributes to produce ring artifact. Fig. 5.10 shows the graphic user interface for this filter. This algorithm works by replacing a noisy pixel by the median

of the value of the surrounding pixels, if it deviates from the median by more than a certain value (the threshold). The "*Radius*" function is to establish the area in pixels used for calculating the median. The, "*Threshold"* function is a measure of how much the pixel must deviate from the median to be replaced. The which "*outlier"* function determines whether the pixel that should be replaced is brighter or darker than its surrounding colleagues.

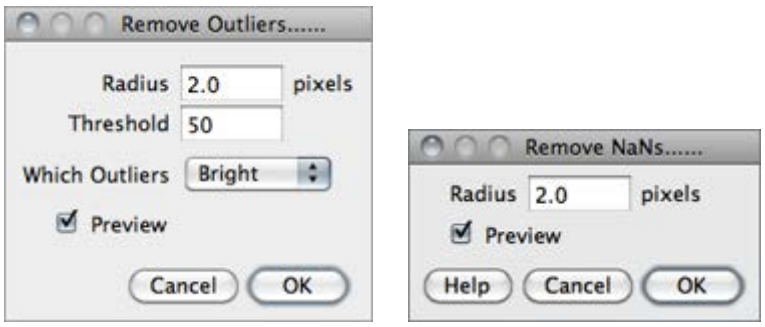

Figure 5.10: *Noise filter interface.*

Remove NaN (Not-a-Number) or dead pixels is a function implemented to replace NaN pixels in 32-bit images by the median of the neighbours inside the circular kernel area defined by "*Radius"*. This algorithm does not remove patches of NaNs larger than the kernel size. Fig. 5.11 shows the resultant image after applying the noise filter. Fig. 5.12 shows a comparison of the image profiles before and after applying the filter. From the profile it shows that the noise (dark and glowing pixels) is further (slightly) reduced compared to the flat field correction profile.

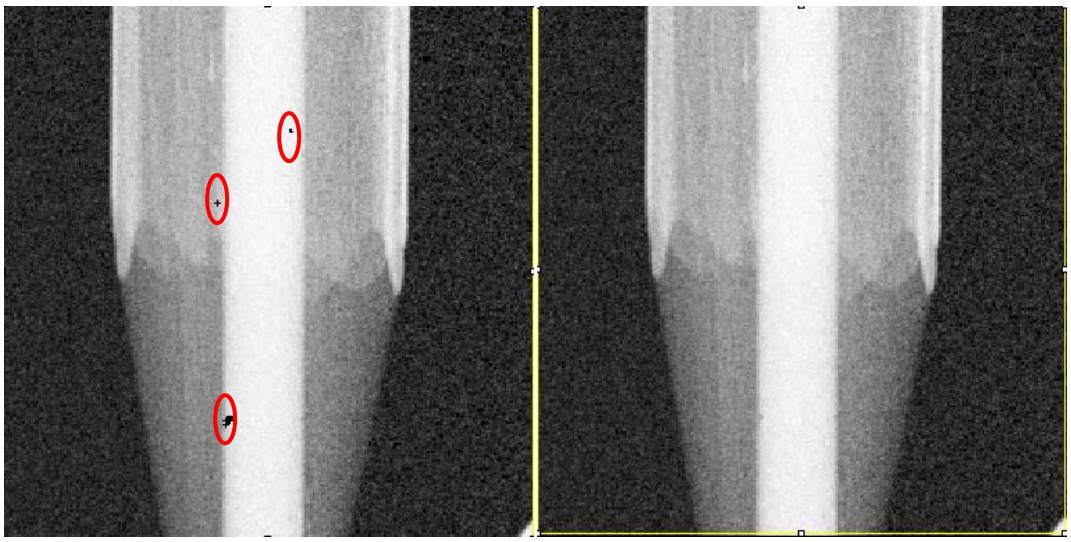

(a) Without noise filter *(b) Noise filter*

Figure 5.11: *Comparison images of pencil before and after performing Noise filter.*

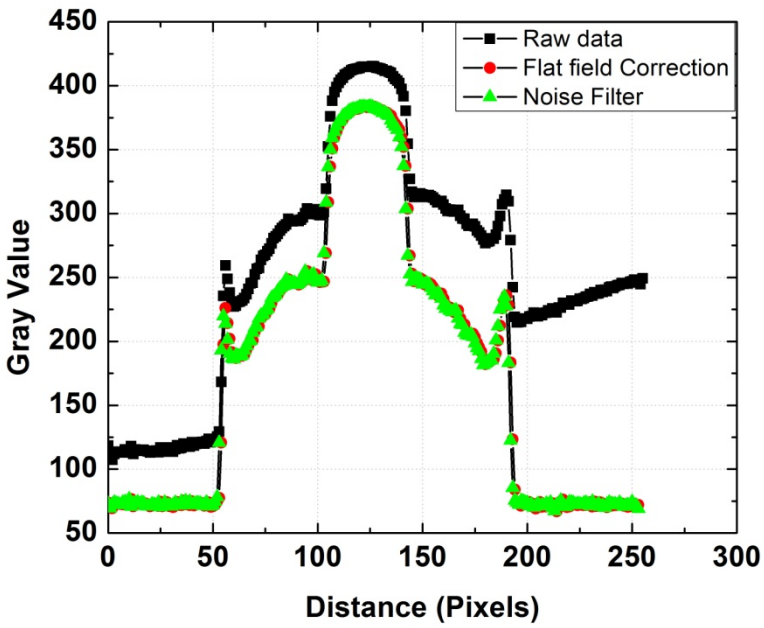

Figure 5.12: *Profile of Pencil image after each process.*

Data projection algorithm

A data projection algorithm was developed to produce high quality image in tomographic reconstruction. The image sets in each projection (0^o to 360^o) are called stacks. A data projection algorithm is a method of analyzing a stack by applying different projection methods to the pixels within the stack. In this study different projection types have been studied, such as *sum slice, average intensity, standard deviation,* and *min intensity* projection method.

A *sum slice* projection creates a real image that is the sum of the slices in the stack. Meanwhile, *average intensity* is when the projection outputs an image wherein each pixel stores average intensity over all images in stack at corresponding pixel location. Another method is a *standard deviation* projection, which functions to produce a real image containing the standard deviation of the slices. The final method being studied is a *minimun intensity* projection. This method creates an output image each of whose pixels contains the minimum value over all images in the stack at the particular pixel location.

Table 5.0 shows the images resulting from different projection types. From the result, it is observed that the *min intensity* method produces a higher quality image compared to the other projection. The *standard deviation, sum slice,* and *average intensity* projection methods all produce tomograms that show a glowing effect at the edge of the wood and carbon (center). The measurement of the profile of *min intensity* tomogram is shown in Table 5.1. The result shows that the size of the pencil in tomogram is similar to the measurement taken using a calliper. From the profile it is observed that the size of the coating outside the layer of the pencil and the carbon inside the pencil can be verified and thus be measured.

Table 5.0: *Results of tomogram in different projection methods*

Photograph of an object 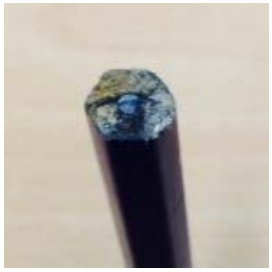	
Type of Data projection	**Result of Tomogram**
1. Sum slice	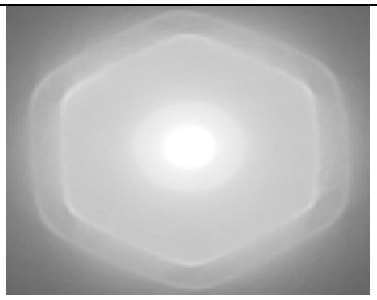
2. Average Intensity	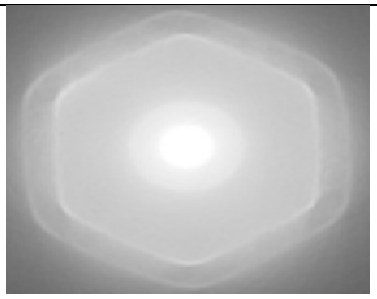
3. Standard deviation	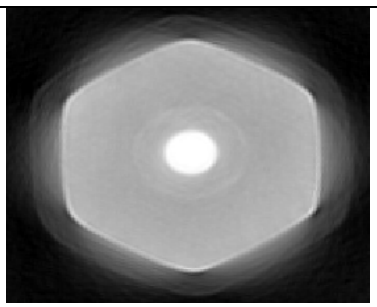
4.Min Intensity	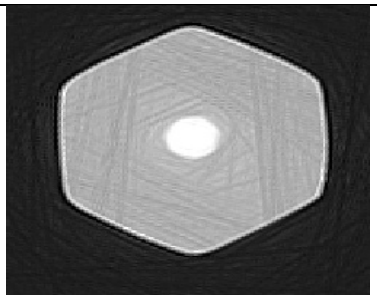

In this study the 3D Slicer platform software has been applied to visualize and analyse the three dimensional images. This software is free online, user friendly and useful for facilitating research into volumetric studies [95]. The slicer has a modular structure so that users can select the functions they need and users also can develop their own modules. Table 5.2 shows the 3 projections of a sample pencil using this volume rendering. The resultant display contains all of the information about the samples. The 3D image of the pencil is generated by combining all of the tomogram images. The gray levels in a CT slice image correspond to X-ray attenuation, which reflects the proportion of X-rays scattered or absorbed as they pass through each voxel in the sample. X-ray attenuation is primarily a function of X-ray energy and the density and composition of the material being imaged [96].

Table 5.1: *Size of pencil measurement*

	Measurement size of pencil
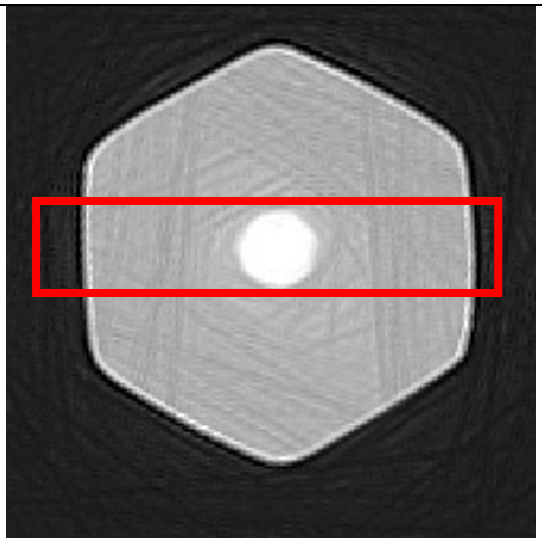	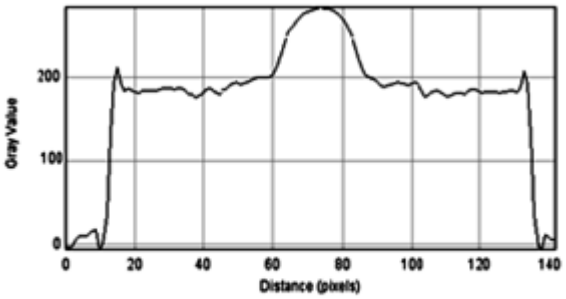 Reading from graph: =(138 -10) pixel x 55um **=(7.04±0.02) mm**

	Reading from calliper = **(7.06±0.02) mm**

Image (a), (b) and (c) show the composition of the density profile of a pencil (paint coating, wooden layer and carbon). The software for the volume rendering is capable of verifying the density profile of the object. When the contrast of the threshold of the image is increased, the wooden area disappears, leaving only the image profiles of the paint coating and carbon (images (d), (e) and (f). This is because the density of carbon and paint coating is higher than that of the wooden layer. Lastly, as the contrast is higher after the threshold (paint coating), only the image of the carbon of the sample pencil can be seen (images (g), (h), (i)).

Table 5.2: *3D images of pencil*

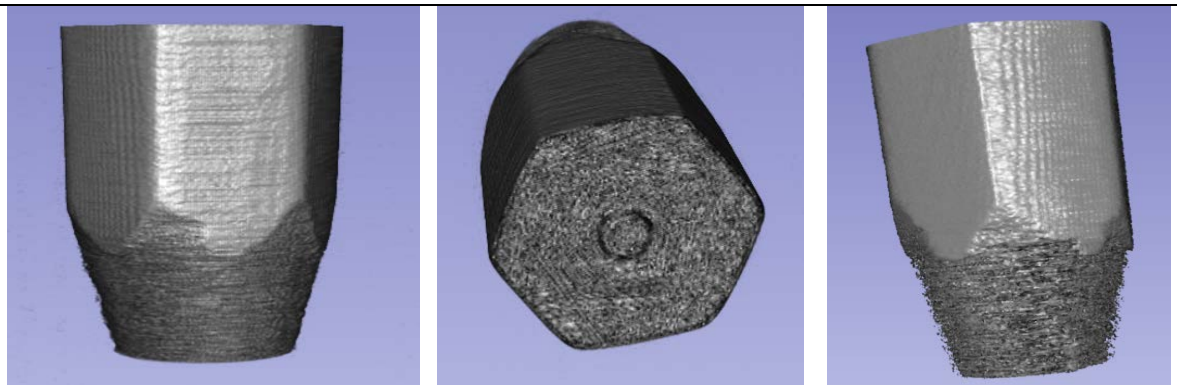

(a) *(b)* *(c)*

3D image of pencil (combination of the slice images) containt of 3 density profile (paint coating, wooden and carbon)

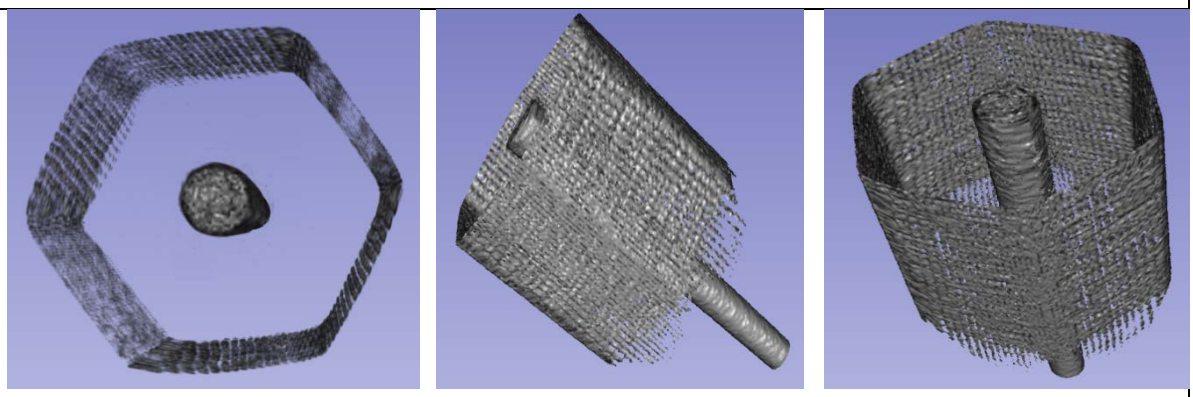

(d) *(e)* *(f)*

3D images of paint coating and carbon

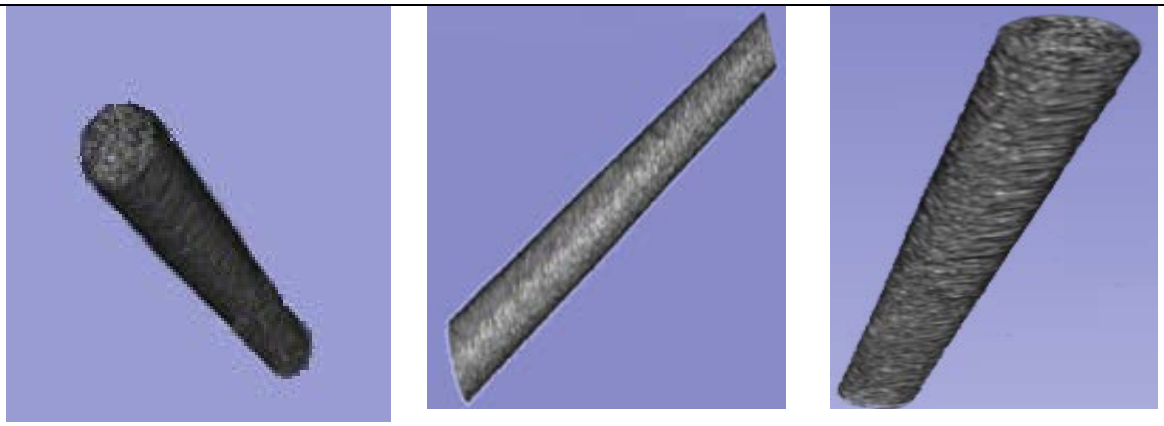

(g) *(h)* *(i)*

3D images of carbon only.

Table 5.3: *Results of voltage regulator*

	Line images	Tomogram
(a)	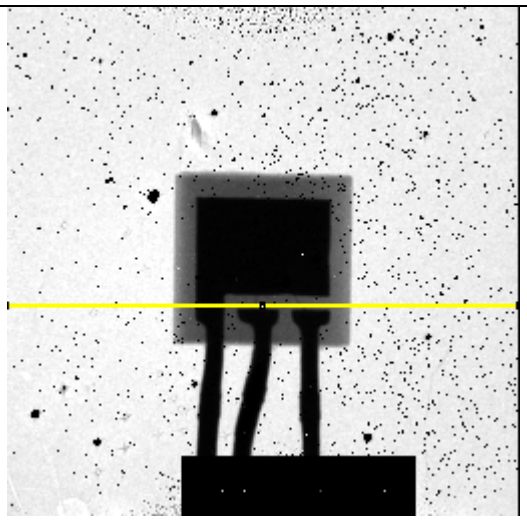	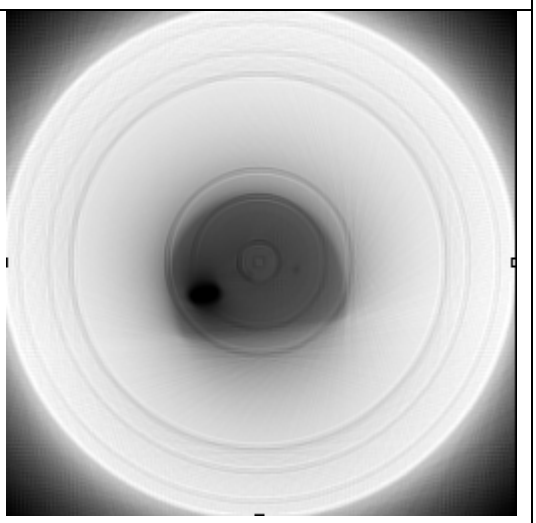
(b)	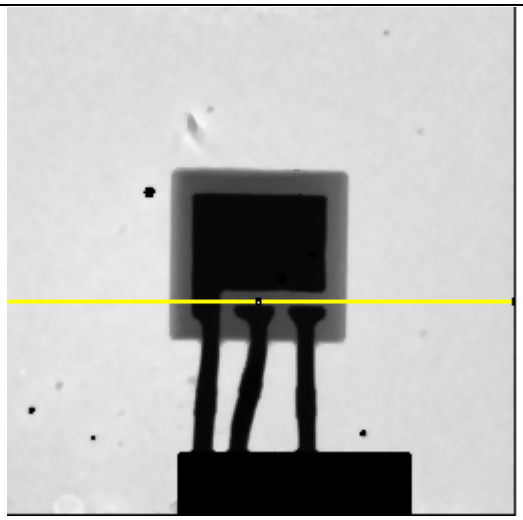	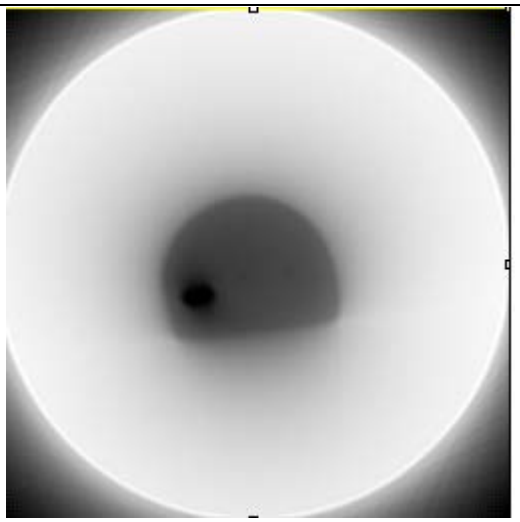

Table 5.3 shows the result for the generation of projection data for a voltage regulator. Image (a) is the raw image taken with the CdTe Timepix detector. The interval projection data is 1 degree. The tomogram image (a) was a slice image on the yellow line in line images. The minimum intensity algorithm is applied to produce tomogram in data projection. The tomogram shows the ring artifact. Meanwhile, Table 5.3 (b) shows the images after processing the with all of the software adjustments (flat field correction, noise filter and min intensity data projection). The result shows the tomogram with good quality images without the presence of the ring artifact. Table 5.4 shows the image of voltage regulator after an inversion process is conducted. The picture shows good quality of a

three- leg connector tomogram of voltage regulator inside the housing being visualized. The profile of the leg connector is shown in table 5.4 (d). This technique is beneficial for quality control in applications such as industrial production.

Table 5.4: *Invert of voltage regulator image.*

<table>
<tr><td> 
(a)</td><td> 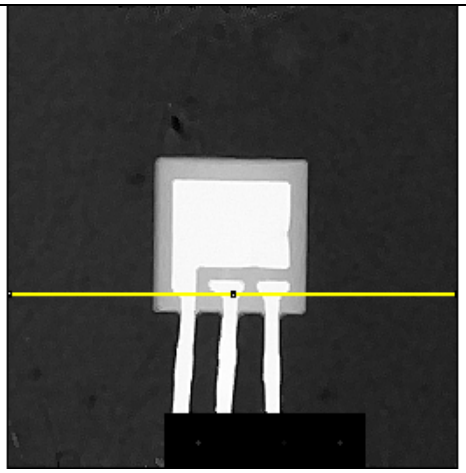
(b)</td></tr>
<tr><td> 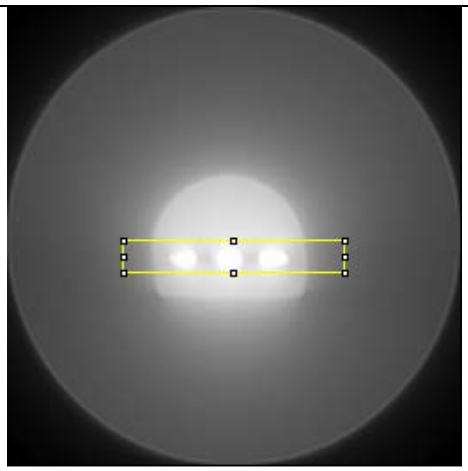
(c)</td><td> 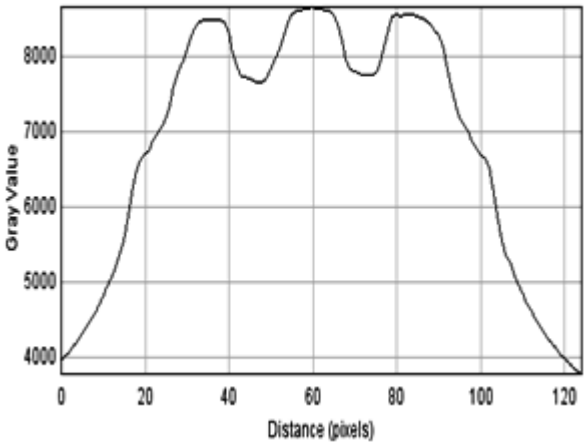

(d)</td></tr>
</table>

Table 5.5 shows the effect of different types of data projection in producing the tomogram for the voltage regulator. Table 5.5 (a) shows the tomogram after being processed using average intensity. The tomogram image shows the occurrence of the artifact (streaking patterns). After applying all software adjustments to the data as shown in Table 5.5 (b) the artifact was eliminated. The profile of the tomogram generated by the minimum intensity projection of the data shows low noise in between the 3 legs connector. The tomogram is produced from a slice along the cross section of the yellow line in the line image.

Table 5.5: *Different type of data projection*

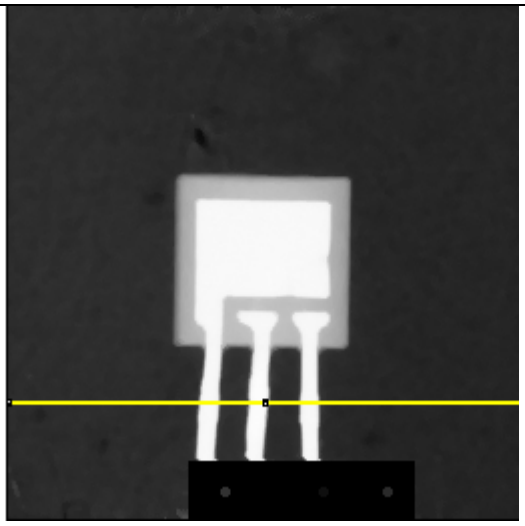

Line Image

Data projection	**Tomogram**	**Profile**
(a) Average Intensity	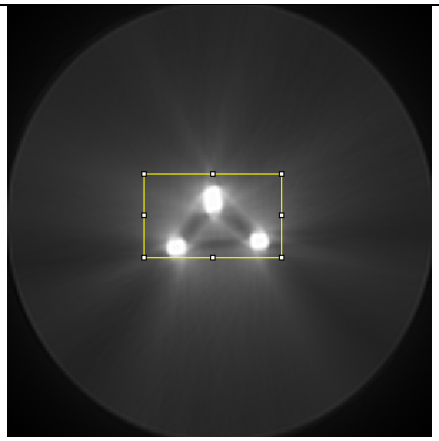	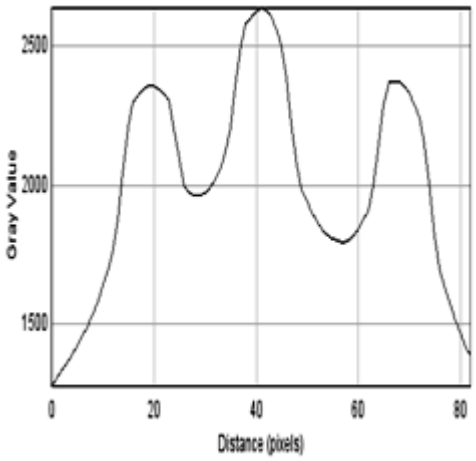
(b) Minimum Intensity	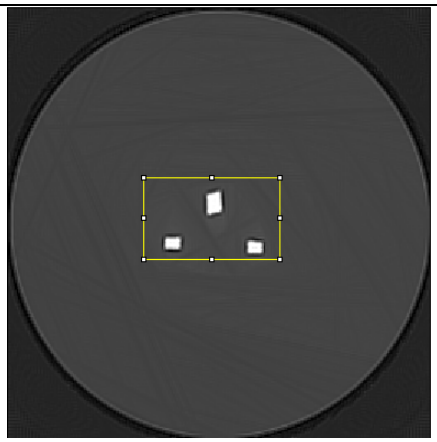	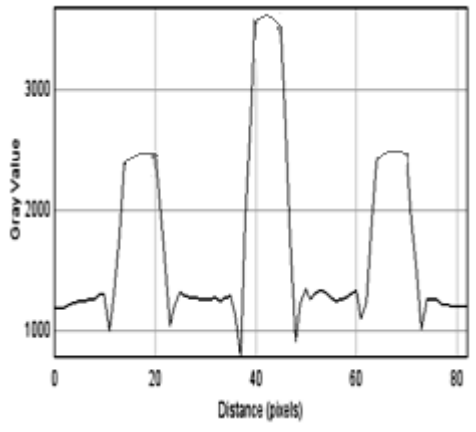

Table 5.6 shows the volume rendering of the voltage regulator. The volume rendering is produced by combining of all the tomograms in one plane. For the voltage regulator it contains two different density profiles, such as polypropylene and aluminium. The last image in Table 5.6 shows the aluminium profile inside the voltage regulator.

Table 5.6: *Volume rendering of voltage regulator*

(a) Photograph of an object

(b) 3D viewer of the object (combination all the stacks of slices)

(c) 3D image of the internal structure of the voltage regulator (aluminium)

5.5 Conclusion

In this study the pixellated CdTe Timepix detector has shown that it is capable of performing X-ray tomography producing images of high quality. It has also been shown that the optimisation of hardware arrangement and use of software correction can significantly improve the production of good quality images and 3D reconstruction. Through the hardware technique a clearer quality visual is obtained through the reduction and of beam hardening and scattering. For the data processing the first step is to apply a flat field correction. The results of a sample pencil show the flat field correction increases the SNR fortyfold compared to the image without the flat field correction. The second step is to apply a noise filter to reduce the noise from the detection processes; eliminate the dead pixels, glowing pixels, and other electronic noise in the detector and the data acquisition system. Following this the application of the minimum intensity method for data projection results in the generation of the best reconstruction. The tomogram results of the pencil and voltage regulator samples show that the techniques developed in this study can produce a good quality image and eliminate the artifacts.

Chapter 6

Conclusion

The study of *CdTe/CdZnTe* pixellated detectors is the topic of discussion of this thesis. The work covers the fabrication process used to make the detector, the characterisation of the *CdTe* Timepix detector in polychromatic and monochromatic X-ray beams and also the development of an imaging application for X-ray computed tomography.

In Chapter 3, the development of a dry fabrication process which optimises the surface treatment of the material and minimises the leakage current has been described. Through the SiN passivation and additional oxygen plasma oxidation technique used, it is shown that the bulk leakage current can be reduced by about an order of magnitude when compared to the samples used without the passivation process. It is also shown that the interpixel leakage current is considerably reduced. The effect of varying the thickness of the deposited layers using different thickness of SiN layers to observe the be behaviour of the reduction in leakage current. The results indicate that 200 nm, 400 nm and 500 nm SiN layer thickness provide a similar reduction in the interpixel leakage current measurement. The measured energy spectrum for Co-59 showed that passivation technique gives values 10.78 keV FWHM and an energy resolution of around 8.8 %.

In Chapter 4, the work on hybrid photon counting detector systems coupled to a *CdTe* Timepix detector assembly is presented. A characterisation of the *CdTe* Timepix detector system was carried out in order to gain a better understanding of charge sharing and the effects of fluorescence on detector performance. The studies measure and compare the performance of two *CdTe* Timepix detectors with pixel pitches of 55 μm and 110 μm and were conducted using ToT and DAC Scan mode to assess the performance differences between them.

In the study of the material properties of CdTe, the I-V measurement results showed that the I-V graph has a symmetrical ohmic behaviour. At 300 V the leakage current is around 8.28 x 10^{-6} A. The measurement of mobility lifetime of *CdTe* had been performed. The extracted mean $\mu\tau$ value from fitting the data are 1.35 ± 0.04 x 10^{-3} cm^2/V for electrons and 2.1 ± 0.34 x 10^{-4} cm^2/V for holes. This result is more than a factor of two better than previous published results on this type of material [67].

Although both detectors show a similarly acceptable spectroscopic performance for energies above ~1000 keV, the 110 um *CdTe* Timepix detector shows better energy spectrum performance compare to the 55 μm pitch in the energy range from 10 to 1000 keV. The systematic difference in energy resolution between two pixel pitches is associated with pixel-to-pixel non-uniform response not only in the ASIC but potentially related to the *CdTe* material itself. The results of these measurements also indicated that the DAC scan counting mode is better than that of ToT mode by factor of around 3-7. The monochromatic X-ray beam illumination at 79 keV shows that the 110 μm CdTe Timepix detector energy resolution in DAC scan counting mode is 1.5% either with or without clustering. For the ToT mode it is 4.3% with no clustering and 7.4% with clustered charge. The different of energy resolution suspected are due to the effects in electronic and clock noise, and also the setting of the detector.

As the small pixel size induces an important charge sharing effect which limits the spectroscopic capabilities of the sensor, post-treatment algorithms based on the summing

of signal from several adjacent pixels have been made to improve this condition. Decreasing the sensor thickness may also be an option to reduce charge sharing.

The CdTe detector with 55μm pitch demonstrated reasonable imaging performance. A 70% contrast at 4 *lp/mm* was achieved for the 55μm pixel pitch detector with a 60 kV X-ray tube and 5 kV noise level. No significant degradation in performance was observed for X-ray tube energies of 20–60 kV. The optimal bias voltage for imaging was found to be 400–500 V for 1 mm thick CdTe detector. As expected, around half the contrast transfer (30%) was recorded for the 110μm detector compared to that with 55μm pixels at 4 *lp/mm.*

There follows a study of defects in the material as these have a considerable influence on the detector performance and efficiency. Some defects, which show sufficient response and are stable over time, such as bright lines, can be corrected with flat field images, while the ring defects are more difficult or impossible to correct.

In Chapter 5, the imaging performance of the CdTe Timepix detectors of computed tomography had been assessed. Here, improved techniques were developed to provide good quality images by using the 55 μm CdTe Timepix detector. For the hardware setup, the alignment of components has been optimized between the X-ray tube, the sample and the CdTe Timepix detector. To minimise the effects of scattering, the beam was collimated at the X-ray tube window. Improvements to the imaging software included the addition of a flat field correction, noise filter and optimisation of the data projection algorithm. The flat field correction improved the SNR in the sample pencil to 187 when compared to the raw data which is around 5.26. The CdTe Timepix detector is capable of distinguishing the different density profile of the materials in the tomogram using volumetric rendering. In the Pencil sample used there were differences in the density profile of the paint coating, the wooden body and the carbon core. The technique which are capable of eliminating artifacts that occur in tomograph reconstruction have also been developed as part of this work. The beam hardening artifact, scattered artifact, ring artifact and shrink artifact which all degrade the quality of the reconstructed image have been suppressed using optimal filtering. To illustrate this the voltage regulator sample showed that the technique provides

good quality tomogram and eliminate the shrink effect associated with the dramatic density change caused by the metal in the sample.

Future research

There are a few suggestions that should be taken into consideration for further future studies regarding CdTe and CZT pixellated detector.

The currently available material is far from perfect and will need dedicated effort to improve the quality of the material if it is to be routinely used for radiation imaging. Furthermore, the need to for operation at high illumination intensities will require great improvements in the ability of the material to avoid the build up of a polarised field. This is a necessary quality if this material is to be used in CT applications for medical diagnostics. There is currently much interest in this and the application of energy resolving photon counting techniques in this area and so much effort is currently being devoted to improving the quality of the raw material.

When better material is available the fabrication process for CZT detector will need to be optimised and research should continue to study the effect of various techniques to improve interpixel properties in multi-element detectors in order to optimise bulk and interpixel performance, such as applied the negative resist (Su-8) in process photolithography.

The characteristics of the CdTe Timepix detector need to be prolonged to Time Over Arrival (ToA) mode performance, which later can be compared to the counting mode and ToT mode in polychromatic and monochromatic X-ray beam. The studies of polarization effects in monochromatic X-ray beam line should be continued also in order to understand the performance of CdTe material.

Finally, for computed tomography imaging using the CdTe Timepix detector, the performance can be considerably improved by introducing a weighted energy response of the detector to produce better quality images for the same dose. This is possible due to the energy sensitivity possible with thresholded photon counting techniques. The energy of the photons can be measured and a more accurate attenuation coefficient calculated for the range of energies that are emitted by the generator.

Based on this method the tomogram can be produce based on energy dependent image reconstruction techniques. This technique can be applied the energy dependent data set to reconstrust separate images of photoelectric abbsortion and Compton scatter interaction. These images will allow the end user to better discriminate the attenuation coefficient of the object in study for specific application, such as in medical application.

Bibliography

[1] W. R. Willig, 'Mercury iodide as a gamma spectrometer', Nucl. Instr. and Meth., vol. 96, pp. 615-616, doi: 10.1016/0029-554X(71)90182-0, **1971**

[2] D.S. McGregor, G.F. Knoll, Y.eisen, R.Brake, 'Development of bulk GaAs room temperature radiation detectors', IEEE Trans. Nucl. Sci., vol. 39, no. 5, pp. 1226-1236, **1992.**

[3] W. Akutagawa, K. Zanio, and J. W. Mayer, 'CdTe as a gamma detector', Nucl. Instr. and Meth, vol. 55, pp. 383-385, **1967.**

[4] J. F. Butler, C. L. Lingren, and F. P. Doty, 'CdZnTe gamma ray detectors', IEEE Trans. Nucl. Sci., vol. 39, no. 4, pp. 605-609**, 1992.**

[5] T. E. Schlesinger, J. E. Toney, H. Yoon, E. Y. Lee, B. A. Brunett, and L. Franks, 'Cadmium zinc telluride and its use as a nuclear radiation detector material', Materials Science and Engineering, vol. 32, pp. 103-189, **2001.**

[6] S. M. Sze, 'Semiconductor Devices Physics and Technology', John Wiley & Sons, 2nd Edition, **2002**

[7] Glenn F Knoll, 'Radiation Detection and measurement', John Wisley & Sons, Inc, 3rd Edition, **2000**

[8] Syed Ahmed, 'Physics and engineering of radiation detection', 1st edition, Academic Press, ISBN : 9780120455812. **2007**

[9] Streetman, B. G. & Banerjee, S. K. 'Solid State Electronic Devices', 6th ed. Pearson Education, Inc., New Jersey, USA. **2006**

[10] Halleday, D., Resnick, R. & Walker, J. 'Fundamentals of Physics', 7th ed. John Wiley & Sons, Inc., New Jersey, USA. **2005**

[11] Szeles, C., Eissler, E. E., Reese, D. J. & Cameron, S. E. 'Radiation Detector Performance of CdTe Single Crystals Grown by the Conventional Vertical Bridgman Technique'. eV Products, Pennsylvania, USA. **1999**

[12] J.F. Butler, B. Apotovsky, A. Niemela, H. Sipila, 'Sub-keV resolution with $Cd_{1-x}Zn_xTe$ detectors', Proceedings of the SPIE, Vol. 2009 X-ray Detector Physics and Application 11, SPIE, Bellingham, WA, pp. 121-127.**1993**

[13] W. Akutagawa, K. Zanio, J.W. Mayer, 'CdTe as gamma detector', Nuclear instrument & methods, Vol 55, pp. 398-385, doi: 10.1016/0029-554X (67)901474, **1967**

[14] Makram Hage-Ali, Paul Siffert, 'Growth methods of CdTe nuclear detector materials', Semiconductors for room temperature nuclear detector application, Vol 43 , pp. 291-334, ISSBN :978-0-12-752143-5, **1995**

[15] Stefano Del Sordo, Leonardo Abbene, Ezio Caroli, anna Maria Mancini, andrea Zappettini, Pietro Ubertini, ' Prohress in the development of CdTe and CdZnTe semiconductor radiation detectors for astrophysical and medical applications', Sensors 2009, ISSN 1424-8220, doi: 10.3390/s90503491, **2009**

[16] Alan Owens, A. Peacock, 'Compound semiconductor radiation detectors', Nuclear instruments and methods in physics research section A: accelerators, spectrometers, detectors and associated equipment, Vol 531, issues 1-2, pp 18-37, **2004**

[17] W. J. McNeil, D. S. McGregor, A. E. Bolotnikov, G. W. Wright, and R. B. James, 'Single-charge-carrier-type sensing with an insulated Frisch ring CdZnTe semiconductor radiation detector', Jounal of Applied Physics, AIP Publishing, 84, doi: 10.1063/1.1668332, 1988 (**2004**)

[18] N. Auricchio, E. Caroli, G. De Cesare, A. Donati, W. Dusi, M. Hage-Ali, G.Landini, E. Perillo, P. Siffert, 'Investigation of response behavior in CdTe detectors versus inter-electrode charge formation position'. IEEE Trans. Nucl. Sci., vol. 46, no. 4, pp. 853-857. **1999**

[19] V.T. Jordanov, J.A. Pantazis, A. Huber, 'Compact circuit for pulse rise-time discrimination'. Nucl. Instrum. Meth. Phys. Res., vol. 380, pp. 353-357. **1996**

[20] M. Richter, P. Siffert 'High resolution gamma ray spectroscopy with CdTe detector systems'. Nucl. Instrum. Methods Phys. Res., vol. 322, pp. 529-537. **1992**

[21] N. Auricchio, L. Amati, A. Basili, E. Caroli, A. Donati, T. Franceschini, F.Frontera, G. Landini, A. Roggio, F. Schiavone, J.B. Stephen, G. Ventura, 'Twin shaping filter techniques to compensate the signals from CZT/CdTe detectors'. *IEEE Trans.* Nucl. Sci., vol. 52, no.5, pp. 1982-1988, **2005**

[22] D.S. McGregor, Z He, H.A Seifert, D.K Wehe, R.A Rojeski, 'Single charge carrier type sensing with a parallel strip pseudo-frisch-grid CdZnTe semiconductor radiation detector'. Applied Phyics Leter, vol. 72, no. 7, pp. 792-794, **1998**

[23] A.E Bolotnikov, G.C Camarda, G.A Carini, M. Fiederle, L Li, D.S McGregor, W McNeil, G.W Wright, R.B James, 'Performance characteristics of frisch-ring CdZnTe detectors'. IEEE Trans. Nucl. Sci., vol.53, no.2, pp. 607-614. **2006**

[24] H.H. Barrett, J.D. Eskin, H.B. Barber, 'Charge transport in arrays of semiconductor gamma-rays detectors'. Phys. Rev. Lett. 1995, vol.75, pp.156-159. **1995**

[25] I. Kuvvetli, C. Budtz-Jørgensen, 'Pixelated CdZnTe drift detectors'. IEEE Trans. Nucl. Sci. 2005, vol. 52, pp. 1975-1981, **2005**

[26] L. Abbene, S. Del Sordo, G. Agnetta, B. Biondo, E. Caroli, A. Mangano, F.Russo, J.B. Stephen, G. Ventura, A. Carlino, G. Gerardi, G. Bertuccio, 'Investigation

on pixellated CZT detectors coupled with a low power readout ASIC'. IEEE Nucl. Sci. Symp. Conf. Rec. 2008, pp. 478-483, **2008**

[27] Luke, P.N. 'Unipolar charge sensing with coplanar electrodes - application to semiconductor detectors'. IEEE Trans. Nucl. Sci. 1995, vol. *42*, pp. 207-213,**1995**

[28] A. Shor, Y. Eisen, I. Mardor, 'Optimum spectroscopic performance from CZT γ- and X-ray detectors with pad and strip segmentation'. Nucl. Instrum. Meth. Phys. Res. A 1999, vol. *428*, pp.182-182, **1999**

[29] E. Perillo, A. Cola, A. Donati, W. Dusi, G. Landini, A. Raulo, G. Ventura, S.Vitulli, 'Spectroscopic response of a CdTe microstrip detector when irradiated atvarious impinging angles', Nucl. Instrum. Meth. Phys. Res. A 2004, vol. *531*, pp. 125-133, **2004**

[30] C.L. Lingren, B. Apotovsky, J.F. Butler, R.L. Conwell, F.P. Doty, S.J. Friesenhahn, A. Oganesyan, B. Pi, S. Zhao, 'Cadmium-zinc telluride, multiple-electrode detectors achieve good energy resolution with high sensitivity at room-temperature'. IEEE Trans. Nucl. Sci. 1998, vol. *45*, pp. 433-437, **1998**

[31] H. Kim, L. Cirignano, K. Shah, M. Squillante, P. Wong, 'Investigation of the energy resolution and charge collection efficiency of Cd(Zn)Te detectors with three electrodes'. IEEE Trans. Nucl. Sci. 2004, vol.*51*, pp.1229-1234, **2004**

[32] L. Abbene, S. Del Sordo, F. Fauci, G. Gerardi, A. La Manna, G. Raso, A. Cola, E. Perillo, A. Raulo, V. Gostilo, S. Stumbo, 'Spectroscopic response of a CdZnTe multiple electrode detector', Nucl. Instrum. Meth. Phys. Res. *A* 2007, vol. *583*, pp. 324-331, **2007**

[33] Van Pamelen, M.A.J.; Budtz-Jørgensen, C. 'CdZnTe drift detector with correction for hole trapping'. Nucl. Instrum. Meth. Phys. Res. A 1998, vol. *411*, pp. 197-200, **1998**

[34] D Maneuski, V Astromskas, E Fröjdh, C Fröjdh, E N Gimenez, J Marchal, V O'Shea, G Stewart, N Tartoni, H Wilhelm, K Wraight, R M Zain. 'Imaging and spectroscopic performance studies of pixellated CdTe Timepix detector', *Journal of Instrumentation* 7 C01038, IOP science, doi: 10.1088/1748-0221/7/01/C01038, **2012**

[35] E. Wilson. 'An introduction to particle accelerators'. Oxford University Press, Oxford, **2001.**

[36] Diamond Light Source. Diamond website. Available: http://www.diamond.ac.uk, **2014.**

[37] K. Wille. 'Synchrotron radiation sources'. Reports on Progress in Physics, vol.54 (8), pp. 1005-1068, **1991**

[38] M. J. Mescher et al., 'Development of Dry Processing Techniques for CdZnTe Surface Passivation', Journal of Electronic Material, vol. 28, no. 6, **1999**

[39] J.T. Mullins, B.J. Cantwell, A. Basu, Q. Jiang, A. Choubey, A.W. Brinkman, and B.K. Tanner, 'Vapor-Phase Growth of Bulk Crystals of Cadmium Telluride and Cadmium Zinc Telluride on Gallium Arsenide Seed', Journal of electronic Materials, vol. 37, Issue 9, pp1460-1464, **2008**

[40] http://en.wikipedia.org/wiki/Lithography, **2014**

[41] Andrew James Blue, 'New Materials & Processes for Radiation Detection', Ph.D. dissertation, University of Glasgow, **2005**

[42] http://microchem.com/PDFs_Dow/S1800.pdf, **2014**

[43] Chen, H et. al., 'Photoluminescence investigation of surface oxidation of $Cd_{0.9}Zn_{0.1}Te$ detector', Mat. Res. Soci. Symp. Proc., vol. 487, pp. 65-70, **1998**

[44] Wright et. al., 'Effect of surface roughness on large –volume CdZnTe Nuclear Radiation detection and removal of surface damage by chemical etching', Proc. SPIE, vol. 5198, pp. 306-313, **2004**

[45] M. J. Mescher et. al., 'Development of dry processing technique of CdZnTe Surface passivation', Journal of electronic material, vol.28, no.6, **1999**

[46] Alireza Kargar, Adam C. Brooks, Kyle T. Kohman, Rans B. Lowell, Roger C. Keyes, Henry Chen, Salah Awadalla, Glenn Bindley and Douglas S. McGregor, 'Final surface effect on performance of CdZnTe Frisch collar gamma ray detectors', proceeding of SPIE, Vol 7079, doi: 10.1117/12.795366, **2008**

[47] Y. Eisen, A. Shor, 'CdTe and CdZnTe materials for room temperature X-ray and gamma ray detectors, Jounal of crystal growth vol. 184/185, pp.1302-1312, **1998**

[48] Sang Wenbin, Wang Kunshu, Min Jiahua, Teng Jianyong, Zhang Qi and Qian Yongbiao, 'A novel two-step chemical passivation process for CdZnte detectors', IOP Publishing Semicond. Sci. Technol., vol. 20, pp. 343-346. doi: 10.1088/0268-1242/20/5/003, **2005**

[49] Y. Cui, M. Groza, A. Burger, and R. B. James, 'Effects of surface processing on the performance of $Cd_{1-x}Zn_xTe$ radiation detectors', IEEE trans. on nuclear science, vol. 51, no 3, pp.1172-1175. **2004**

[50] Wright G W and James R B, 'Evaluation of NH_4F/H_2O_2 effectiveness as a surface passivation for $Cd_{1-x}Zn_xTe$ crystal', SPIE proceeding vol. 4141, pp. 324-335, **2000**

[51] Kaushik Chattopadhyay, et. all., 'Surface passivation of cadmium Zinc Telluride radiation detectors by potassium hydroxide solution', Jounal of electronic materials, vol. 29, no. 6,pp. 708-71, **2000**

[52] R M Zain, D Maneuski, V O'Shea, R Bates, A Blue, L Cunnigham, C Stehl, E Berderman and R A Rahim, "Leakage current measurements of a pixelated polycrystalline CVD diamond detector" Journal of Instrumentation *JINST* **8** C01056 doi:10.1088/1748-0221/8/01/C01056, **2012**

[53] A. Balducci et al., Synthesis and characterization of a single-crystal chemical-vapor-deposition diamond particle detector, Appl. Phys. Lett. vol. 86, issue 21, 213507, **2005**

[54] Goro Sato, Tadayuki Takahashi, Masahiko Sugiho, Manabu Kouda, Takefumi Mitani, 'Characterization of CdTe/CdZnTe Detectors', IEEE Transactions on Nuclear Science, vol.49, no.3, pp. 1258-1263. **2002**

[55] Xavier llopart, Timepix manual V1.0, file :Timepix manualV1.0.pdf

[56] X. Llopart, M. Campbell, R. Dinapoli, D. San Segundo, and E. Pemigotti. 'Medipix2: a 64-k pixel readout chip with 55 μm square elements working in single photon counting mode'. IEEE Transactions on Nuclear Science, vol.49, no. 5, pp.2278-2283, **2002**

[57] X. Llopart, R. Ballabriga, M. Campbell, L. Tlustot, and W. Wong, 'Timepix, a 65k programmable pixel readout chip for arrival time, energy and/or photon counting measurements', Nuclear Instruments and Methods in Physics Research A, vol. 581, pp.485-494, **2007**

[58] Z. Vykydal, J. Jak_ubek, and S. Pospsil, 'USB Interface for Medipix2 Pixel Device Enabling Energy and Position Detection of Heavy Charged Particles', Nuclear Instruments and Methods A, vol. 536. pp. 112-115, **2006**

[59] M. Platkevic, V. Bocarov, J. Jakubek, S. Pospsil, V. Tichy, and Z. Vykydal, 'Signal processor controlled USB2.0 interface for Medipix2 detector', Nuclear Instruments and Methods A, vol. 591, pp. 245-247, doi: 10.1016/j.nima.2008.03.065, **2008**

[60] V Kraus, M Holik, J Jakubek and V Georgiev, 'FITPix data preprocessing pipeline for the Timepix single particle pixel detector', IOP Science Journal of Instrumentation, vol. 7, doi:10.1088/1748-0221/7/04/C04011, **2008**

[61] T. Holy et al. 'Data acquisition and processing software package for Medipix-2 device',Nuclear Instruments and Methods A, vol.563, pp. 254- 258, **2006**

[62] X. Llopart, R. Ballabriga, M. Campbell, L. Tlustos, W. Wong, 'Timepix, a 65k programmable pixel readout chip for arrival time, energy and/or photon counting measurements', In: Nuclear Instruments and Methods A, vol. 581, pp. 485–494, **2007**

[63] M Niraula, A Nakamura, T Aoki, Y Tomita, Y Hatanaka, 'Stability issues of high-energy resolution diode type CdTe nuclear radiation detectors in a long-term operation', Nuclear Instruments & Methods Physics Research Section A, vol. 491, pp.168-175, doi: 10.1016/S0168-9002(02)01175-0, **2002**

[64] Acrorad, http://www.acrorad.co.jp/us/index.html.

[65] Marie Ruat and Cyril Ponchut, 'Characterization of a pixelated CdTe x-ray detector using the timepix photon-counting readout chip', IEEE Transactions on Nuclear Science, vol. 59, no. 5, **2012**

[66] Yanfeng Du, James LeBlanc, George E, Possin, Brian D, Yanoff and Snezana Bogdanovich, 'Temporal response of CZT detectors under intense irradiation', IEEE Transactions on Nuclear Science, vol. 50, no. 4, pp. 1031-1035, **2003**

[67] D. Greiffenberg, A. Fauler, A. Zwerger and M. Fiederle, 'Energy resolution and transport properties of CdTe-Timepix –Assemblies', IOP science, JINST 6 C01058, doi : 10.1088/1748-0221/6/01/C01058, **2011**

[68] O. Limousin, 'New trends in CdTe and CdZnTe detectors for X- and gamma-ray applications', Nuclear Instruments and Methods in Physics Research.Vol.504, pp. 24-37, doi: 10.1016/S0168- 9002(03)00745-9, **2003**

[69] A. Ruzin, J.Gorelik and Y. Nemirovsky, 'Mobility-lifetime product of CdTe/CdZnTe crystals from charge collection efficiency of x-ray detectors', Eighteenth Convention of Electrical and Electronics Engineers in Israel 1995, IEEE 10.1109/EEIS.1995.513837, **1995**

[70] J. Jakubek, Andrea Cenjnarova, Tomas Holy, Stanislav pospisill, Josef Uher, Zdenek Vykydal, 'Pixel detectors for imaging with heavy charged particles', Nuclear Instruments & Methods A, vol. 591, pp. 155-158, doi: 10.1016/j.nima.2008.03.091, **2008**

[71] Diamond Light Source Ltd., Extreme Conditions Beamline I15, http://www.diamond.ac.uk/Home/Beamlines/I15.html.

[72] J. Jakůbek, 'Energy sensitive X-ray radiography and charge sharing effect in pixelated detector', Nuclear Instruments & Methods A, vol. 607, issue 1, pp. 192-195, **2009**

[73] J. Bouchami, A. Gutierrez, A. Houdayer, J. Idarraga, J. Jakůbek, C. Lebel, C. Leroy, J. Martin, M. Platkevič, S. Pospíšil, 'Study of the charge sharing in silicon pixel detector with heavy ionizing particles interacting with a Medipix2 device', Nuclear Instruments & Methods A, vol. 607, issue 1, pp. 196-198, **2009**

[74] J. Marchal, 'Theoretical analysis of the effect of charge-sharing on the Detective Quantum Efficiency of single-photon counting segmented silicon detectors', IOP science, Journal of Instrumentation, 5, P01004, **2010**

[75] E. Hamann *et al.*, 'Applications of Medipix2 single photon detectors at the ANKA synchrotron facility', in Proc. IEEE NSS/MIC, pp. 3860–3863, IEEE, **2010**

[76] P. N. Luke and E. E. Eissler, 'Performance of CdZnTe coplanar-grid gamma-ray detectors', IEEE Trans. Nucl. Sci., vol. 43, no. 3, pp. 1481–1486, Jun. **1996**

[77] Marie Ruat and Cyril Ponchut, 'Characterization of a Pixelated CdTe X-Ray Detector Using the Timepix Photon-Counting Readout Chip', IEEE Transactions on Nuclear Science, vol. 59, no. 5, October **2012**

[78] Webb, S. From the watching of the shadows. The origins of radiological tomography, IOP Publishing Ltd 1990, ISBN 0-58274-305-X, **1990**

[79] S J Doran and N Krstajić. The history and principles of optical computed tomography for scanning 3-D radiation dosimeters, Journal of Physics: Conference Series 56 45–57, doi:10.1088/1742-6596/56/1/005, **2006**

[80] Gabor T.Herman . Fundamental of computerized tomography, second edition, Springer –Verlag London Limited 2009, ISBN 978-1-85233-617-2, **2009**

[81] Julia F.Barrett, Nicholas Keat, 'Artifacts in CT: recognition and avoidance', RSNA journal, vol. 24, issue 6, pp. 1679-1691, doi: 10.1148/rg246045065, **2004**

[82] B. De man, J.Nuyts, P.Dupont, G. Marchal and P. Suetens, 'Metal streak artifacts in X-ray computed tomography: A simulation study', IEEE Transactions on Nuclear Science, vol. 46, no. 3, pp. 691-696, **1999**

[83] Xiameng Zhang, 'Metal artifact reduction in x-ray computed tomography (CT) by constrained optimization', Journal of medical physics, vol.38, no.2, pp. 701-711, doi : 10.1118/1.3533711, **2011**

[84] F Edward Boas, Dominik Fleischmann, 'CT artifacts: causes and reduction techniques', Imaging in medicibe, vol. 4, no.2, pp. 229-240, doi: 10.2217/iim.12.13, **2012**

[85] Jan Sijbers, Andrei Postnov, 'Reduction of ring artifacts in high resolution micro-CT reconstructions', physics in medicine and biology, vol. 49, no.14, **2004**

[86] Yiannis Kyriakou, Daniel Prell and Willi A Kalender, 'Ring artifact correction for high-resolution micro CT', IOP Publishing Physics In Medicine And Biology, Phys. Med. Biol. vol. 54, pp. 385–391, **2009**

[87] Riess T, Fuchs T and Kalender W A, 'A new method to identify and to correct circular artifacts in x-ray CT images', Phys. Medica, vol. 2, pp. 43–55, **2004**

[88] Whiting, B. R, 'Signal statistics of X-ray computed tomography', Proceedings SPIE:Med. Im. *2002* pp. 53–60, **2002**

[89] Elbakri, I. A. & Fessler, J. A, 'Segmentation-free statistical image reconstruction for polyenergetic X–ray computed tomography with experimental validation', Phys. Med. Biol. vol. 48, pp.2453–2477, **2003**

[90] Mini-X X-ray Tube 50kV USB controlled user's manual.pdf

[91] OWIS PS 10 Position control user manual. pdf

[92] Dzmitry maneuski, 'Pixellated radiation detector for scientific application', Ph.D. dissertation, University of Glasgow, **2009**

[93] Daniel Vavrik, Tomas Holy, Jan Jakubek, Stanislav Popisil, Zdenek Vykydal, Jiri Dammer, X-ray Micro radiography using beam hardening correction', IEEE Nuclear Science Symposium Conference record, **2005**

[94] Börje Norlin, 'Characterisation and application of photon counting X-ray detector systems', Ph.D. dissertation, Mid Sweden University, **2007**

[95] http://www.slicer.org/archives/users/index.html#1

[96] F. Mess, R. Swennen, M. Van geet, P. Jacobs, 'Application of x-ray computed tomography in the geosciences' Geological Society, London, Special Publications, vol. 215, pp. 1-6, doi: 10.1144/GSL.SP.2003.215.01.01, **2003**

Appendices

Appendix A

List of abbreviations

Abbreviation	Description	Definition
CdTe	Cadmium Telluride	i
CdZnTe	Cadmium Zinc Telluride	i
SiN	Silicon Nitride	i
FWHM	Full width half maximun	i
HgI_2	Mercury (II) Iodide	2
GaAs	Gallium arsenide	2
RIE	Reactive ion electron	3
MTF	Module transfer function	3
I-V	Current -Voltage	4
ToT	Time over threshold	4
CCE	Charge collection efficiency	14
MCA	Multi-channel analyser	16
THM	Travelling heater method	17

PTF	Planar transverse field	19
PPF	Planar parallel field	19
RF	Radio-frequency	20
JWNC	James Watt Nano Fabrication Centre	22
CATS	Computer Aided Transcription System	28
GDSII	Graphic Data System II	28
BELLE	Beam-writer exposure layout for lithography engineers	28
HDMS	Hexamethyldisilazane	32
LAF	Laminar air flow	32
rpm	Revolution per minute	32
RO	Reverse osmosis	32
ICP	Inductively coupled plasma	35
SEM	Scanning electron microscope	37
DAC	Digital analog converters	57
ReLaXd	High resolution large area X-ray detector	59
THL	Threshold level	61
ToA	Time of arrival	62

Appendix B

List of publications

Below is the list of publication arised during the time of work on this thesis.

1. **R M Zain**, D Maneuski, V O'Shea, R Bates, A Blue, L Cunnigham, C Stehl, E Berderman and R A Rahim, "Leakage current measurements of a pixelated polycrystalline CVD diamond detector" Journal of Instrumentation *JINST* **8** C01056 doi:10.1088/1748-0221/8/01/C01056

2. E. Frojdh, C. Frojdh, Gimenez ,D. Maneuski, J. Marchal, B. Norlin, V. O'Shea,G. Stewart, **R. Mohd Zain**, G. Thungstrom, Heribert Wilhelm, "Depth of interaction and bias voltage depenence of the spectral response in a pixellated CdTe detector operating in time-over-threshold mode subjected to monochromatic X-rays ", JOURNAL OF INSTRUMENTATION 7 DOI: 10.1088/1748-0221/7/03/C03002

3. Dzmitry Maneuski, V Astromskas, E Fröjdh, C Fröjdh, Eva Gimenez-Navarro, Julien Marchal, V O'Shea, G Stewart, Nicola Tartoni, Heribert Wilhelm, K Wraight, **R M Zain,** "Imaging and spectroscopic performance studies of pixellated CdTe Timepix detector", Journal of Instrumentation 7 DOI: 10.1088/1748-0221/7/01/C01038

4. R. Bates, A. Blue, M. Christophersen, L. Eklund, S. Ely, V. Fadeyev, E. Gimenez, V. Kachkanov, J. Kalliopuska, A. Macchiolo, D. Maneuski, B. F. Phlips, H. Sadrozinski, G. Stewart, N. Tartoni, **R. M. Zain,** "Characterisation of edgeless technologies for pixellated and strip silicon detectors with a micro-focused X-ray beam", Journal of Instrumentation, 2013, Vol. 8, Issue 01, Article P01018 doi:10.1088/1748-0221/8/01/P01018

5. E. Frojdh, C. Frojdh, E.N. Gimenez, D. Krapohl, D. Maneuski, B. Norlin, V. O'Shea, H. Wilhelm, N. Tartoni, G. Thungstrom, **R.M. Zain,** " Probing Defects in a Small Pixellated CdTe Sensor Using an Inclined Mono Energetic X-Ray Micro Beam" IEEE Transactions on Nuclear Science 01/2013; 60(4):2864-2869.

Appendix C

Image reconstruction software

```
macro "openBatchTextImagesToStack" {
	//dir = getDirectory("Choose a Directory ");
	//dir = "G:\\140318_CT\\50kV\\"
	dir = "C:\\Users\\Rasif\\Desktop\\190314_CT\\latest\\50kVlatest\\"
	//dir = "/data\\detdev03\\medipix\\10032900AmTOTSi50V/"
	a1 = getFileList(dir);
	Array.sort(a1);
	if (getVersion>="1.40e")
	setOption("display labels", true);
	setBatchMode(true);
	for (i=0000; i < a1.length; i++) {
		path = dir+a1 [i];
		showProgress(i, a1.length);
		if (!endsWith(path,"/")) {
			if (!endsWith(path,".dsc")) {
				if (!endsWith(path,".idx")) {
					print(path);
					run("Raw...", "open="+ path + " image=[32-bit Unsigned] width=256 height=256 offset=0 number=1000 gap=0 little-endian");
					//run("Measure");
				}
			}
		}
	}
	run("Images to Stack", "title=[]");
	setBatchMode(false);
}
setBatchMode(true);
var img=getTitle();
var startSlice = 0;
for (slice=48; slice <49; slice++) { //getHeight()
   var out="rec2D_BP_"+img;
   selectWindow(img);
   w=getWidth();
   newImage(out, "32-bit Black", w, w, 1);
   //newImage(out, "16-bit Black", w, w, 1);
   newImage("backproj", "32-bit Black", w, w, 360);
   //newImage("backproj", "16-bit Black", w, w, 360);

   for (j=0; j<360; j++) {  // number of angles
     selectWindow(img); setSlice(j+1);
     makeRectangle(0, slice+startSlice, w, 1);
     run("Duplicate...", "title=line");
```

```
      run("Scale...", "x=- y=- width=" + w + " height=" + w + " interpolation=Bicubic create
title=proj");
      run("Rotate... ", "angle="+1*(-j)+" grid=100 interpolation=Bicubic enlarge");
      imageCalculator("Add", out,"proj");
      selectWindow("line"); close();
      selectWindow("proj");
      run("Select All");
      run("Copy");
      close();
      selectWindow("backproj");
      setSlice(j+1);
      run("Paste");
  }
          var img1=getTitle()+slice+startSlice;
          print(img1);
          //run("Z Project...", "start=1 stop=360 projection=[Average Intensity]");
          //run("Z Project...", "start=1 stop=360 projection=[Standard Deviation]");
          //run("Z Project...", "start=1 stop=360 projection=[Sum Slices]");
          //run("Z Project...", "start=1 stop=360 projection=[Median]");
          run("Z Project...", "start=1 stop=360 projection=[Max Intensity]");
          //run("Z Project...", "start=1 stop=360 projection=[Min Intensity]");
          run("Smooth", "stack");
          run("Sharpen", "stack"); run("Sharpen", "stack");
          run("Copy");
          //run("Sharpen", "stack");
          newImage(getTitle()+slice+startSlice, "32-bit Black", w, w, 1);
          //newImage(getTitle()+slice+startSlice, "16-bit Black", w, w, 1);
          run("Paste");run("Enhance Contrast", "saturated=0.4");
          //run("Enhance Contrast...", "saturated=0.4 normalize process_all")
          run("Save", "save=D:\\1CT\\VR_THL\\test1\\"+img1+".tif");
          //run("Save", "save=C:\\Users\\Rasif\\Desktop\\Result131113CTVolReg\\"+img1+".tif");
          //selectWindow("backproj");  close();
}
setBatchMode(false);
```